



## Durham E-Theses

---

### *Computational Studies of Light-Matter Interactions in Two- and Three-Dimensional Systems*

LITTLE, CLAIRE,ELSPETH

#### How to cite:

---

LITTLE, CLAIRE,ELSPETH (2011) *Computational Studies of Light-Matter Interactions in Two- and Three-Dimensional Systems*, Durham theses, Durham University. Available at Durham E-Theses  
Online: <http://etheses.dur.ac.uk/3372/>

#### Use policy

---

The full-text may be used and/or reproduced, and given to third parties in any format or medium, without prior permission or charge, for personal research or study, educational, or not-for-profit purposes provided that:

- a full bibliographic reference is made to the original source
- a [link](#) is made to the metadata record in Durham E-Theses
- the full-text is not changed in any way

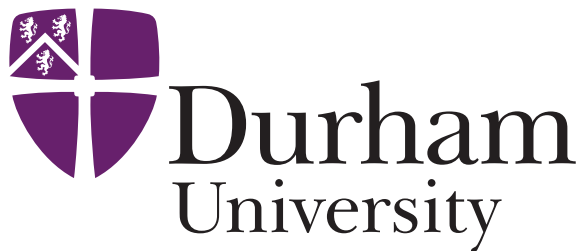
The full-text must not be sold in any format or medium without the formal permission of the copyright holders.

Please consult the [full Durham E-Theses policy](#) for further details.

# COMPUTATIONAL STUDIES OF LIGHT-MATTER INTERACTIONS IN TWO- AND THREE-DIMENSIONAL SYSTEMS

Claire Elspeth Little

A thesis presented for the degree of  
Doctor of Philosophy



Supervised by Professor R.A. Abram  
Department of Physics  
Durham University

2011

# Computational Studies of Light-Matter Interactions in Two and Three Dimensional Systems

Claire Elspeth Little

Submitted for the degree of Doctor of Philosophy

2011

## Abstract

A computational approach is taken to studying a range of light-matter interactions which are interesting in terms of their potential applications as well as from a fundamental point of view.

Two different types of polariton, part-light, part-matter quasiparticles, namely exciton-polaritons and Tamm plasmon-polaritons (a type of surface plasmon-polariton) are considered. The conditions required for the strong coupling of optical whispering-gallery modes and bulk excitons in submicron spheres are ascertained for the materials gallium arsenide, gallium nitride and zinc oxide. It is shown that the strong coupling regime may be accessed by optical modes with a low decay constant, typically exhibited by those modes with higher angular momentum quantum numbers.

Tamm plasmon-polaritons have previously been shown to exist at the boundary between a metal and a planar Bragg reflector structure. The conditions required for the formation of Tamm plasmon-polaritons in cylindrical multilayer structures with a metal core, cladding or metal in both of these locations are determined. The cylindrical Tamm plasmon-polaritons are shown to have low effective masses and low group velocities. It is also shown that it is possible to obtain split polariton modes in structures containing metal in both the core and the cladding.

The effect of disorder on a two-dimensional photonic crystal structure consisting of air holes in a slab of dielectric material is studied. It is shown that the defined threshold disorder is not significantly affected by the different relative band widths of the ideal crystal structures considered.

# Declaration

The work in this thesis is based on research carried out under the supervision of Professor Abram, in the Department of Physics, University of Durham, England. No part of this thesis has been submitted elsewhere for any other degree or qualification and it is all my own work unless referenced to the contrary in the text.

**Copyright** ©2011 by C Little.

“The copyright of this thesis rests with the author. No quotations from it should be published without the author’s prior written consent and information derived from it should be acknowledged”.

# Acknowledgements

This thesis would not have been possible without the continual support of my husband John, my family and friends. Special thanks must go to my officemates Dawn Geatches, Robyn Cooke and Lara Small for their daily encouragement.

I gratefully acknowledge the help of colleagues in the Durham Condensed Matter Theory Group, in particular my supervisor Richard Abram for providing direction and guidance throughout. Also, Stuart Brand, Mikhail Kaliteevski and Ivan Iorsh for helpful discussions and providing some of the Fortran code that has been used in the calculations presented here.

I would like to thank the EPSRC for funding the research and making the whole project possible.

# Contents

<b>Declaration</b>	<b>ii</b>
<b>1 Introduction</b>	<b>1</b>
1.1 Light-matter interactions . . . . .	1
1.2 Photonic crystals and the Bragg reflector . . . . .	3
1.2.1 The Bragg reflector . . . . .	3
1.2.2 Photonic crystals . . . . .	4
1.3 Polaritons . . . . .	7
1.3.1 Exciton-polaritons . . . . .	7
1.3.2 Surface plasmon-polaritons and Tamm plasmon-polaritons . . . . .	7
1.4 Theoretical framework . . . . .	9
1.5 Outline of the thesis . . . . .	10
<b>2 Exciton-polaritons in sub-micron spheres</b>	<b>11</b>
2.1 Excitons . . . . .	11
2.2 Exciton-polaritons . . . . .	12
2.2.1 Rabi splitting . . . . .	16
2.2.2 Exciton-polariton phenomena . . . . .	17
2.3 Cylindrical and spherical microcavities . . . . .	19
2.3.1 Whispering-gallery modes . . . . .	19
2.3.2 Exciton-polaritons in cylindrical and spherical cavities . . . . .	20
2.4 Electromagnetic waves in spherical cavities . . . . .	21
2.4.1 Eigenfrequencies of the spherical cavity . . . . .	24

2.4.2	Reflection from the spherical boundary . . . . .	26
2.5	Mode decay in spherical cavities . . . . .	29
2.5.1	Estimate of the polariton splitting . . . . .	33
2.5.2	Optical mode analysis . . . . .	34
2.6	Exciton-polariton calculations . . . . .	38
2.6.1	Results . . . . .	38
2.7	Discussion . . . . .	42
<b>3</b>	<b>Tamm plasmon-polaritons in cylindrical fibres</b>	<b>45</b>
3.1	Surface plasmon-polaritons . . . . .	45
3.1.1	Uses of surface plasmon-polaritons . . . . .	51
3.2	Tamm plasmon-polaritons . . . . .	51
3.2.1	Reflection from the metal . . . . .	55
3.2.2	Reflection from the Bragg reflector . . . . .	56
3.2.3	Other work on TPPs . . . . .	57
3.3	Cylindrical structures . . . . .	58
3.3.1	Transfer matrix method . . . . .	58
3.4	Cylindrical structures with metallic features . . . . .	66
3.4.1	Cylindrical surface plasmon-polaritons . . . . .	66
3.4.2	Surface plasmon-polaritons in optical fibres . . . . .	68
3.5	Multilayer cylindrical structures with metallic features . . . . .	73
3.5.1	Cylindrical Bragg reflector structures . . . . .	74
3.5.2	Cylindrical structures for Tamm plasmon-polaritons . . . . .	74
3.5.3	A simplification of the transfer matrix problem . . . . .	81
3.6	Results . . . . .	84
3.6.1	Bragg reflector . . . . .	84
3.6.2	Indication of modes in a Bragg reflector structure . . . . .	90
3.6.3	Metal core . . . . .	91
3.6.4	Metal cladding . . . . .	99
3.6.5	Metal core and metal cladding . . . . .	101
3.7	Discussion . . . . .	102

<b>4</b>	<b>Disorder in Two-Dimensional Photonic Crystals</b>	<b>106</b>
4.1	Introduction . . . . .	106
4.1.1	Electromagnetic waves in photonic crystals . . . . .	108
4.2	Disorder in photonic crystals . . . . .	109
4.2.1	Disorder in two-dimensional photonic crystals . . . . .	110
4.3	Introduction to <i>OmniSim</i> . . . . .	114
4.4	The photonic crystal structure . . . . .	118
4.4.1	The ideal structure . . . . .	118
4.4.2	The disordered structure . . . . .	121
4.5	Analysis . . . . .	123
4.5.1	Flux analysis . . . . .	124
4.5.2	Directional energy analysis . . . . .	129
4.5.3	Mean refractive index . . . . .	137
4.5.4	Frequency limits . . . . .	138
4.6	Discussion . . . . .	141
<b>5</b>	<b>Summary and future work</b>	<b>145</b>
	<b>Bibliography</b>	<b>148</b>
	<b>Appendices</b>	<b>161</b>

# List of Figures

1.1	A structure consisting of alternating layers of different refractive index acts as a near-perfect mirror for light of certain wavelength. The greater the number of layers the more effective the mirror. . . . .	3
1.2	Example cross section of a photonic crystal fibre (from RP-photonics.com). Grey and white represent areas of different refractive index. . . . .	5
2.1	Frequency as a function of wavevector for an exciton-polariton mode in bulk GaAs showing an anticrossing at the exciton resonance frequency, $\omega_{\text{ex}} = 1.515$ eV (the horizontal dashed line). The vertical dashed line shows the wavevector of the optical photon. This anticrossing is characteristic of the strong coupling regime. . . . .	13
2.2	A Fabry-Pérot, one dimensional cavity formed by an $m\lambda/2$ dielectric layer sandwiched between two dielectric Bragg mirrors consisting of alternate $\lambda/4$ layers with different dielectric constants. . . . .	14
2.3	An example mode spectrum for a microcavity. The Q-factor of the cavity for the resonance at $\omega = \omega_c$ is given by $Q = \omega_c/\delta\omega_c$ while the finesse is given by $F = \Delta\omega_c/\delta\omega_c$ . . . . .	15
2.4	A typical polariton dispersion curve (solid lines) and the dispersion of the uncoupled photon and exciton modes (dashed lines). (Taken from [1]) . . . . .	16
2.5	The Whispering Gallery at St. Paul's Cathedral, London. . . . .	19
2.6	Spherical Bessel functions of the first kind $j_l(kr)$ (top) and spherical Neumann functions, $n_l(kr)$ (bottom), for $l = 0, 1, 2$ shown in black, red and green respectively. . . . .	25

2.7	Dependence of the power reflection coefficient on the radius of a GaAs sphere (refractive index $n = 3.7$ ) in vacuum at a frequency corresponding to the exciton resonance, $\hbar\omega = 1.515$ eV. The red lines show TE modes with $l = 1, 2$ and $3$ from left to right while the black lines show TM modes, again with $l = 1, 2$ and $3$ from left to right. . . . .	28
2.8	The minimum sphere radius below which a mode of quantum number $l$ cannot be supported at a frequency of $\hbar\omega = 1.515$ eV. The dashed lines give the predictions of Equations 2.48 and 2.49 for a GaAs sphere (refractive index $n = 3.7$ ) in vacuum. The solid symbols give the actual radius of appearance of modes. The TE-polarisation is shown in black and the TM-polarisation in red. . . . .	30
2.9	Three TE modes with increasing quantum number $l = 1, 2$ and $3$ and $m = 0$ . The radius of the sphere, marked in black, increases from left to right as $l$ increases as a bigger sphere is needed to support the mode. Blue represents areas of low field intensity while red shows areas of high field intensity. . . . .	32
2.10	The decay constant, $\gamma$ for modes with different $l$ in a GaAs sphere in vacuum. The dashed lines represent the approximation given by Equation 2.54 while the symbols show the actual values given by the iterative computer program. The TE-polarisation is shown in black and the TM-polarisation in red. . . . .	33
2.11	Decay constant as a function of radius for bare cavity modes in a GaAs sphere in vacuum. The real part of the frequency is equal to the exciton resonance frequency for excitons in GaAs, $\hbar\omega_{\text{ex}} = 1.515$ eV. The TE(TM)-polarised modes are shown in black (red) and are labelled $lN$ . The horizontal line indicates the estimated polariton splitting value calculated by Equation 2.59. . . . .	35

2.12	Decay constant as a function of radius for bare cavity modes in a GaN sphere in vacuum. The real part of the frequency is equal to the exciton resonance frequency for excitons in GaN, $\hbar\omega_{\text{ex}} = 3.502$ eV. The TE(TM)-polarised modes are shown in black (red) and are labelled $lN$ . The horizontal line indicates the estimated polariton splitting value calculated by Equation 2.59. . . . .	36
2.13	Decay constant as a function of radius for bare cavity modes in a ZnO sphere in vacuum. The real part of the frequency is equal to the exciton resonance frequency for excitons in ZnO, $\hbar\omega_{\text{ex}} = 3.386$ eV. The TE(TM)-polarised modes are shown in black (red) and are labelled $lN$ . The horizontal line indicates the estimated polariton splitting value calculated by Equation 2.59. . . . .	37
2.14	Exciton-polariton modes of GaAs. The TM20 mode is shown in red and the TE30 mode is shown in green. The square points show the real part of the exciton-polariton eigenfrequency for each mode while the vertical bars give the decay constant of the mode at each radius. The black lines mark the real part of the bare cavity modes and the exciton energy (horizontal line) for comparison. . . . .	39
2.15	Exciton-polariton modes of GaN. The TM20 mode is shown in red and the TE30 mode is shown in green. The square points show the real part of the exciton-polariton eigenfrequency for each mode while the vertical bars give the decay constant of the mode at each radius. The black lines mark the real part of the bare cavity modes and the exciton energy (horizontal line) for comparison. . . . .	40
2.16	Exciton-polariton modes of ZnO. The TM20 mode is shown in red and the TE30 mode is shown in green. The square points show the real part of the exciton-polariton eigenfrequency for each mode while the vertical bars give the decay constant of the mode at each radius. The black lines mark the real part of the bare cavity modes and the exciton energy (horizontal line) for comparison. . . . .	41

3.1	Surface plasmons may propagate along the interface between a dielectric and a metal in the $x$ -direction. . . . .	47
3.2	The dispersion relations for a photon (black) and a surface plasmon-polariton (red) at an interface between gold and $\text{SiO}_2$ . The SPP dispersion lies outside the light cone of bulk $\text{SiO}_2$ . . . . .	50
3.3	A planar structure to support a Tamm plasmon-polariton. The yellow represents the metal layer, the two shades of blue represent the periodic layers of the dielectric Bragg reflector. The TPP is formed at the interface between the metal and the first Bragg reflector layer. . . . .	52
3.4	The reflection spectra for planar Bragg reflectors with alternating layers of refractive index $n_A = 2.37$ , $n_B = 1.47$ . The black line shows the spectrum for a structure with 12 pairs of layers; red is for 8 pairs of layers and green is for 4 pairs of layers. The thickness of each layer of the Bragg reflector was chosen to give maximum reflection, and to centre the photonic stop band, at a frequency of 1.0 eV. . . . .	53
3.5	Two virtual interfaces, left (L) and right (R) in a homogeneous medium a distance $x$ apart with fields incident upon each boundary ( $A_R$ and $A_L$ ) and the fields reflected from each boundary where $r_R$ and $r_L$ are the amplitude reflection coefficients from the right and left respectively. . . . .	54
3.6	In the cylindrical coordinate system $\rho$ is the radial vector, $\phi$ is a vector giving the azimuthal angle and $z$ is parallel to the cylinder axis. . . . .	59
3.7	Function $J_m(x)$ for $m = 0$ (black line) and $m = 1$ (red line). . . . .	60
3.8	Function $N_m(x)$ for $m = 0$ (black line) and $m = 1$ (red line). . . . .	60
3.9	Function $I_m(x)$ for $m = 0$ (black line) and $m = 1$ (red line). . . . .	64
3.10	Function $K_m(x)$ for $m = 0$ (black line) and $m = 1$ (red line). . . . .	64
3.11	Dispersion curves for cylindrical surface plasmons on the inside of gold tubes ( $\omega_p = 8.9$ eV) with various radii and filled with air. The black line shows the dispersion curve for the similar planar system. Red indicates a tube radius of 1000 nm, green = 400 nm, blue = 80nm, cyan = 50 nm, magenta = 30 nm and orange = 10 nm. The dashed line marks the cut off at $\omega = c\beta$ . . . . .	67

3.12	Colladon's <i>light fountain</i> demonstration, published in <i>La Nature</i> , 1884. Light focused by a lens onto an aperture in a container of water causes the light to be confined to the stream by total internal reflection. . . .	69
3.13	The $E_\rho$ field component for a structure with a 100 nm radius metal core surrounded by a 50 nm thick layer of silica, a 200 nm thick layer of silicon and air. The vertical dashed lines indicate the boundary between each of the layers. . . . .	71
3.14	Dispersion relation for the fundamental mode in a structure with a 200 nm core of refractive index $n = 2.37$ surrounded by a layer of refractive index $n = 1.47$ and infinite metal cladding. Colours indicate the thickness of the middle, low refractive index layer: solid black = 0 nm (no low refractive index layer), red = 25 nm, green = 50 nm, blue = 100 nm, cyan = 200 nm and magenta = 400nm. The dashed black line is for the case with an infinite low refractive index layer and no metal. . . . .	72
3.15	A cylindrical fibre aligned along the $z$ -axis with a core region surrounded by layers of different refractive index, shown in blue and white. The dotted region represents repetition of the alternative refractive index layers. $\rho_c$ and $\rho_f$ indicate the radii of the core and the final layer of the structure respectively. . . . .	73
3.16	The round trip phase difference in a dielectric layer (blue) adjacent to a metal core (orange) is given by the phase change on reflection from the Bragg reflector ( $r_1$ ), the phase change on reflection from the metal ( $r_2$ ) and twice the phase change of a wave travelling across the dielectric layer marked $x$ . The dots represent repeated layers of the Bragg reflector. Key radii are marked: $\rho_c$ is the core radius, $\rho_1$ is the outer radius of the first dielectric layer and $\rho_f$ is the outer radius of the final layer of the structure. . . . .	75

3.17	The round trip phase difference in a dielectric layer (blue) adjacent to essentially infinite metal cladding outside (orange) is given by the phase change on reflection from the Bragg reflector ( $r_3$ ), the phase change on reflection from the metal ( $r_4$ ) and twice the phase change of a wave travelling across the dielectric layer marked $x$ . The dots represent repeating layers of the Bragg reflector. . . . .	76
3.18	Bessel function of the first kind in a medium of refractive index $n = 2.37$ with frequency 1.0 eV. The first node occurs at a radius 200 nm.	85
3.19	a) TE mode: the $E_\phi$ (black line) and $cB_z$ (red line) fields for a BR structure with TiO <sub>2</sub> core with radius 200 nm surrounded by 8 pairs of SiO <sub>2</sub> /TiO <sub>2</sub> layers at a frequency 0.9792 eV. b) TM mode: the $E_z$ (black line) and $cB_\phi$ (red line) fields for a BR structure with TiO <sub>2</sub> core with radius 200 nm surrounded by 8 pairs of TiO <sub>2</sub> /SiO <sub>2</sub> layers at a frequency 0.9942 eV. . . . .	86
3.20	The reflection spectrum (black, magnitude and red, phase) for a cylindrical DBR with a core refractive index $n_c = 2.37$ and 8 pairs of surrounding layers with refractive indices $n_1 = 1.47$ and $n_2 = 2.37$ . The thicknesses of each layer of the DBR were chosen to be $\lambda/4$ giving effective reflection, and centring the photonic stop band, at a frequency of 1.0 eV. . . . .	88
3.21	Solid lines represent the dispersion curves for a TE (green) and TM (blue) mode whose field profiles for $\beta = 0$ are shown in Figure 3.19. For comparison, the dispersion curves of modes in a simple optical fibre structure with a TiO <sub>2</sub> core ( $n = 2.37$ ) and SiO <sub>2</sub> ( $n = 1.47$ ) cladding are shown as dashed lines: TE, $m = 0$ mode (green) and TM $m = 0$ (blue). All confined modes in this simple optical fibre have dispersion curves that lie between the dashed black lines. . . . .	89
3.22	The phase of the reflection coefficient calculated from the outside of the Bragg reflector structure for a TM mode in a structure with a 150nm TiO <sub>2</sub> core and 9 pairs of SiO <sub>2</sub> / TiO <sub>2</sub> layers shows a sharp feature at frequency 0.9234 eV. . . . .	91

3.23	Phase of the reflection coefficient, $r_1$ , from the inside of a Bragg reflector varying with frequency across the photonic band gap for the TE polarisation as calculated from Equation 3.74. . . . .	92
3.24	The $E_\phi$ (black) and $cB_z$ (red) fields components for a TE mode with $m = 0$ , $\beta = 0$ in a Bragg reflector structure with a 30 nm metal core, a 201 nm thick $\text{TiO}_2$ layer and 8 pairs of $\text{SiO}_2/\text{TiO}_2$ layers. The vertical dashed line indicates the edge of the metal core. The mode frequency is 0.9792 eV. . . . .	93
3.25	a) TE mode with $\beta = 0$ and frequency 1 eV in a multilayer structure with a metal core of radius 30 nm and $\text{TiO}_2$ layer adjacent to the metal with thickness of 426 nm. The black line shows the $E_\phi$ field component while the red line shows the $cB_z$ field component. b) TM mode with $\beta = 0$ and frequency 1 eV for the same structure but with an adjacent $\text{TiO}_2$ layer thickness of 346 nm. The black line shows the $E_z$ field component while the red line shows the $cB_\phi$ field component. All boundaries are marked with vertical dashed lines. . . . .	94
3.26	The solid lines show the dispersion curves for $m = 0$ , TE (black) and TM (red) modes for the structures required to give a mode frequency at $\beta = 0$ of 1 eV. The dashed lines show the dispersion curves for the same structures with the metal core removed and replaced by $\text{TiO}_2$ . . . . .	95
3.27	a) TE mode with $\beta = 0$ and frequency 0.9976 eV in a multilayer structure with a $\text{TiO}_2$ core of radius 456 nm surrounded by 8 pairs of $\text{SiO}_2/\text{TiO}_2$ layers. The black line shows the $E_\phi$ field component while the red line shows the $cB_z$ field component. b) TM mode with $\beta = 0$ and frequency 0.9200 eV for the same structure but with a $\text{TiO}_2$ core of radius 376 nm. The black line shows the $E_z$ field component while the red line shows the $cB_\phi$ field component. All interfaces are marked with vertical dashed lines. . . . .	97
3.28	Variation of mode frequency with varying thickness of the $\text{TiO}_2$ layer adjacent to the metal core for $m = 0$ and $m = 1$ . . . . .	98

3.29	The $E_z$ (black) and $cB_\phi$ (red) field components of a TM mode of frequency 1.0 eV in a cylindrical structure with 150 nm $\text{TiO}_2$ core, 14 pairs of $\text{TiO}_2/\text{SiO}_2$ Bragg reflector layers (of thickness 131 nm and 211 nm respectively), a $\text{SiO}_2$ cavity layer of thickness 400 nm all surrounded by essentially infinite metal. . . . .	99
3.30	The $cB_z$ (red) and $E_\phi$ field components of a TE mode with frequency 1 eV and $\beta = 0$ in a structure with a $\text{TiO}_2$ core of radius 150 nm surrounded by 14 pairs of $\text{SiO}_2/\text{TiO}_2$ layers, where the $\text{SiO}_2$ layers have thickness 211 nm and the $\text{TiO}_2$ layers have thickness 131 nm. The $\text{TiO}_2$ cavity layer adjacent to the metal surrounding the structure has a thickness of 130 nm. Vertical dashed lines mark the dielectric boundaries. . . . .	100
3.31	The $E_z$ field component for two split modes, one with frequency 1.00406 eV (black line) and the other 1.00589 eV (red). Both were calculated for $m = 1, \beta = 0$ in a structure consisting of: a metal core of radius 30 nm; a $\text{SiO}_2$ cavity layer adjacent to the core of thickness 483 nm; 14 pairs of layers alternating $\text{TiO}_2/\text{SiO}_2$ with respective thickness 131 nm/ 211 nm; a final $\text{TiO}_2$ cavity layer of thickness 370 nm adjacent to the semi-infinite metal cladding outside. . . . .	101
3.32	The split dispersion curves for a structure with a metal core and a metal cladding as described in Figure 3.31. The black line is the dispersion curve for the symmetric mode and the higher frequency, red line is for the antisymmetric mode. This structure has only 10 pairs of layers in the Bragg reflector rather than the 14 pairs in Figure 3.31 to enhance the splitting and hence show it more clearly. . . . .	103
4.1	Representations of one-, two- and three-dimensional photonic structures (left to right). Different colours represent homogeneous blocks of material with different values of dielectric constant, $\epsilon$ . . . . .	107
4.2	The power transmission coefficient for a planar Bragg reflector structure with a cavity defect at its centre. The defect mode can be seen as a peak in the transmission spectrum dip. . . . .	110

4.3	An $x$ - $z$ plane view of the structure of a hexagonal array of cylindrical air holes (dark blue) in a slab of semiconductor (light blue) showing the lattice parameter, $a$ . The $y$ -direction is out of the page. . . . .	115
4.4	The colours in the grid represent the different refractive indices that are assigned to each square. Squares completely inside the circle have one refractive index, squares completely outside the circle have another. The grid on the right has twice as many squares as that on the left and the circle is more clearly defined. . . . .	116
4.5	Screen shot of the ideal structure as it appears in <i>OmniSim</i> . The radius of each air cylinder is $0.4a$ where $a$ is the lattice parameter. The light blue background represents the substrate material. The photonic crystal has varying dielectric constant in the $x$ - $z$ plane and is homogeneous in the $y$ -direction. The excitor (yellow) and the two sensors (red) are indicated. . . . .	119
4.6	The band structure for TM (black) and TE (red) polarised light in a GaN slab (refractive index $n = 2.43$ ) with a hexagonal array of cylindrical air holes each with radius $0.4a$ . The inset shows the first Brillouin zone of the ideal crystal and marks the wavevector directions within the crystal. . . . .	120
4.7	Relative transmission of a TM pulse across an ideal photonic crystal structure such as that shown in Figure 4.5 with GaN as the background material. . . . .	121
4.8	The distribution of cylinder radii depending on the disorder parameter, $\delta$ . . . . .	121
4.9	An example disordered structure as it appears in <i>OmniSim</i> . The radius of each cylinder is randomly attributed from a distribution about $r_0 = 0.4a$ where $a$ is the lattice parameter, as shown in Figure 4.8. . . . .	122

4.10	Relative transmitted flux as a function of frequency for the ideal structure (thick black line) with background refractive index $n = 2.7$ , a randomly disordered structure with $\delta = 0.18$ (thin black line) and the mean relative transmitted flux for 10 random configurations of disorder parameter $\delta = 0.18$ (red). . . . .	125
4.11	The mean (solid black) and standard deviation (red) of transmitted flux in the mid $1/20^{th}$ of the photonic band gap for structures with background refractive index a) $n = 1.8$ , b) $n = 2.0$ , c) $n = 2.2$ , d) $n = 2.43$ , e) $n = 2.7$ . The dotted black line shows the one standard deviation error bound on the mean. The green construction lines show the threshold disorder, $\delta_{th}^F$ (right) and the lower error bound (left). . . . .	127
4.12	Threshold disorder parameter $\delta_{th}^F$ , defined as the point at which the standard deviation of the relative transmitted flux becomes greater than the mean, as a function of the relative band width $\Delta\omega/\omega_0$ . . . . .	128
4.13	The Fourier transformed $H_y$ field component at sensor 2 for a 2D hexagonal photonic crystal. . . . .	132
4.14	Energy flow per unit frequency into scattering angle $\theta$ for the ideal structure (black) and one configuration each of four levels of disorder: $\delta = 0.05$ (red), $\delta = 0.10$ (green), $\delta = 0.15$ (blue) and $\delta = 0.20$ (cyan). . . . .	134
4.15	Total energy in the ballistic (solid symbols) and scattered (open symbols) light passing through sensor 2 for structures with background refractive index: $n = 1.8$ (black), $n = 2.0$ (red), $n = 2.2$ (green), $n = 2.43$ (blue), $n = 2.7$ (cyan) and $n = 3.0$ (magenta). The vertical dashed lines indicate the disorder parameter at which the energy in the scattered light exceeds that in the ballistic light. . . . .	135
4.16	Threshold disorder, $\delta_{th}^E$ defined as the point at which the energy in the scattered light becomes greater than the energy in the ballistic light, as a function of relative band width with a trend line fit. . . . .	136
4.17	Threshold disorder, $\delta_{th}^F$ as a function of mean refractive index with a trend line fit. . . . .	138

4.18	Threshold disorder parameter, defined as the point at which the energy in the scattered light becomes greater than the energy in the ballistic light, as a function of mean refractive index. The red trend-line shows the fit given by Equation 4.38 and the green line shows the fit given by Equation 4.39. . . . .	139
4.19	Upper and lower band edges for the complete band gap of an ideal photonic crystal structure with all the air holes having radius $r$ . Black represents a structure with background refractive index $n = 1.8$ , red represents $n = 2.2$ and green represents $n = 2.7$ . The horizontal dashed lines indicate the frequency at the centre of the band gap for the case of air holes with radius $r = 0.4 \mu\text{m}$ . . . . .	140

# Chapter 1

## Introduction

### 1.1 Light-matter interactions

Techniques for controlling electromagnetic radiation are currently of great interest. In particular, this thesis considers light-matter interactions which are interesting both from a fundamental point of view and in terms of their applications. The interaction of light with matter allows for direct control of the properties of light. For example, group velocity, dispersion characteristics and the formation of part-light, part-matter quasiparticles may be controlled. Mathematically, a quasiparticle is an eigenstate of the Hamiltonian describing the relevant many-body problem. Physically, the excitation may be considered as a particle with its own effective mass and properties distinct from those of its constituent parts. One topical example is the Bose-Einstein condensation of quasiparticles formed from the interaction between excitons and photons, known as exciton-polaritons.

Photonics is the study, design and fabrication of materials and structures with particular optical properties, for example: frequency stop-band filters; waveguiding; confinement of light; resonant cavities or specific dispersion characteristics. These desirable effects are produced by selecting the structure of materials so that light interacts with areas of differing refractive index, or with features such as excitations, within the material. Photonics has found application in many different areas of technology, including (but not limited to) telecommunications, medicine, security and defence, with new applications being proposed all the time. There is currently great

interest in creating optical analogues of electronic chip components such as switches and logic gates. Just as fibre optic cables revolutionised the telecommunications industry, photonics more generally has the potential to replace electronic systems with faster, smaller, more efficient components with wide bandwidths. A major challenge is to be able to produce such optical components that are both technically and economically competitive with current electronic devices and systems.

In order for optical components to carry out the same role as electronic integrated circuit features, they need to be able to operate on a nanometer scale. Nanophotonics involves the control and manipulation of light in a subwavelength regime as the wavelength of visible light is around 400 - 700 nm. Nanoscale light-matter interactions generally require either the light to be confined to the nanoscale or the material to have dimensions of this order of magnitude [2]. In this thesis we are mainly concerned with restricting the size of the matter component. Nanoscale materials include quantum wells, wires and dots. In semiconductor materials, this quantum confinement causes changes to the electronic band structure and hence to the optical properties of the material. Nanoparticles also exhibit different optical properties to their bulk counterparts due to their small size and high surface area to volume ratio. Another example of material confined to nanometer dimensions is the photonic crystal which is discussed later in this chapter.

It is interesting to note that for the majority of papers cited in this thesis, the phenomena being studied have been proposed theoretically before being studied in experiments. This shows that theoretical studies, both introducing new phenomena and looking at established phenomena in new ways, are crucial for driving forward our optoelectronic industries. The work reported in this thesis uses computations to model light-matter interactions. We investigate the effects of using matter to confine light in different ways. Chapters 2 and 3 focus on part-light, part-matter quasiparticles and the structures required for their formation. Chapter 4 focuses on photonic crystal structures and how deviation from the perfect crystal affects their ability to control light.

## 1.2 Photonic crystals and the Bragg reflector

To control the light-matter interaction we need to be able to control light. One way to do this is with photonic crystals. Photonic crystals are structured materials, with a periodic variation in dielectric properties. The period of the variation is of the order of the wavelength of light and this gives rise to the interesting optical properties that the photonic crystals possess. Currently, one of the most widely used photonic structures for controlling light is the dielectric mirror, known as a Bragg reflector.

### 1.2.1 The Bragg reflector

A Bragg reflector is a periodic structure, consisting of layers of material with alternating refractive index  $n_1$  and  $n_2$ , a one-dimensional photonic crystal, as illustrated in Figure 1.1. When light is incident on one of the dielectric boundaries, such as

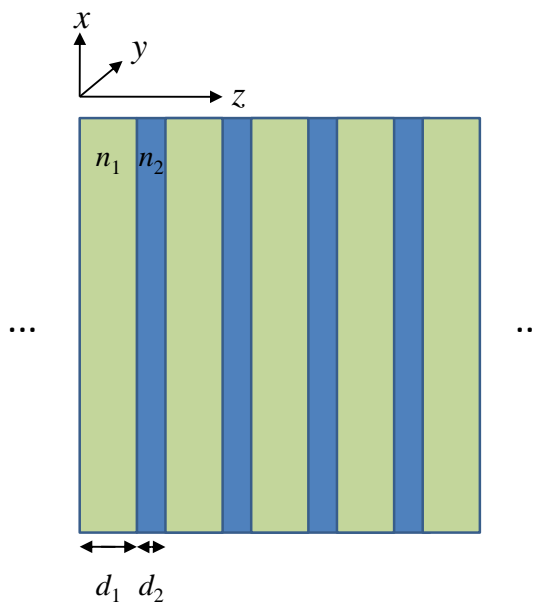


Figure 1.1: A structure consisting of alternating layers of different refractive index acts as a near-perfect mirror for light of certain wavelength. The greater the number of layers the more effective the mirror.

between layers of refractive index  $n_1$  and  $n_2$ , the beam is partially reflected and par-

tially transmitted in accordance with the Fresnel equations. For the case of multiple boundaries in the same structure, the many reflected and refracted waves interfere with each other. Typically, each layer in a Bragg reflector structure has the same optical thickness:

$$n_1 d_1 = n_2 d_2 \quad (1.1)$$

where  $d_1$  and  $d_2$  are the physical thicknesses of layers with refractive index  $n_1$  and  $n_2$  respectively. For a particular frequency of light, if the optical thickness of each layer is equal to one quarter of the free space wavelength, then the many reflected beams of light are in-phase and therefore interfere constructively with one another. For Bragg reflector structures with a sufficient number of layers, this constructive interference results in a reflectivity close to unity, at and around the given frequency. Bragg reflectors are therefore highly effective mirrors for a certain frequency range. The frequency range that is reflected by the Bragg reflector is called the photonic band gap. In a planar structure, such as that illustrated in Figure 1.1, the photonic band gap prevents light (of the appropriate frequency) from propagating through the structure in the  $x$ - $z$  plane.

Bragg mirrors are generally preferred over traditional metal mirrors in photonics as they have significantly lower losses. Two Bragg reflectors on either side of a cavity layer create a Fabry-Pérot cavity in which light, of an appropriate frequency, may be confined due to repeated reflection. This device is used, for example, in the gain medium of solid state lasers.

It is also possible to have cylindrical and spherical Bragg reflectors by arranging the layers of material with alternating properties in these geometries. In these cases the basic physics is similar to the planar case but the detailed description is more challenging. A description of the cylindrical Bragg reflector may be found in [3] and the spherical case in [4]. In this thesis, an application of the cylindrical Bragg reflector will be considered.

## 1.2.2 Photonic crystals

Although the Bragg reflector was a well established optical component at the time, the term *photonic crystal* was not introduced until the works of Yablonovitch [5]

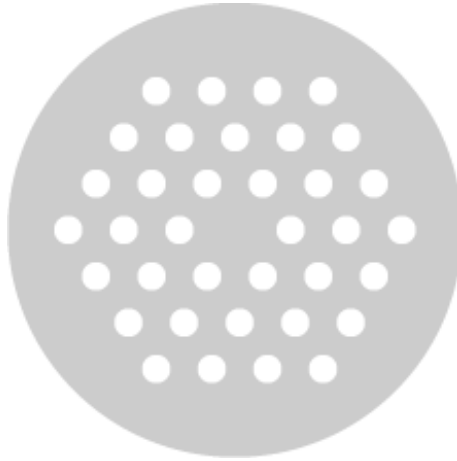


Figure 1.2: Example cross section of a photonic crystal fibre (from RP-photonics.com). Grey and white represent areas of different refractive index.

and John [6] in 1987 that referred to photonic crystals in two- and three-dimensions. Photonic band gaps, such as those occurring in one-dimensional structures, are also exhibited by some higher-dimensional photonic crystals. An advantage of photonic crystals with a periodic variation in refractive index in two or three-dimensions is that their band gap exists for light travelling in more than one direction in the material. The theory of band gaps in photonic crystals is now well established and an introductory treatment may be found in Joannopoulos *et al.* [7]. A further, more detailed, photonic crystals text is that by Lourtioz *et al.* [8]

Two-dimensional photonic crystal slabs containing features such as channels or cavities make use of localised modes within the photonic band gap to guide or confine light within the material [9]. This has led to the production of devices such as waveguides, resonant cavities and optical filters. Lasers have been produced making use of cavity modes related to isolated defects in photonic crystals [10] [11].

Photonic crystal fibres consist of a periodic lattice, for example, of dielectric cylinders with capillary air holes at their centres, drawn together into a fibre. Some photonic crystal fibres have a core region in which light may be confined due to the photonic band gap created by the pattern of alternating dielectric, air regions surrounding the core [12]. A photonic crystal fibre cross section is illustrated in Figure 1.2. Photonic crystal fibres guide light using a photonic band gap, while traditional step-index fibres use total internal reflection. The advantages of photonic

crystal fibres include lower levels of loss when the fibre is bent and better confinement of light to the core [13].

More recently photonic crystals have been designed in order to control the dispersion of light, leading to novel effects such as ‘slow light’ and negative refraction [14]. One interesting application of negative refraction is imaging, where certain materials may be used to image objects below the classical diffraction limit [15]. Another development concerns photonic crystals containing metal, for example an array of metal cylinders in air. These have been shown to exhibit photonic band gaps in much the same way as their all-dielectric counterparts [16]. The metallic photonic crystals can suffer from high absorption losses due to the metal but on the other hand allow for smaller devices due to the much smaller lattice constant required to produce a band gap at the same frequency.

The photonic band gap is an important feature of photonic crystal structures and is utilized in many applications. It is well known that disorder causes degradation of the photonic band gap by causing states to appear in the gap. These states lead to the photonic band gap narrowing and eventually, for high enough disorder, closing. Disorder can take the form of any random deviation from the perfect, or ideal, crystal structure and may be the result of manufacturing processes. For example, a one-dimensional photonic crystal may have disorder in the thickness of its layers. In two-dimensions photonic crystals formed from an array of air holes in a slab of dielectric material may have disorder in the size or shape of the holes. It is important to understand the effects of disorder on the band gap so that device manufacturers know how much disorder is acceptable before their photonic crystals will no longer operate effectively.

An empirical relationship exists between the relative band width for ideal photonic crystals and the ‘amount’ of disorder required to close the photonic band gap [17]. Due to the increased complexities in the two-dimensional system, as yet, no quantitative relationship, applicable to a range of photonic crystals, has been found. Chapter 4 of this thesis investigates the effect of disorder of the relative band width of two-dimensional photonic crystals.

## 1.3 Polaritons

Polaritonics is an emerging branch of photonics. Polaritons are part-light, part-matter quasiparticles that are formed when an electromagnetic field interacts resonantly with a particle carrying charge or a dipole. There are many different types of polariton with different matter contributions. In this thesis we specifically consider exciton-polaritons and Tamm plasmon-polaritons, a type of surface plasmon-polariton. The formation of these polaritons and, in particular, the structures in which each of the two types of polariton may exist are investigated.

### 1.3.1 Exciton-polaritons

Exciton-polaritons were first observed in planar semiconductor microcavities in 1992 by Weisbuch *et al.* [18]. Since then the study of exciton-polariton phenomena has captivated the attention of many research groups and the number of papers published on the topic has grown exponentially. Many interesting effects have been shown to occur with exciton-polaritons, including, for example, Bose-Einstein condensation [19] [20] and polariton lasing [21] [22]. Prototype devices using exciton-polaritons have been proposed and demonstrated, for example optical switches [23] [24], polarisation-controlled logic gates [25] [26] and integrated circuits [27]. Much of the work carried out on exciton-polaritons has been done in planar microcavities but recent advances in fabrication technology have allowed for increasingly high quality microcavities in other geometries. Higher-dimensional microcavities have obvious advantages over the planar system as they can confine light in more than one direction. In particular, studies have been carried out on pillar microcavities [28], and related cylindrical geometries [29]. In this thesis a theoretical description of a method of producing exciton-polaritons in submicron spheres is presented.

### 1.3.2 Surface plasmon-polaritons and Tamm plasmon-polaritons

Surface plasmon-polaritons can exist at the surface of a metal in vacuum or at a metal dielectric interface. In this case the matter component is the coherent oscilla-

tion of the electrons in the metal against the fixed background of the positive metal ions. Surface plasmons were first studied by Ritchie in the 1950s [30] and have found numerous applications in a wide range of areas; for example, their use is well established in commercial sensors for molecular biological systems [31]. A comprehensive review of surface plasmon-polaritons is given by Pitarke *et al.* [32]. More recently the study of surface plasmon-polaritons in nanostructured materials has resulted in plasmonics becoming a highly topical branch of photonics. In such structures, the confinement length of surface plasmon-polaritons is less than their wavelength [33] leading to some interesting phenomena. For example, it has been shown that surface plasmon-polaritons play a role in the enhancement of transmission of light through an array of subwavelength holes in a metal film [34]. A comprehensive review of work on light passing through subwavelength apertures is given in [35]. Surface plasmon-polaritons in metal nanoparticles have been demonstrated for use as biosensing tags [36]. Surface plasmon-polaritons have also been used in subwavelength imaging [37], optical switching [38] and are promising candidates for use in photonic circuits [33] [39] [40].

Tamm plasmon-polaritons are a relatively new concept having been proposed in a planar system in 2007 by Kaliteevski *et al.* [41] and subsequently demonstrated experimentally by Sasin *et al.* in 2008 [42]. They are a type of surface plasmon-polariton that exist at the interface between a Bragg reflector structure and a metal. Since being demonstrated they have been considered for use in polariton lasers [43], polariton integrated circuits [44], all-optical diodes [45], optical absorbers [46] and optical switches [47]. The fundamental properties and interactions of Tamm plasmon-polaritons have also been studied by various groups. For example, they have been shown to exhibit strong coupling with quantum well excitons [48] and exciton-polaritons [49]. The inclusion of metal in a step-index optical fibre, either in the core, as a thin layer between the core and the cladding or as an additional cladding layer, has been shown to allow surface plasmon-polaritons to exist at the metal dielectric interface in cylindrical structures [50] [51]. In this thesis, the use of Tamm plasmon-polaritons in cylindrical structures is investigated. Instead of a traditional optical fibre, we consider multilayer cylindrical Bragg reflector structures

with metallic features either in the core or cladding or both of these locations.

## 1.4 Theoretical framework

The four Maxwell equations fundamentally describe the propagation of electromagnetic fields in time and space. They are given below in SI units which are used throughout this thesis.

$$\nabla \cdot \mathbf{E} = \frac{\rho}{\varepsilon_0} \quad (1.2)$$

$$\nabla \cdot \mathbf{B} = 0 \quad (1.3)$$

$$\nabla \times \mathbf{E} = -\frac{\partial \mathbf{B}}{\partial t} \quad (1.4)$$

$$\nabla \times \mathbf{B} = \mu_0 \mathbf{J} + \mu_0 \varepsilon_0 \frac{\partial \mathbf{E}}{\partial t} \quad (1.5)$$

Here  $\mathbf{E}$  is the electric field vector,  $\mathbf{B}$  is the magnetic field vector,  $\rho$  is the total charge density,  $\mathbf{J}$  is the total current density,  $\mu_0$  is the permeability of free space,  $\varepsilon_0$  is the permittivity of free space and  $t$  is time. The permittivity and permeability of free space are related to the speed of light in vacuum,  $c$  by the relation:

$$c = \frac{1}{\sqrt{\varepsilon_0 \mu_0}}. \quad (1.6)$$

Two other quantities that are routinely referred to in electromagnetism are the electric displacement field,  $\mathbf{D}$  and the magnetic field strength,  $\mathbf{H}$ . These are related to the electric and magnetic field by the relations:

$$\mathbf{D} = \varepsilon \varepsilon_0 \mathbf{E} \quad (1.7)$$

$$\mathbf{B} = \mu \mu_0 \mathbf{H} \quad (1.8)$$

where  $\varepsilon$  and  $\mu$  are the relative permittivity and relative permeability respectively. Throughout this thesis the materials under consideration are non-magnetic and so we take  $\mu$  to be unity. We consider dielectric materials where the relative permittivity does not vary appreciably with frequency within the range of frequencies considered, and hence, we may write the refractive index,  $n$  as:

$$n = \sqrt{\varepsilon \mu} \quad (1.9)$$

which reduces to  $n = \sqrt{\varepsilon}$  for the case of interest,  $\mu = 1$ .

## 1.5 Outline of the thesis

This thesis presents work focusing on two different types of polariton, each in a particular dielectric system and geometry. Chapter 2 investigates the conditions required for the formation of exciton-polaritons in spherical microcavities with sub-micron diameters. Spheres made of three different materials are considered: gallium arsenide, gallium nitride and zinc oxide. The results for each case are compared and discussed. The work carried out on gallium arsenide has been published in ‘Whispering-Gallery Exciton Polaritons in Submicron Spheres’ under the authors maiden name [52].

Chapter 3 introduces Tamm plasmon-polaritons and the formalism put forward by Kaliteevski *et al.* [41] which hypothesises their existence in planar structures. To allow for the prediction of Tamm plasmon-polaritons in cylindrical multilayer structures the method has been extended to the cylindrical coordinate system. Particular consideration is given to the effect of the position of the required metallic features in the structures.

In Chapter 4 we turn our attention to photonic crystal structures. The effect of disorder in two-dimensional photonic crystal structures is considered, specifically the effect of hole radius in a photonic crystal consisting of air holes in a slab of dielectric material.

The thesis is concluded in Chapter 5 with a summary of the work undertaken and suggestions for further avenues of research that have not been considered.

# Chapter 2

## Exciton-polaritons in sub-micron spheres

In this chapter spherical microcavities are considered as a medium for supporting exciton-polariton quasiparticles. We first briefly consider work done on exciton-polaritons in planar and cylindrical geometries then go on to present a formalism for spherical microcavities. Specifically, the eigenfrequencies of whispering-gallery photon modes are considered along with their coupling to excitons in the materials gallium arsenide (GaAs), gallium nitride (GaN) and zinc oxide (ZnO). Evidence for the formation of exciton-polaritons in sub-micron spheres is presented.

### 2.1 Excitons

An exciton is an electron-hole pair that can be formed in a semiconductor by the absorption of a photon with sufficient energy to excite an electron from the valence to the conduction band. The amount of energy required is known as the exciton energy. Another quantity, the exciton binding energy is defined as the amount of energy required to separate the bound electron-hole pair to form ‘free’ carriers. The exciton binding energy gives an idea of the stability of the exciton. There are two main theoretical models for excitons: Frenkel excitons and Wannier-Mott excitons. Frenkel excitons are highly localised, tightly bound and are typically found in ionic and molecular materials. In contrast Wannier-Mott excitons are weakly bound and

have an electron-hole separation much larger than the lattice parameter of their host material. They are characteristic of materials with relatively high dielectric constant and low electron effective mass, such as GaAs and many other inorganic semiconductors [53]. The typical radius of a Wannier-Mott type exciton is 1-10nm and they have binding energies of around 0.1-10 meV [54]. Excitons are charge neutral and have integer spin and so obey Bose-Einstein statistics.

## 2.2 Exciton-polaritons

Exciton-polaritons are quasiparticles formed from the strong coupling between excitons and photons. They were first described in the pioneering works of Pekar [55], Agranovich [56] and Hopfield [57] in the 1950s. Excitons have a dipole moment due to their separated charges and upon application of an electromagnetic field at an appropriate frequency the dipole will oscillate. Both the exciton and the photon may be thought of as individual oscillators that may be joined together in analogy with the well known coupled pendula experiment. Exciton-polaritons are the result of the splitting between strongly coupled hybrid modes with both excitonic and photonic character. This splitting can be clearly seen in the solutions to the electromagnetic wave equation. In a bulk semiconductor with no excitonic contribution the wavevector,  $k$ , may be written:

$$k^2 = \frac{\varepsilon_b \omega^2}{c^2} \quad (2.1)$$

where  $\omega$  is the angular frequency and  $\varepsilon_b$  is the background dielectric constant (that of the material when no exciton is present). With the excitonic contribution included, the dielectric constant of a semiconductor,  $\varepsilon$  may be written as [58]:

$$\varepsilon = \varepsilon_b + \frac{\varepsilon_b \omega_{\text{LT}}}{\omega_{\text{ex}} - \omega - i\Gamma} \quad (2.2)$$

where  $\omega_{\text{ex}}$  is the exciton resonant frequency,  $\Gamma$  is the non-radiative decay rate of the exciton and  $\omega_{\text{LT}}$  is the bulk value of the longitudinal-transverse splitting. For simplicity  $\Gamma$  is set to zero and the variation of exciton resonance frequency,  $\omega_{\text{ex}}$  with wavevector is neglected giving:

$$k^2 = \frac{\varepsilon_b \omega^2}{c^2} \left( \frac{\omega - \omega_{\text{ex}} - \omega_{\text{LT}}}{\omega - \omega_{\text{ex}}} \right) \quad (2.3)$$

For  $k \rightarrow 0$  there are two solutions for the frequency:  $\omega \rightarrow 0$  or  $\omega \rightarrow \omega_{\text{ex}} + \omega_{\text{LT}}$ . For  $k \rightarrow \infty$  there are also two solutions:  $\omega \rightarrow \omega_{\text{ex}}$  or  $\omega \rightarrow ck/\sqrt{\epsilon_b}$ . Also for  $\omega_{\text{ex}} < \omega < \omega_{\text{ex}} + \omega_{\text{LT}}$  the numerator inside the parentheses of Equation 2.3 is negative and hence there can be no real solutions for  $k$ . The resulting  $\omega$ - $k$  dispersion is illustrated in Figure 2.1. This anticrossing is characteristic of strong coupling between an exciton and a photon and results in upper and lower exciton-polariton branches. The splitting of the modes at the anticrossing is analogous to Rabi splitting in

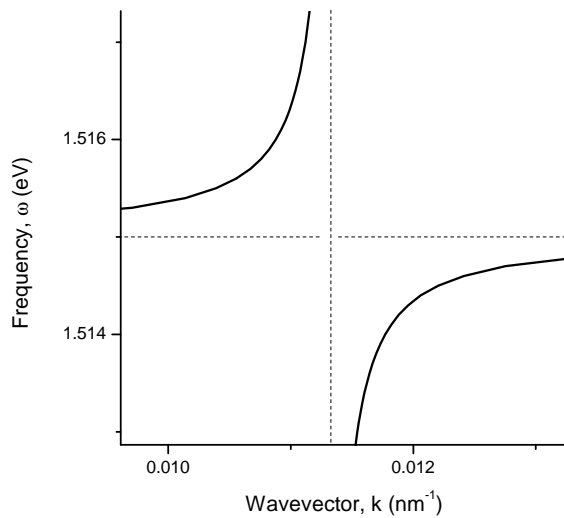


Figure 2.1: Frequency as a function of wavevector for an exciton-polariton mode in bulk GaAs showing an anticrossing at the exciton resonance frequency,  $\omega_{\text{ex}} = 1.515$  eV (the horizontal dashed line). The vertical dashed line shows the wavevector of the optical photon. This anticrossing is characteristic of the strong coupling regime.

atomic physics (where the modes of the coupled photon – interatomic transition system are split due to strong coupling) and is discussed further in Section 2.2.1.

In fact, it is difficult to study or to make use of exciton-polaritons in bulk systems because they are effectively buried in the host material. In 1992, Weisbuch *et al.* observed exciton-polaritons in a semiconductor microcavity [18]. Low-dimensional structures allow for greater control over the position of the exciton and photon than bulk systems and furthermore the microcavity design may be altered in order to give maximum control over the exciton - photon interaction [1]. Since the work of Weis-

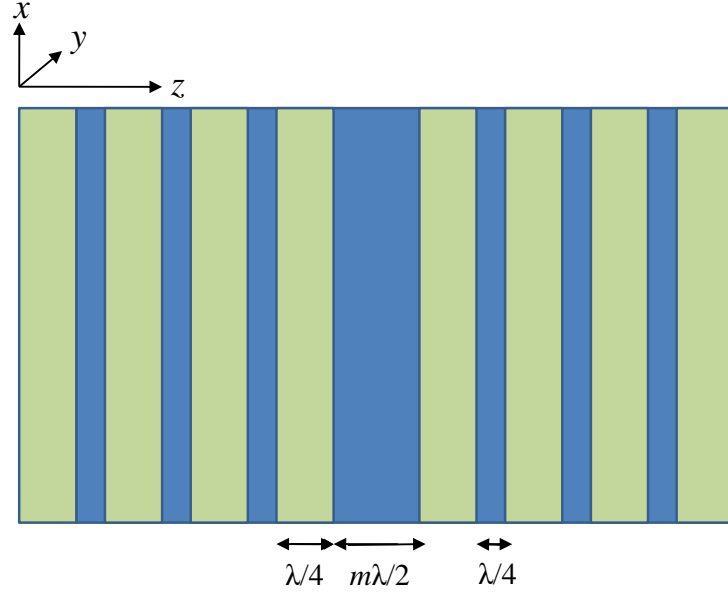


Figure 2.2: A Fabry-Pérot, one dimensional cavity formed by an  $m\lambda/2$  dielectric layer sandwiched between two dielectric Bragg mirrors consisting of alternate  $\lambda/4$  layers with different dielectric constants.

but the number of published papers referring to exciton-polaritons has increased year on year and the majority of this work has been done in planar microcavities such as the Fabry-Pérot system illustrated in Figure 2.2. The thick layer in the middle of the structure, labelled  $m\lambda/2$  represents a semiconductor microcavity with thickness equal to an integer number,  $m$ , of half wavelengths,  $\lambda/2$ , of the light in the structure. In many cases the cavity is formed in the material with the higher refractive index and  $m$  is chosen to be 2 which gives a  $\lambda$  thickness layer. This means that the electric field of the cavity mode has an antinode in the centre of the cavity [1]. Photons may be confined perpendicular to the plane of the layers, either in the microcavity itself or in a quantum well within the cavity, due to the quarter-wave Bragg reflector mirrors on either side. The thickness and dielectric constant of each of the layers in the stack are chosen such that reflections from the multiple interfaces are in-phase, giving an effective reflectivity close to unity [59].

Well confined photons have a long lifetime and so have a better opportunity to interact with excitons to form exciton-polaritons. The Q-factor of a cavity may be

defined as the ratio of the resonant frequency to the line width:

$$Q = \frac{\omega_c}{\delta\omega} \quad (2.4)$$

where  $\omega_c$  is the resonant frequency of the cavity and  $\delta\omega$  is the linewidth of the mode as depicted in Figure 2.3. As the polariton lifetime is dictated by those of the photon and the exciton, a high Q-factor indicates a greater potential polariton lifetime. Another quantity describing the cavity modes is the finesse,  $F$ , given by

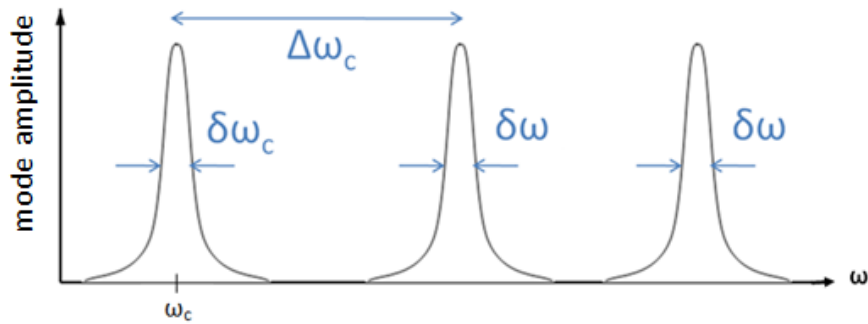


Figure 2.3: An example mode spectrum for a microcavity. The Q-factor of the cavity for the resonance at  $\omega = \omega_c$  is given by  $Q = \omega_c/\delta\omega_c$  while the finesse is given by  $F = \Delta\omega_c/\delta\omega_c$ .

the ratio of mode separation to linewidth:

$$F = \frac{\Delta\omega_c}{\delta\omega} \quad (2.5)$$

where  $\Delta\omega_c$  is the separation between cavity modes. A high finesse is desirable for forming polaritons because the mode that is coupling to an exciton will then be isolated creating distinct polariton states rather than suffering from interference from other cavity modes.

As the optical modes are confined only in one direction in a Fabry-Pérot structure, the photons have an in-plane dispersion. A coupled oscillator model can be used to calculate the in-plane dispersion, for example, Figure 2.4 shows a typical polariton dispersion curve for a planar Fabry-Pérot microcavity. The solid lines represent the dispersion of the coupled modes of the system while the dashed lines

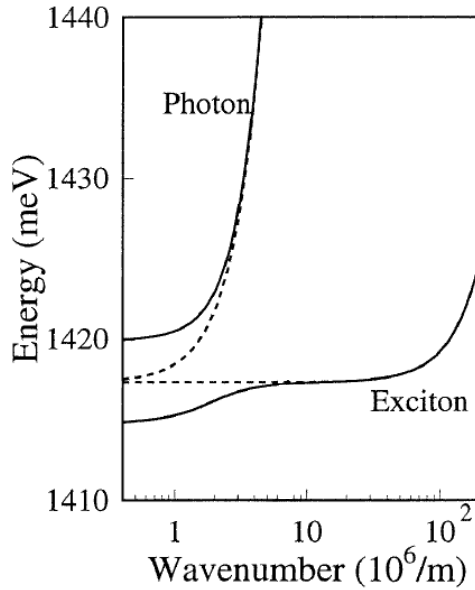


Figure 2.4: A typical polariton dispersion curve (solid lines) and the dispersion of the uncoupled photon and exciton modes (dashed lines). (Taken from [1])

indicate the dispersion of the bare photon and exciton modes. The two solid lines are conventionally labelled the upper and lower polariton branches and are due to symmetric and antisymmetric combinations of the bare exciton and photon modes. For values of the in-plane wavevector close to zero the dispersion is parabolic giving rise to the low effective mass of exciton-polaritons. At large in-plane wavevector the lower polariton branch shows mainly exciton-like characteristics while the upper polariton branch becomes photon-like.

### 2.2.1 Rabi splitting

The signature of the strong coupling regime is an anticrossing in the polariton dispersion. The energy separation of the two modes at the anticrossing point is known as the Rabi splitting. In the strong coupling regime the Rabi splitting is greater than the widths of both the bare exciton and the optical cavity mode. The case where the Rabi splitting is less than the widths of the two individual oscillators is known as the weak coupling regime where there is no splitting into distinct polariton

modes of the system. For a Fabry-Pérot structure with a cavity thickness  $d$ , an estimate of the Rabi splitting,  $\Omega$ , is given by [60]

$$\Omega = \sqrt{\frac{2\omega_0\omega_{\text{LT}}d}{L_{\text{DBR}} + d}} \quad (2.6)$$

where  $\omega_0$  is the frequency at the centre of the stop band for the Fabry-Pérot structure,  $\omega_{\text{LT}}$  is the exciton longitudinal-transverse splitting and  $L_{\text{DBR}}$ , the effective length of the Fabry-Pérot cavity is given by:  $L_{\text{DBR}} = n_A n_B \lambda_0 / 2(n_B - n_A)$  where  $n_{A,B}$  are the refractive indices of the layers in the Fabry-Pérot structure and  $\lambda_0$  is the wavelength at the centre of the stop band for the structure.

## 2.2.2 Exciton-polariton phenomena

The exciton - photon interaction for forming exciton-polaritons may be controlled in a number of ways. For example, planar microcavities can be grown in a wedge shape allowing for varying cavity mode wavelength across the structure; changing the temperature can also alter the cavity mode [61] and the application of external electric or magnetic fields may be used to tune the exciton mode [62]. This degree of control over the system leads to a wealth of fundamental physics associated with exciton-polaritons that, as well as being studied for its own sake, is setting the groundwork for novel devices. Reviews of work done on exciton-polaritons in semiconductor microcavities are given in [1] and [63]. In this section, some highlights of the work carried out in this field are discussed with an emphasis on their applications.

### Bose-Einstein condensates and polariton lasers

In 1996 Imamoğlu and Ram [64] proposed that because exciton-polaritons retain the bosonic nature of the exciton, they could form condensates and spontaneously emit coherent photons creating a polariton laser. Furthermore, it was proposed that, due to their very light effective mass, of the order  $10^{-5}m_e$ , exciton-polaritons would be able to form Bose-Einstein condensates at room temperature and above, unlike more traditional cold atom condensates. In 1998 polariton lasing was reported under optical pumping in planar microcavities at low temperature by Le Si Dang *et*

*al.* [21] and by 2007 at room temperature by Christopoulos *et al.* [22]. Polariton emission from similar electrically pumped devices has also been achieved [65] [66]. However, polariton lasing itself is insufficient to demonstrate Bose-Einstein condensation [63] and further works by Kasprzak *et al.* [19] and Balili *et al.* [67] subsequently showed that forming exciton-polariton condensates was possible. A great advantage of polariton lasers over conventional lasers is that they do not require a population inversion and so have a very low pumping threshold and hence require little power. For polariton lasing or to achieve Bose-Einstein condensation the exciton-polaritons must be ‘cooled’ to the ground state. One way in which this can be achieved is by interactions with phonons. However, contrary to the steep dispersion in the lower polariton branch in the planar case, phonons have a shallow dispersion which means many interactions with phonons of small momentum are required for polariton relaxation. Polaritons accumulate in the region of the spectrum where the character changes from exciton-like to photon-like, the point of inflection in the lower polariton branch as seen in Figure 2.4, causing a ‘bottleneck’ effect [68].

There is currently great interest in phenomena linked to the Bose-Einstein condensation of exciton-polaritons including superfluidity and superconductivity [20]. However, considering the Bose-Einstein condensation of exciton-polaritons is beyond the scope of the work presented in this chapter.

### **Optical integrated circuits**

Other exciton-polariton effects making use of spin and polarisation properties have been proposed for use in optical integrated circuits. ‘Spinoptronics’ is an emerging, multidisciplinary field designing and fabricating novel devices using the polariton pseudospin. The pseudospin is a vector used to represent and visualise the state of a two-level quantum system and is dependent on the spin of the exciton and the polarisation of the cavity photon [69]. For example, bistable optical switching requiring very low power was demonstrated experimentally by Baas *et al.* in 2004 [23] and polarisation-controlled optical logic gates were proposed and demonstrated in 2007 by Leyder *et al.* [25]. In 2008 several optical logic gates were integrated to form a circuit in a single microcavity [27]. Despite these extremely promising

advances, at the current time, optical integrated circuits using exciton-polaritons can in no way compete economically with more traditional electronic components.

## 2.3 Cylindrical and spherical microcavities

### 2.3.1 Whispering-gallery modes

Another way to confine photons, rather than using a Fabry-Pérot type cavity, is to take advantage of whispering-gallery modes found in cylindrical and spherical structures. Whispering-gallery modes are known to possess both high Q-factor and



Figure 2.5: The Whispering Gallery at St. Paul's Cathedral, London.

high finesse suggesting they would be suitable for producing polaritons. St Paul's Cathedral in London contains a renowned example of a whispering-gallery. Inside the dome a smooth cylinder stone wall causes the effect which gives the whispering-gallery its name. A person who whispers into the wall on one side of the dome can be clearly heard by a second person standing on the opposite side despite the diameter of the gallery being over 30 meters. The effect is due to the constructive interference of sound waves bouncing off the smooth stone walls. The same effect can be obtained

with light in dielectric microcavities of cylindrical or spherical geometry. Any mode where an integer number of wavelengths fits into the circumference is amplified by constructive interference and confined to the cavity by total internal reflection.

### 2.3.2 Exciton-polaritons in cylindrical and spherical cavities

Cylindrical and spherical microcavities are promising structures for exciton-polariton devices as they have distinct advantages over the more traditional planar cavities. Cylinders and spheres provide localisation of photons in two and three dimensions and, as introduced in the previous section, the whispering-gallery modes in such structures are particularly well confined. Non planar microcavities also do not suffer from the bottleneck effect caused by the momentum condition on polariton-phonon scattering in the planar case. Relieving the bottleneck effect allows for more efficient relaxation of exciton-polaritons to the ground state as required for polariton lasing and Bose-Einstein condensation.

Over the past few decades there has been increasing interest in exciton-polaritons in cylindrical and spherical microcavities due to the advancing technologies which have made their fabrication possible. In 1999 Panzarini and Andreani [29] predicted, using a quantum formalism, the strong coupling between exciton and photon modes with angular momentum quantum number,  $l$  equal to unity in AlAs/GaAs cylindrical stacked Bragg reflector structures containing a quantum well. Kaliteevski *et al.* [70] made a study of whispering-gallery modes for forming exciton-polaritons in cylindrical cavities of GaAs in 2007. They investigated the conditions required for strong coupling, looking for modes with a long lifetime and high finesse that are best suited for strong coupling. It was found that the first modes (radial quantum number,  $N$  equal to zero) for each azimuthal quantum number had the highest finesse and modes with low azimuthal quantum number had the longest lifetimes. In 2008 Bajoni *et al.* [28] demonstrated polariton lasing in a single GaAs/GaAlAs micropillar cavity. They found that the micropillar cavity allowed for a more well-defined, discrete energy spectrum than in planar cavities.

In 2001 Kaliteevski *et al.* [71] presented a theoretical study of semiconductor quantum dots in spherical Bragg reflector structures and the conditions for the weak

to strong coupling threshold were found for photon modes with quantum number  $l$  which characterises the relevant spherical harmonic equal to unity. In 2004 Bi-genwald *et al.* [72] studied cadmium telluride (CdTe) spheres as candidates for polariton lasers at low temperatures. The spheres that were studied in [72] were supermicron in size and of low finesse leading to exciton coupling with a number of photon modes simultaneously and a resultant complicated polariton spectrum with no ground state suitable for Bose-Einstein condensation. Studies of the weak coupling of excitons with photon modes in spherical quantum dots have been presented by Ajik *et al.* [73] [74]. Nikolaev, Smith and Ivanov [75] have investigated the weak to strong coupling threshold in semiconductor spheres with radii of the order of the wavelength of the photon modes, however this study was restricted to modes with quantum number  $l = 1$ .

Advances in crystal growth technology over the past two decades have made the fabrication of layered dielectric systems, such as the Fabry-Pérot etalon, possible. Nevertheless, the structures must be of high quality for use in experiments and the growth of multilayered structures is easier with some materials, for example CdTe, than it is with others [63]. Further advances in growth technology will undoubtedly allow for better planar cavities for experiments and devices as well as multilayer structures in other geometries. However, here we propose a much simpler system, the sub-micron sphere, for supporting exciton-polaritons.

The work presented in this thesis provides a systematic study of the lifetimes of the cavity modes in GaAs, GaN and ZnO spheres as a function of their quantum number and the radius of the sphere which ultimately allows for the prediction of reliable criteria for the weak - strong coupling threshold. The cavities under consideration are spheres of a material with given refractive index surrounded by vacuum. The radii of the cavities are sub-micron ensuring suitably high finesse.

## 2.4 Electromagnetic waves in spherical cavities

Maxwell's equations are given by Equations 1.2 – 1.5. In spherical polar coordinates there are three component equations for the electric,  $E$ -field and three for the mag-

netic,  $B$ -field. Assuming a time dependence of the form  $\exp(-i\omega t)$  the six equations take the form:

$$\begin{aligned}
\frac{1}{r \sin \theta} \left[ \frac{\partial}{\partial \theta} (\sin \theta E_\phi) - \frac{\partial E_\theta}{\partial \phi} \right] &= i\omega B_r \\
\frac{1}{r \sin \theta} \frac{\partial E_r}{\partial \phi} - \frac{1}{r} \frac{\partial}{\partial r} (r E_\phi) &= i\omega B_\theta \\
\frac{1}{r} \left[ \frac{\partial}{\partial r} (r E_\theta) - \frac{\partial E_r}{\partial \theta} \right] &= i\omega B_\phi \\
\frac{1}{r \sin \theta} \left[ \frac{\partial}{\partial \theta} (\sin \theta B_\phi) - \frac{\partial B_\theta}{\partial \phi} \right] &= -i \frac{\omega}{c^2} E_r \\
\frac{1}{r \sin \theta} \frac{\partial B_r}{\partial \phi} - \frac{1}{r} \frac{\partial}{\partial r} (r B_\phi) &= -i \frac{\omega}{c^2} E_\theta \\
\frac{1}{r} \left[ \frac{\partial}{\partial r} (r B_\theta) - \frac{\partial B_r}{\partial \theta} \right] &= -i \frac{\omega}{c^2} E_\phi
\end{aligned} \tag{2.7}$$

where  $c^{-2} = \mu_0 \varepsilon_0$ . Spherical waves may be split into two distinct polarisations, conventionally labelled TE and TM. For the TE-polarisation there is no radial component to the electric field ( $E_r = 0$ ) and hence the TE-polarised field can be completely described by five equations each containing at least two of the components  $B_r$ ,  $B_\theta$ ,  $B_\phi$ ,  $E_\theta$  and  $E_\phi$ . Similarly the TM-polarisation is completely described by five equations each containing at least two of the components  $E_r$ ,  $E_\theta$ ,  $E_\phi$ ,  $B_\theta$  and  $B_\phi$ .

From Maxwell's equations the vector Helmholtz equation may be derived giving:

$$\nabla^2 \Psi + \mathbf{k}^2 \Psi = 0 \tag{2.8}$$

where  $\Psi = \mathbf{E}$  or  $\mathbf{B}$ . Using the identity

$$\nabla^2 (\mathbf{r} \cdot \Psi) = \mathbf{r} \cdot (\nabla^2 \Psi) + 2 \nabla \cdot \Psi \tag{2.9}$$

it can be shown that the scalar quantity  $(\mathbf{r} \cdot \mathbf{E})$  where  $\mathbf{r} = r \hat{\mathbf{r}}$  and  $\hat{\mathbf{r}}$  is the radial unit vector satisfies the Helmholtz equation. Using  $\nabla \cdot \mathbf{E} = 0$  we obtain:

$$\nabla^2 (\mathbf{r} \cdot \mathbf{E}) + k^2 (\mathbf{r} \cdot \mathbf{E}) = \mathbf{r} \cdot [\nabla^2 \mathbf{E} + k^2 \mathbf{E}] = 0 \tag{2.10}$$

The quantity  $(\mathbf{r} \cdot \mathbf{E})$  can also be written as  $r E_r$ , hence we can write a scalar Helmholtz equation for the radial components of the field. For the TM-polarisation (where  $B_r = 0$ ) the equation is

$$\nabla^2 (r E_r) + k^2 r E_r = 0 \tag{2.11}$$

In spherical polars the scalar Helmholtz equation is

$$\frac{1}{r^2 \sin \theta} \left[ \sin \theta \frac{\partial}{\partial r} \left( r^2 \frac{\partial \psi}{\partial r} \right) + \frac{\partial}{\partial \theta} \left( \sin \theta \frac{\partial \psi}{\partial \theta} \right) + \frac{1}{\sin \theta} \frac{\partial^2 \psi}{\partial \phi^2} \right] + k^2 \psi = 0 \quad (2.12)$$

where  $\psi = rE_r$ .

Using the technique of separation of variables, two quantum numbers are introduced:  $l$ , the orbital angular momentum number can take positive integer values and the projection of the orbital angular momentum number,  $m$ , takes integer values from  $-l$  to  $l$ . This gives the components of the TM-polarised field as:

$$B_r = 0 \quad (2.13)$$

$$B_\theta = \frac{\omega}{c^2} \frac{m}{\sin \theta} z_l(kr) P_l^{|m|}(\cos \theta) \exp(im\phi) \quad (2.14)$$

$$B_\phi = i \frac{\omega}{c^2} z_l(kr) \frac{d}{d\theta} \left[ P_l^{|m|}(\cos \theta) \right] \exp(im\phi) \quad (2.15)$$

$$E_r = \frac{l(l+1)}{r} z_l(kr) P_l^{|m|}(\cos \theta) \exp(im\phi) \quad (2.16)$$

$$E_\theta = \frac{1}{r} \frac{d}{dr} (r z_l(kr)) \frac{d}{d\theta} \left[ P_l^{|m|}(\cos \theta) \right] \exp(im\phi) \quad (2.17)$$

$$E_\phi = \frac{im}{\sin \theta} \frac{1}{r} \frac{d}{dr} (r z_l(kr)) P_l^{|m|}(\cos \theta) \exp(im\phi) \quad (2.18)$$

where  $P_l^{|m|}(\cos \theta)$  is an associated Legendre function and  $z_l(kr)$  is some combination of the spherical Hankel functions  $h_l^{(1)}(kr)$  and  $h_l^{(2)}(kr)$  with  $k = \omega/c$ . Similarly for the TE-polarised field we have:

$$E_r = 0 \quad (2.19)$$

$$E_\theta = -\frac{\omega m}{\sin \theta} z_l(kr) P_l^{|m|}(\cos \theta) \exp(im\phi) \quad (2.20)$$

$$E_\phi = -i\omega z_l(kr) \frac{d}{d\theta} \left[ P_l^{|m|}(\cos \theta) \right] \exp(im\phi) \quad (2.21)$$

$$B_r = \frac{l(l+1)}{r} z_l(kr) P_l^{|m|}(\cos \theta) \exp(im\phi) \quad (2.22)$$

$$B_\theta = \frac{1}{r} \frac{d}{dr} (r z_l(kr)) \frac{d}{d\theta} \left[ P_l^{|m|}(\cos \theta) \right] \exp(im\phi) \quad (2.23)$$

$$B_\phi = \frac{im}{\sin \theta} \frac{1}{r} \frac{d}{dr} (r z_l(kr)) P_l^{|m|}(\cos \theta) \exp(im\phi) \quad (2.24)$$

It should be noted that no field exists for the case  $l = 0$ . The associated Legendre polynomial,  $P_l^{|m|}$  for  $l = 0$ ,  $m = 0$  is  $P_0^0(\cos \theta) = 1$ , and its derivative is zero. Substitution of these results into Equations 2.13 – 2.18 and 2.19 – 2.24 gives zero for all field components.

### 2.4.1 Eigenfrequencies of the spherical cavity

The electromagnetic fields inside and outside a dielectric sphere can be constructed from the field solutions for a uniform dielectric medium. Consider waves with the TE-polarisation, radiating from a sphere of radius  $\rho$  and refractive index  $n_1$ , into a medium of refractive index  $n_2$ . Outside the sphere the waves only propagate outwards, hence the radial component,  $z_l(k_2r)$  is given by a spherical Hankel function of the first kind:  $h_l^{(1)}(k_2r) = j_l(k_2r) + in_l(k_2r)$  where we have introduced the notation  $k_i = n_i\omega/c$ . The components of the spherical Hankel function, the spherical Bessel function,  $j_l(kr)$ , and the spherical Neumann function,  $n_l(kr)$ , are shown in Figure 2.6. Inside the sphere there are both outgoing and incoming waves (due to reflection at the boundary) hence the radial part is given by a sum of spherical Hankel functions of the first and second kind. Also, the field at the origin must be finite so the two spherical Hankel functions must be added in equal parts:

$$z_l(kr) = \frac{1}{2}h_l^{(1)}(k_1r) + \frac{1}{2}h_l^{(2)}(k_1r) = j_l(k_1r). \quad (2.25)$$

Therefore, inside the sphere, the electric field is given by:

$$\mathbf{E}^{(in)} = A_{lm}\omega \left[ \frac{m}{\sin\theta} P_l^{|m|}(\cos\theta) \hat{\boldsymbol{\theta}} + i \frac{d}{d\theta} \left( P_l^{|m|}(\cos\theta) \right) \hat{\boldsymbol{\phi}} \right] j_l(k_1r) \exp(im\phi) \quad (2.26)$$

and outside the sphere by:

$$\mathbf{E}^{(out)} = B_{lm}\omega \left[ \frac{m}{\sin\theta} P_l^{|m|}(\cos\theta) \hat{\boldsymbol{\theta}} + i \frac{d}{d\theta} \left( P_l^{|m|}(\cos\theta) \right) \hat{\boldsymbol{\phi}} \right] h_l^{(1)}(k_2r) \exp(im\phi) \quad (2.27)$$

where  $A_{lm}$  and  $B_{lm}$  are constants depending on the quantum numbers  $l$  and  $m$  and  $\hat{\boldsymbol{\theta}}$  and  $\hat{\boldsymbol{\phi}}$  are unit vectors in the  $\theta$  and  $\phi$  directions. The corresponding magnetic field components, calculated using Equation set 2.7 are:

$$\mathbf{B}^{(in)} = A_{lm} \left[ \frac{l(l+1)}{r} j_l(k_1r) P_l^{|m|}(\cos\theta) \hat{\mathbf{r}} + \left( \frac{d}{d\theta} P_l^{|m|}(\cos\theta) \hat{\boldsymbol{\theta}} + \frac{im}{\sin\theta} P_l^{|m|}(\cos\theta) \hat{\boldsymbol{\phi}} \right) \frac{1}{r} \frac{d}{dr} (r j_l(k_1r)) \right] \exp(im\phi) \quad (2.28)$$

$$\mathbf{B}^{(out)} = B_{lm} \left[ \frac{l(l+1)}{r} h_l^{(1)}(k_2r) P_l^{|m|}(\cos\theta) \hat{\mathbf{r}} + \left( \frac{d}{d\theta} P_l^{|m|}(\cos\theta) \hat{\boldsymbol{\theta}} + \frac{im}{\sin\theta} P_l^{|m|}(\cos\theta) \hat{\boldsymbol{\phi}} \right) \frac{1}{r} \frac{d}{dr} (r h_l^{(1)}(k_2r)) \right] \exp(im\phi) \quad (2.29)$$

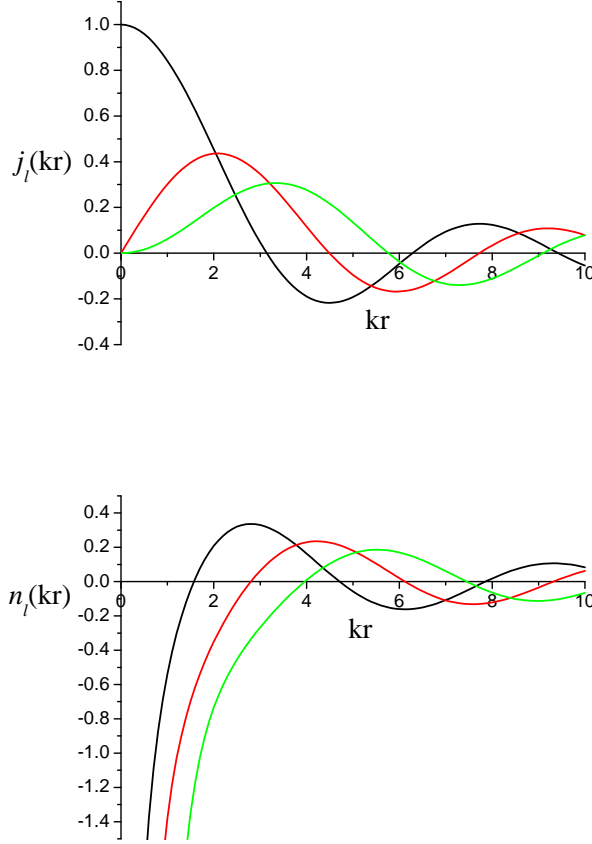


Figure 2.6: Spherical Bessel functions of the first kind  $j_l(kr)$  (top) and spherical Neumann functions,  $n_l(kr)$  (bottom), for  $l = 0, 1, 2$  shown in black, red and green respectively.

where  $\hat{\mathbf{r}}$  is also a unit vector, in the  $r$ -direction. The tangential components of the fields inside and outside the sphere must be continuous across the boundary at  $r = \rho$ . For the electric field components we have

$$B_{lm}j_l(k_1\rho) = A_{lm}h_l^{(1)}(k_2\rho). \quad (2.30)$$

The magnetic field components give the relation

$$B_{lm} [j_l(k_1\rho) + \rho k_1 j_l'(k_1\rho)] = A_{lm} [h_l^{(1)}(k_2\rho) + \rho k_2 h_l^{(1)'}(k_2\rho)]. \quad (2.31)$$

Eliminating  $A_{lm}/B_{lm}$  from Equations 2.30 and 2.31 gives

$$j_l(k_1\rho) [h_l^{(1)}(k_2\rho) + \rho k_2 h_l^{(1)'}(k_2\rho)] - h_l^{(1)}(k_2\rho) [j_l(k_1\rho) + \rho k_1 j_l'(k_1\rho)] = 0 \quad (2.32)$$

noting that  $d/dr(rh_l^{(1)}(kr)) = h_l^{(1)}(kr) + krh_l^{(1)'}(kr)$ .

Similarly, for the TM-polarisation the fields inside and outside the sphere are given by:

$$\begin{aligned} \mathbf{E}^{(\text{in})} = & C_{lm} \left[ \frac{l(l+1)}{r} j_l(k_1 r) P_l^{|m|}(\cos \theta) \hat{\mathbf{r}} + \right. \\ & \left. \left( \frac{d}{d\theta} P_l^{|m|}(\cos \theta) \hat{\boldsymbol{\theta}} + \frac{im}{\sin \theta} P_l^{|m|}(\cos \theta) \hat{\boldsymbol{\phi}} \right) \frac{1}{r} \frac{d}{dr} (r j_l(kr)) \right] \exp(im\phi) \end{aligned} \quad (2.33)$$

$$\begin{aligned} \mathbf{E}^{(\text{out})} = & D_{lm} \left[ \frac{l(l+1)}{r} h_l^{(1)}(k_2 r) P_l^{|m|}(\cos \theta) \hat{\mathbf{r}} + \right. \\ & \left. \left( \frac{d}{d\theta} P_l^{|m|}(\cos \theta) \hat{\boldsymbol{\theta}} + \frac{im}{\sin \theta} P_l^{|m|}(\cos \theta) \hat{\boldsymbol{\phi}} \right) \frac{1}{r} \frac{d}{dr} (r h_l^{(1)}(k_2 r)) \right] \exp(im\phi) \end{aligned} \quad (2.34)$$

$$\mathbf{B}^{(\text{in})} = C_{lm} \frac{\omega}{c^2} \left[ \frac{m}{\sin \theta} P_l^{|m|}(\cos \theta) \hat{\boldsymbol{\theta}} + i \frac{d}{d\theta} \left( P_l^{|m|}(\cos \theta) \right) \hat{\boldsymbol{\phi}} \right] j_l(k_1 r) \exp(im\phi) \quad (2.35)$$

$$\mathbf{B}^{(\text{out})} = D_{lm} \frac{\omega}{c^2} \left[ \frac{m}{\sin \theta} P_l^{|m|}(\cos \theta) \hat{\boldsymbol{\theta}} + i \frac{d}{d\theta} \left( P_l^{|m|}(\cos \theta) \right) \hat{\boldsymbol{\phi}} \right] h_l^{(1)}(k_2 r) \exp(im\phi). \quad (2.36)$$

Again the tangential field components must be continuous across the boundary at  $r = \rho$  which gives two equations:

$$C_{lm} [j_l(k_1 \rho) + \rho k_1 j_l'(k_1 \rho)] = D_{lm} [h_l^{(1)}(k_2 \rho) + \rho k_2 h_l^{(1)'}(k_2 \rho)] \quad (2.37)$$

$$C_{lm} j_l(k_1 \rho) = D_{lm} h_l^{(1)}(k_2 \rho) \quad (2.38)$$

and eliminating  $C_{lm}/D_{lm}$  from Equations 2.37 and 2.38 gives

$$\varepsilon_1 j_l(k_1 \rho) [h_l^{(1)}(k_2 \rho) + k_2 \rho h_l^{(1)'}(k_2 \rho)] - \varepsilon_2 h_l^{(1)}(k_2 \rho) [j_l(k_1 \rho) + k_1 \rho j_l'(k_1 \rho)] = 0. \quad (2.39)$$

Solving Equations 2.32 and 2.39 gives the generally complex eigenfrequencies of the spherical cavity. The electric or magnetic fields inside and outside a sphere may be calculated by matching field components across the boundary and choosing appropriate coefficients for  $A_{lm}$ ,  $B_{lm}$ ,  $C_{lm}$  and  $D_{lm}$ .

## 2.4.2 Reflection from the spherical boundary

The eigenvalue Equations 2.32 and 2.39 may also be derived from consideration of the amplitude of the wave being reflected from the spherical interface. Recall that the interface marks the boundary between materials of refractive index  $n_1$  and  $n_2$  at

radius  $\rho$ . Consider a spherical wave originating inside the cavity, propagating until it reaches the boundary and then being partially reflected. The amplitude of the reflected wave must be equal to the product of the outgoing wave and the amplitude reflection coefficient of the cavity,  $R_{\text{TE(TM)}}$  (where we define  $R_{\text{TE}}$  as the ratio of the tangential components of the electric field for ingoing and outgoing waves and  $R_{\text{TM}}$  as the ratio of the tangential components of the magnetic field.) The outgoing and incoming waves inside the sphere are described by spherical Hankel functions of the first and second kind respectively. As in Section 2.4.1, these Hankel functions must be of equal magnitude to avoid a divergence at the centre of the sphere. It follows that the equation for the TE(TM) modes of the sphere may be written in the form:

$$h_l^{(2)}(k_1\rho) = R_{\text{TE(TM)}}h_l^{(1)}(k_1\rho). \quad (2.40)$$

The amplitude reflection coefficient is a function of the sphere radius and the quantum number  $l$  and can be found, for example, in [4]:

$$R_{\text{TE}} = \frac{D_{l2}^{(1)} - D_{l1}^{(1)}}{D_{l1}^{(2)} - D_{l2}^{(1)}} \quad (2.41)$$

$$R_{\text{TM}} = \frac{-(1/\varepsilon_1)D_{l1}^{(1)} + (1/\varepsilon_2)D_{l2}^{(1)}}{(1/\varepsilon_2)D_{l2}^{(1)} + (1/\varepsilon_1)D_{l1}^{(2)}} \quad (2.42)$$

where

$$D_l^{(1,2)} = \frac{-1}{k_0\rho} \frac{\partial/\partial r \left( r h_l^{(1,2)}(k\rho) \right)}{h_l^{(1,2)}(k\rho)}$$

and  $\varepsilon_{1,2} = n_{1,2}^2$ . Substitution of Equation 2.41 into Equation 2.40 gives the same result as Equation 2.32. Similarly, substitution of Equation 2.42 into Equation 2.40 gives Equation 2.39. Figure 2.7 shows how the power reflection coefficient,  $|R_{\text{TE,TM}}|^2$ , varies with increasing sphere radius for a GaAs sphere (refractive index  $n = 3.7$ ) in vacuum. For the TE-polarisation the power reflection coefficient is close to unity at small radii and decreases asymptotically to the equivalent value for a planar system at large radius. For the TM-polarisation the power reflection coefficient is also close to unity at small radii, then there is a dip in the spectrum that can be associated with a Brewster angle type effect before tending to the corresponding planar system value from below.

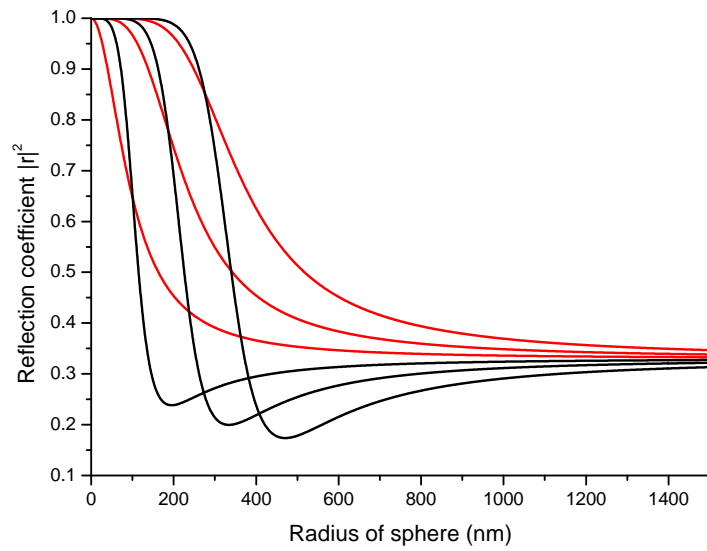


Figure 2.7: Dependence of the power reflection coefficient on the radius of a GaAs sphere (refractive index  $n = 3.7$ ) in vacuum at a frequency corresponding to the exciton resonance,  $\hbar\omega = 1.515$  eV. The red lines show TE modes with  $l = 1, 2$  and  $3$  from left to right while the black lines show TM modes, again with  $l = 1, 2$  and  $3$  from left to right.

## 2.5 Mode decay in spherical cavities

In order to find numerical solutions to the eigenfrequency equations it is helpful to first find an approximate solution as an initial guess for iterative computational routines.

Consider a sphere of large radius, such that the waves arriving at the boundary can be considered as plane waves and the approximations to the spherical Hankel functions of large argument may be used:

$$h_l^{(1,2)}(kr) \rightarrow -\frac{i}{kr} \exp\left(\pm i \left[ kr - \frac{\pi l}{2} \right]\right) \quad (2.43)$$

Equation 2.40 becomes

$$R_{\text{TE(TM)}} \exp\left[i \left( k_1 \rho - \frac{\pi l}{2} \right)\right] = \exp\left[-i \left( k_1 \rho - \frac{\pi l}{2} \right)\right] \quad (2.44)$$

which can be used to give a simplified expression for the real part of the eigenmode frequency by taking the argument:

$$\arg(R_{\text{TE(TM}}) + \arg\left(\exp\left[2i \left( k_1 \rho - \frac{\pi l}{2} \right)\right]\right) = 2\pi N \quad (2.45)$$

where  $N$  is an integer or zero. For the TE-polarisation we calculate using Equation 2.41 that  $\arg(R_{\text{TE}}) \approx 0$ . Using  $k_1 = n_1 \omega / c$  and rearranging we obtain an approximation to the eigenfrequency:

$$\begin{aligned} \frac{n_1 \omega^{(\text{TE})} \rho}{c} &\approx \pi \left[ N + \frac{l}{2} \right] \\ \omega^{(\text{TE})} &\approx \frac{\pi c}{n_1 \rho} \frac{1}{2} (2N + l). \end{aligned} \quad (2.46)$$

Conversely, for the TM-polarisation we calculate using Equation 2.42 that  $\arg(R_{\text{TM}}) \approx \pi$  and Equation 2.45 becomes

$$\begin{aligned} \frac{n_1 \omega^{(\text{TM})} \rho}{c} &\approx \frac{\pi}{2} (2N + 1) + \frac{\pi l}{2} \\ \omega^{(\text{TM})} &\approx \frac{\pi c}{n_1 \rho} \frac{1}{2} (2N + l + 1). \end{aligned} \quad (2.47)$$

There is a minimum sphere radius below which a mode of quantum number  $l$  cannot be supported at a given frequency. This minimum radius,  $\rho_0$  may be

estimated by setting  $N = 0$  in Equations 2.46 and 2.47. These rearrange to give, for the TE-polarisation

$$\rho_0^{(\text{TE})} \approx \frac{\pi c l}{2n_1 \omega^{(\text{TE})}} \quad (2.48)$$

and for the TM-polarisation

$$\rho_0^{(\text{TM})} \approx \frac{\pi c}{2n_1 \omega^{(\text{TM})}} (l + 1). \quad (2.49)$$

Figure 2.8 shows the dependences of the minimum radius on the given quantum

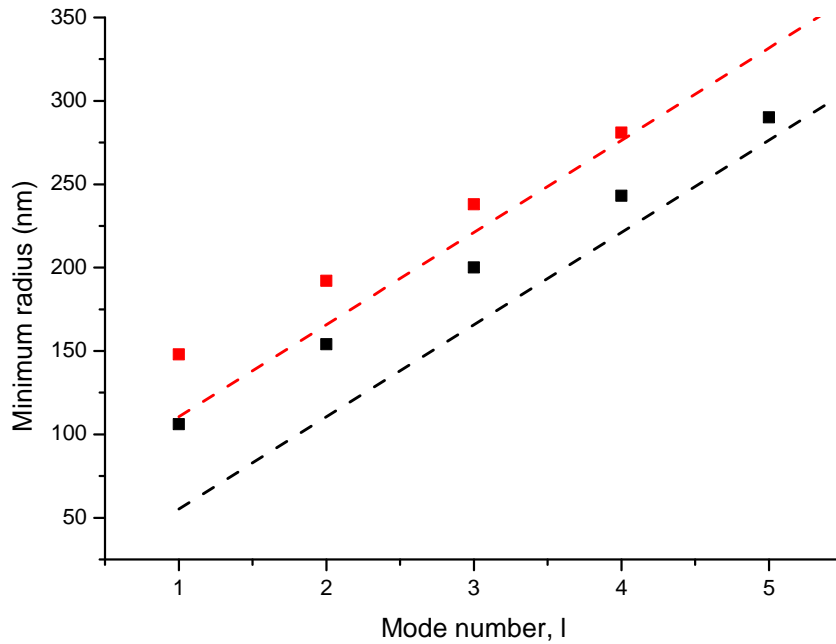


Figure 2.8: The minimum sphere radius below which a mode of quantum number  $l$  cannot be supported at a frequency of  $\hbar\omega = 1.515$  eV. The dashed lines give the predictions of Equations 2.48 and 2.49 for a GaAs sphere (refractive index  $n = 3.7$ ) in vacuum. The solid symbols give the actual radius of appearance of modes. The TE-polarisation is shown in black and the TM-polarisation in red.

number,  $l$ . The calculations were carried out for a GaAs sphere (refractive index  $n = 3.7$ ) in vacuum (refractive index  $n = 1.0$ ) and modes with eigenfrequency at the corresponding exciton resonance,  $\hbar\omega = 1.515$  eV. The dashed lines show the prediction of the approximate formulae in Equations 2.48 and 2.49 while the solid

symbols give the minimum sphere radii for the support of modes found using an iterative computer code. It can be seen for both polarisations that the necessary minimum radius increases with increasing angular momentum quantum number,  $l$ . It is apparent that the values given by Equations 2.48 and 2.49 are not good approximations. This is because the frequency under consideration,  $\hbar\omega = 1.515$  eV, corresponds to a wavelength of around 220 nm in GaAs. This is comparable to the size of the sphere, contrary to the initial assumptions of the approximation. Better approximations were obtained by a colleague, I.Iorsh [76]: if the refractive index of the sphere is greater than that of the surrounding medium, as it is for all spheres considered here, then the electric field should have an antinode at the boundary of the sphere. For the TE-polarisation the form of the electric field given in Equations 2.19–2.21 shows that  $j_l(k_1\rho)$  should have a maximum at the sphere boundary, hence its derivative should have a root. According to a theorem of Siegel [77] the first root of  $j'_l(x)$  lies between the values  $\sqrt{(l+1/2)(l+5/2)}$  and  $\sqrt{2(l+1/2)(l+3/2)}$ . So, for  $N = 0$ , taking an average between these bounds as the approximation, we have that the argument of the Bessel function at the boundary is given by

$$\frac{n_1\omega^{(TE)}\tilde{\rho}_0^{(TE)}}{c} \approx \frac{1}{2} \left( \sqrt{(l+1/2)(l+5/2)} + \sqrt{2(l+1/2)(l+3/2)} \right) \quad (2.50)$$

where  $\tilde{\rho}_0$  is the new approximation to the minimum radius. This has an approximately linear variation with  $l$  which can be fitted numerically to the function  $1.3l + 1.3$ . Hence, a better approximation for the minimum radius at which a TE-polarised mode with quantum number  $l$  can be supported is given by

$$\tilde{\rho}_0^{(TE)} \approx \frac{1.3c(l+1)}{n_1\omega^{(TE)}}. \quad (2.51)$$

A similar analysis for the TM mode gives

$$\tilde{\rho}_0^{(TM)} \approx \frac{1.3c(l+2)}{n_1\omega^{(TM)}}. \quad (2.52)$$

Figure 2.9 shows a cross section of the electric field intensity,  $|E|^2$  for the TE modes of a GaAs sphere in vacuum. The plots show the variation of the fields with  $\theta$  at  $\phi = 0$ . For each value of  $l$  ( $l = 1, 2, 3$ ), the radius of the sphere is the minimum sphere radius,  $\rho_0$ , calculated using the iterative computer code. The black lines

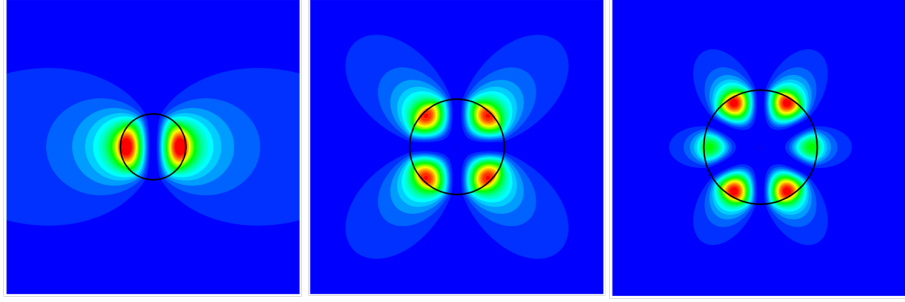


Figure 2.9: Three TE modes with increasing quantum number  $l = 1, 2$  and  $3$  and  $m = 0$ . The radius of the sphere, marked in black, increases from left to right as  $l$  increases as a bigger sphere is needed to support the mode. Blue represents areas of low field intensity while red shows areas of high field intensity.

mark the radii of the spheres. It can be seen for each of the values of  $l$  that there is some leakage of the field into the surrounding vacuum. However the greater the value of  $l$ , the greater the confinement of the mode to the sphere.

We now consider the complex form of the eigenfrequencies,  $\omega - i\gamma$ , that result from solving Equation 2.40 by using the spherical Hankel function approximations of Equation 2.43:

$$\begin{aligned} \frac{1}{R_{\text{TE(TM)}}} &= \exp \left[ 2i \left( \frac{n_1(\omega - i\gamma)\rho}{c} - \frac{\pi l}{2} \right) \right] \\ \frac{1}{R_{\text{TE(TM)}}} &= \exp \left[ i \left( \frac{2n_1\omega\rho}{c} - \pi l \right) \right] \exp \left[ \frac{2n_1\gamma\rho}{c} \right]. \end{aligned} \quad (2.53)$$

After taking the magnitude of both sides we can rearrange to obtain an approximate expression for the decay constant,  $\gamma$ , given by the imaginary part of the eigenfrequency:

$$\begin{aligned} \frac{1}{|R_{\text{TE(TM)}}|} &= \exp \left[ \frac{2n_1\gamma_{\text{TE(TM)}}\rho}{c} \right] \\ \gamma_{\text{TE(TM)}} &= \frac{c}{2n_1\rho} \ln \left| \frac{1}{R_{\text{TE(TM)}}} \right|. \end{aligned} \quad (2.54)$$

The decay constant is the inverse of the lifetime of the photon mode so, for a mode with a long lifetime, a small decay constant is required. These very approximate values were used as an initial guess for an iterative computer program to find the roots of Equations 2.32 and 2.39. The dashed lines in Figure 2.5 show the approx-

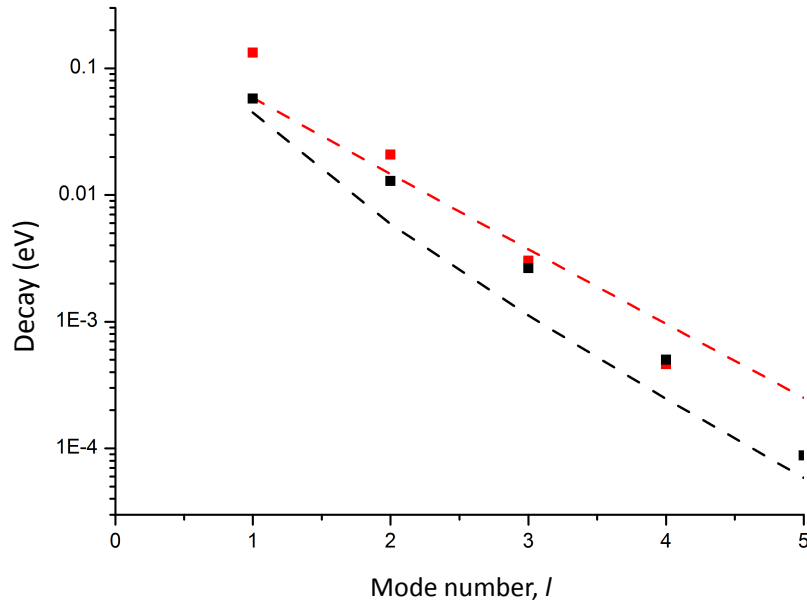


Figure 2.10: The decay constant,  $\gamma$  for modes with different  $l$  in a GaAs sphere in vacuum. The dashed lines represent the approximation given by Equation 2.54 while the symbols show the actual values given by the iterative computer program. The TE-polarisation is shown in black and the TM-polarisation in red.

imate values of the decay constant,  $\gamma$  in electron volts, for different values of  $l$ , for cavity modes in a GaAs sphere. The TE-polarisation is shown in black and the TM-polarisation in red. The decay constant exhibits a nearly exponential decrease with increasing  $l$ . The solid symbols show the values given by the root-finding computer program: black squares for the TE-polarisation and red for the TM-polarisation.

### 2.5.1 Estimate of the polariton splitting

An analytical estimate of the polariton splitting can be obtained by considering the effect that the excitonic contribution to the dielectric constant has on an optical mode that would be at frequency  $\omega_{\text{ex}}$  in the absence of excitonic effects. We know from Equations 2.48 and 2.49 that the minimum radius of sphere required to support

a mode at frequency  $\omega_{\text{ex}}$  can be written as

$$\varepsilon_b \rho_0^2 \omega_{\text{ex}}^2 = f(l) \quad (2.55)$$

where  $f(l)$  is the appropriate function of  $l$  for either the TE or TM-polarisation. Including the excitonic contribution using Equation 2.2 and neglecting any non radiative exciton decay gives

$$\varepsilon_b \left( 1 + \frac{\omega_{LT}}{\omega_{\text{ex}} - \omega} \right) \rho_0^2 \omega^2 = f(l). \quad (2.56)$$

Combining Equations 2.55 and 2.56 and rearranging yields:

$$\begin{aligned} (\omega_{\text{ex}} - \omega)(\omega_{\text{ex}} + \omega) - \frac{\omega^2 \omega_{LT}}{\omega_{\text{ex}} - \omega} &= 0 \\ (\omega - \omega_{\text{ex}})(\omega + \omega_{\text{ex}}) - \frac{\omega^2 \omega_{LT}}{\omega - \omega_{\text{ex}}} &= 0. \end{aligned} \quad (2.57)$$

Assuming that the frequency in Equation 2.56 is close to the exciton resonance frequency,  $(\omega - \omega_{\text{ex}}) \ll \omega_{\text{ex}} \rightarrow \omega \approx \omega_{\text{ex}}$ , we obtain:

$$(\omega - \omega_{\text{ex}})^2 \approx \frac{\omega_{\text{ex}} \omega_{LT}}{2} \quad (2.58)$$

which gives the splitting of the polariton modes as:

$$\begin{aligned} \Delta &= 2(\omega - \omega_{\text{ex}}) \\ \Delta &= \sqrt{2\omega_{\text{ex}} \omega_{LT}}. \end{aligned} \quad (2.59)$$

This result is not exclusive to the case of spherical symmetry but it is worth noting that the splitting for the sphere is generally larger than for planar microcavities with Bragg mirrors. This is because the electric field of the cavity mode is mostly localised inside the sphere and thus its overlap integral with the exciton wavefunction of the corresponding symmetry approaches unity. On the other hand, in planar cavities the overlap integral is strongly reduced due to the penetration of the cavity mode into the dielectric Bragg mirrors.

## 2.5.2 Optical mode analysis

Figures 2.11, 2.12 and 2.13 show the decay constant as a function of radius for spheres of GaAs, GaN and ZnO respectively. The spheres are all in vacuum with

the real part of their eigenfrequencies set to their respective exciton resonances ( $\hbar\omega_{\text{ex}} = 1.515$  eV in GaAs,  $\hbar\omega_{\text{ex}} = 3.502$  eV in GaN and  $\hbar\omega_{\text{ex}} = 3.386$  eV in ZnO). The horizontal lines in the figures represent the weak to strong coupling threshold as discussed in Section 2.6.1.

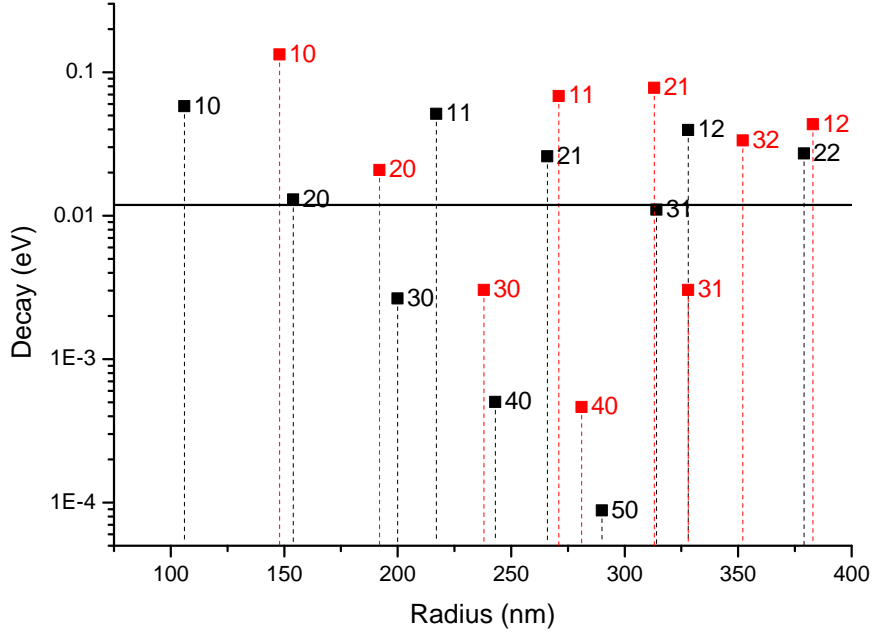


Figure 2.11: Decay constant as a function of radius for bare cavity modes in a GaAs sphere in vacuum. The real part of the frequency is equal to the exciton resonance frequency for excitons in GaAs,  $\hbar\omega_{\text{ex}} = 1.515$  eV. The TE(TM)-polarised modes are shown in black (red) and are labelled  $lN$ . The horizontal line indicates the estimated polariton splitting value calculated by Equation 2.59.

As apparent from the results for GaAs in Figure 2.11, the number of modes that can exist for a sphere of given radius increases as the radius increases. Above the minimum radius required to support a mode with given quantum number  $l$ , increasing the radius further makes possible modes with the same  $l$  value but increasing radial quantum number  $N$ . We label the modes  $lN$  such that the first mode with  $l = 1$  has the label 10 and the second mode with  $l = 2$  has the label 21.

As the computer program has to find the roots of an equation in the complex

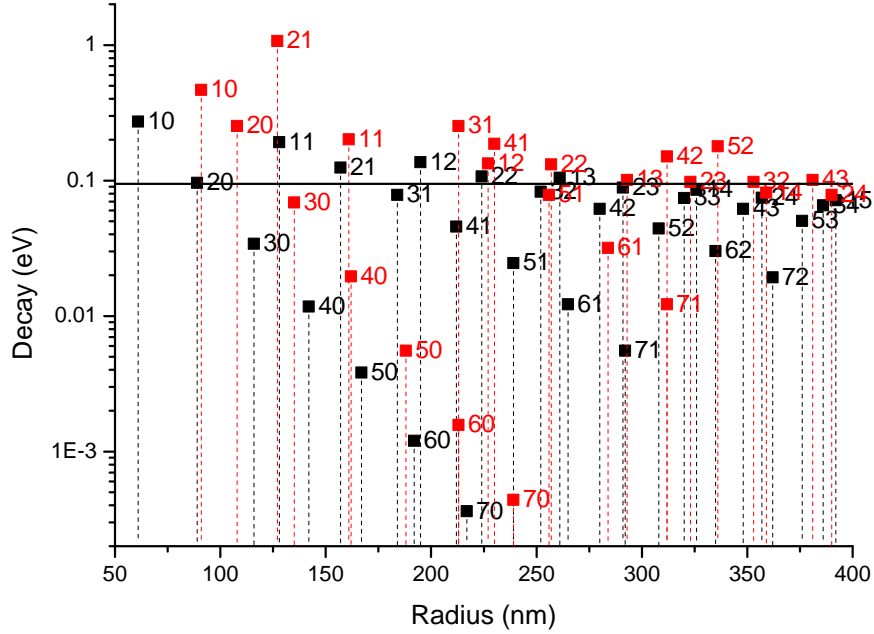


Figure 2.12: Decay constant as a function of radius for bare cavity modes in a GaN sphere in vacuum. The real part of the frequency is equal to the exciton resonance frequency for excitons in GaN,  $\hbar\omega_{\text{ex}} = 3.502$  eV. The TE(TM)-polarised modes are shown in black (red) and are labelled  $lN$ . The horizontal line indicates the estimated polariton splitting value calculated by Equation 2.59.

plane, the initial guess needs to be more and more accurate as  $l$  increases (in order for the calculation to converge.) The results that are displayed all satisfy Equations 2.32 for the TE-polarisation and 2.39 for the TM-polarisation to within a convergence tolerance of  $\pm 1 \times 10^{-5}$ .

Equation 2.54 states that the decay constant  $\gamma$  depends explicitly on the sphere radius  $\rho$  and also implicitly on it through the reflection coefficient  $R$  (as given in Equations 2.41 and 2.42). Consider increasing the sphere radius from an initial very small value: for a mode with specific  $l$ , the initial increase in radius and the corresponding rapid decrease in reflection coefficient shown in Figure 2.7 lead to an increase in  $\gamma$ . Further increase in radius causes the reflection coefficient to tend to a nearly constant value. At this point the radius itself has more bearing on the

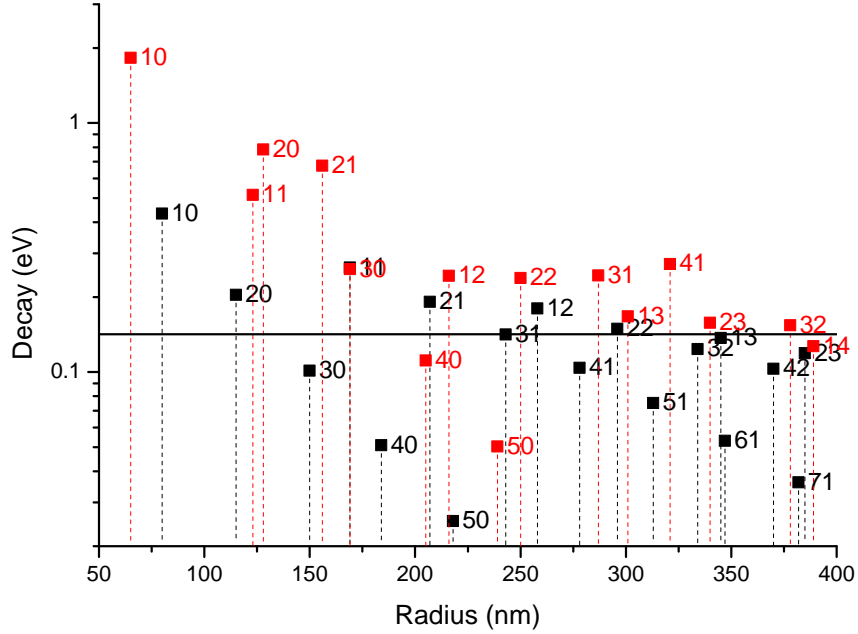


Figure 2.13: Decay constant as a function of radius for bare cavity modes in a ZnO sphere in vacuum. The real part of the frequency is equal to the exciton resonance frequency for excitons in ZnO,  $\hbar\omega_{\text{ex}} = 3.386$  eV. The TE(TM)-polarised modes are shown in black (red) and are labelled  $lN$ . The horizontal line indicates the estimated polariton splitting value calculated by Equation 2.59.

variation of  $\gamma$  than the reflection coefficient and, due to the inverse dependence of  $\gamma$  on  $\rho$ ,  $\gamma$  slowly decreases. To obtain the highest Q-factor whilst holding the cavity frequency at the exciton resonance, the decay constant must be as small as possible. To satisfy the requirement of a large Q-factor, necessary for the production of polaritons with a long lifetime, this suggests that a mode with large  $l$  would be most suitable. However, in the limit of large radius (required to increase  $l$ ) the density of modes becomes so large that even though the Q-factor is high, the finesse of the modes becomes too low to produce distinct polariton states. The mode with the highest Q-factor shown in Figure 2.11 is that labelled 50 in the TE-polarisation with a Q-factor of over 17,000. By comparison, the modes with the highest decay constants have Q-factors of around just 25.

## 2.6 Exciton-polariton calculations

The eigenfrequencies of the exciton-polariton modes of the spherical microcavity can be found from the same equations as for the bare cavity modes (Equations 2.32 and 2.39) by including the excitonic contribution to the refractive index using Equation 2.2. Numerical computations were carried out to find the complex eigenmodes using a Fortran program already available in Durham. The spheres under consideration are at least an order of magnitude larger than the exciton radius therefore a bulk model of the exciton and its dielectric response, given by Equation 2.2, is expected to be satisfactory. For GaAs, the effective Bohr radius of the exciton,  $a_B$ , is 15 nm and in GaN and ZnO  $a_B$  is 2 – 4 times smaller [60]. Table 2.1 gives the parameter values used in the calculations for the different semiconductor materials under consideration. Note that  $\omega_{LT}$  is an order of magnitude larger in GaN and ZnO than it

Semiconductor	$\varepsilon_b$	$\hbar\omega_{\text{ex}}(\text{eV})$	$\hbar\omega_{LT}$ (meV)	$\hbar\Gamma$ (meV)
GaAs at 4K [70]	13.69	1.515	0.08	1
GaN at 2K [78]	7.29	3.502	1.45	1
ZnO at 5K [79]	2.11	3.384	5	1

Table 2.1: Parameters used for calculating the excitonic contribution to the refractive index for different semiconductor materials.

is in GaAs as it is inversely proportional to the dielectric constant  $\varepsilon_b$ .

### 2.6.1 Results

The frequency of the exciton-polariton modes as a function of sphere radius are shown in Figures 2.14, 2.15 and 2.16 for GaAs, GaN and ZnO respectively. The real parts of the bare cavity optical eigenfrequencies and the exciton energy are shown in black for comparison. The approximations given by Equations 2.48 and 2.49 of the minimum radius required to support a mode with mode number  $l$  and  $N = 0$  predict that the TM $l$ 0 and the TE( $l+1$ )0 modes will be degenerate, but Figures 2.14 – 2.16 show that this is not the case. However, the difference is less than 5% in GaAs, around 10% in GaN and 15% in ZnO. The TE30 modes in all three cases

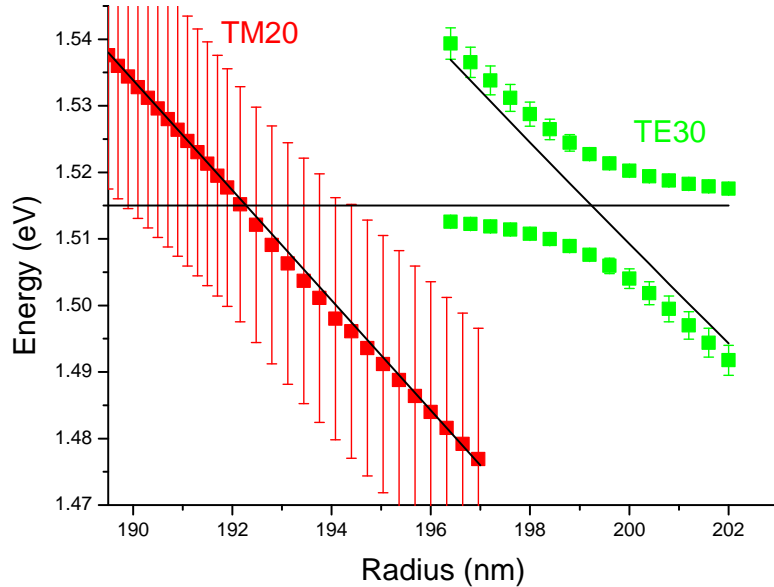


Figure 2.14: Exciton-polariton modes of GaAs. The TM20 mode is shown in red and the TE30 mode is shown in green. The square points show the real part of the exciton-polariton eigenfrequency for each mode while the vertical bars give the decay constant of the mode at each radius. The black lines mark the real part of the bare cavity modes and the exciton energy (horizontal line) for comparison.

exhibit a distinct anticrossing showing them to be strongly coupled. Conversely the TM20 modes in all three cases do not anticross and therefore are in the weak coupling regime. Table 2.2 gives the polariton splitting, calculated both from the approximate Equation 2.59 and the values found from Figures 2.14 – 2.16, and also the values of the imaginary part of the mode energies (the decay constant,  $\gamma$ ) at the anticrossing. We recall that the decay constant is the inverse of the photon lifetime so the smaller the decay constant, the longer the lifetime of the mode. The estimated polariton splitting values are shown by horizontal black lines in Figures 2.11 – 2.13 (showing the decay constant of the bare optical modes as a function of sphere radius) and it is clear in all three cases that the decay constant of the TM20 mode is greater and the decay constant of the TE30 mode is less than their respective splitting values.

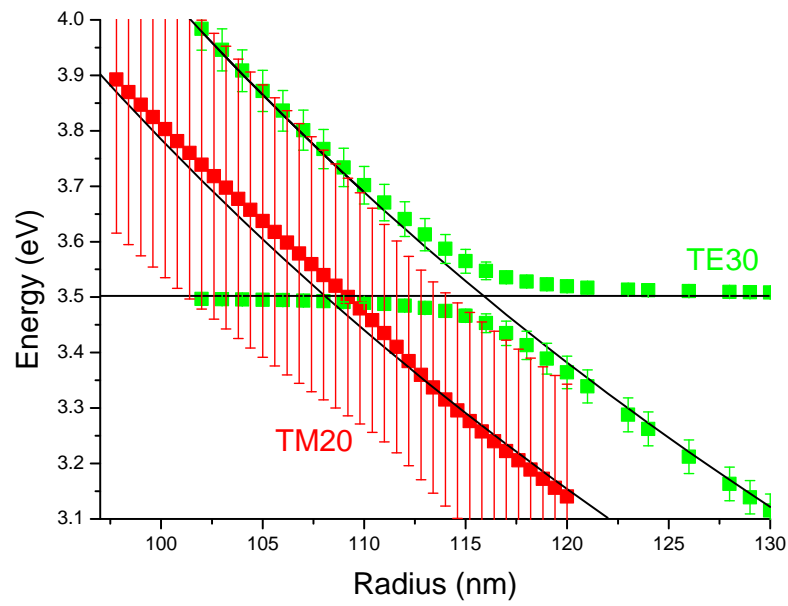


Figure 2.15: Exciton-polariton modes of GaN. The TM20 mode is shown in red and the TE30 mode is shown in green. The square points show the real part of the exciton-polariton eigenfrequency for each mode while the vertical bars give the decay constant of the mode at each radius. The black lines mark the real part of the bare cavity modes and the exciton energy (horizontal line) for comparison.

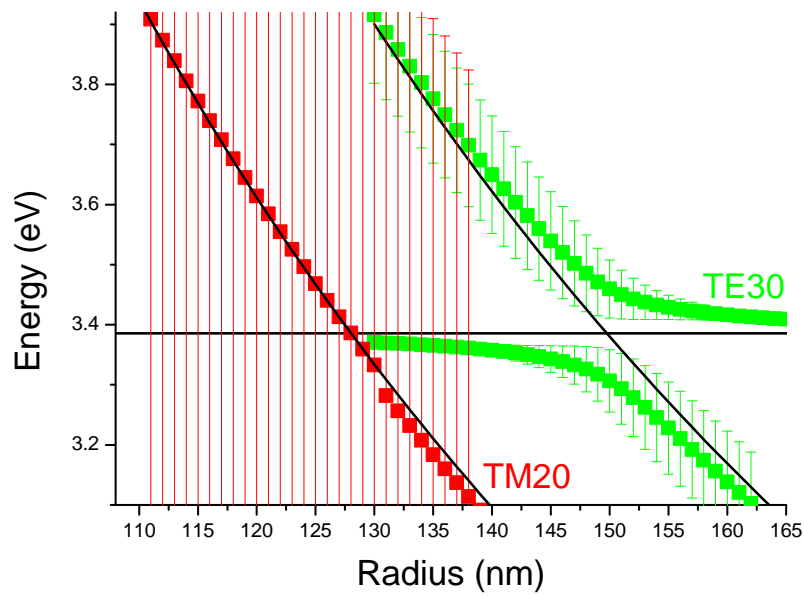


Figure 2.16: Exciton-polariton modes of ZnO. The TM20 mode is shown in red and the TE30 mode is shown in green. The square points show the real part of the exciton-polariton eigenfrequency for each mode while the vertical bars give the decay constant of the mode at each radius. The black lines mark the real part of the bare cavity modes and the exciton energy (horizontal line) for comparison.

Feature	GaAs (meV)	GaN (meV)	ZnO (meV)
bulk polariton splitting*	15.6	101	184
microsphere polariton splitting	11.9	94.4	142
decay constant for TM20	18.3	191	386
decay constant for TE30	2.6	37.0	103

Table 2.2: Values of polariton splitting and decay constants as shown in Figures 2.14 – 2.16.

\* from Equation 2.59.

For the TM20 modes, the decay constant,  $\gamma$  exceeds the splitting,  $\Delta$  given by Equation 2.59, which is characteristic of the weak coupling regime. In contrast for the TE30 modes the decay constant is smaller than the splitting so that the strong coupling is realised and the expected anticrossing is apparent.

It can be seen that the polariton splitting of the TE30 mode in GaN is over seven times greater than that in GaAs and the splitting of the TE30 mode in ZnO is one and a half times greater again. However, the decay constants in GaN are an order of magnitude greater than those in GaAs which is partly due to the lower refractive index of GaN. Equation 2.54 shows that the decay constant  $\gamma$  has an explicit inverse dependence on the refractive index. The widths of the modes in ZnO are over twice as great as those in GaN, again by virtue of the lower refractive index in ZnO.

## 2.7 Discussion

In this chapter we have considered the exciton-polariton modes for semiconductor sub-micron spheres of GaAs, GaN and ZnO. The specific conditions for the threshold of weak to strong coupling of excitons to photon modes have been found. It has been shown that optical modes with a decay constant greater than the polariton splitting are weakly coupled and those with decay constant less than the polariton splitting are strongly coupled, in accordance with accepted theory. An estimate of the polariton splitting in the spherical geometry is provided. It is also shown that modes with higher  $l$  values are more likely to have sufficiently small decay constant

for strong coupling to occur. However, as  $l$  increases the finesse of the optical cavity decreases making these modes less desirable for exciton-polariton formation. Estimates of the minimum sphere radius required to support modes of different  $l$  and of the decay constant for modes of different  $l$  are given for TE and TM modes. The weak to strong coupling threshold of the topical material, ZnO is shown to be comparable to those of other semiconductor materials in the sub-micron sphere system.

GaAs has a low binding energy of around just 4 meV, whereas GaN and ZnO are well known ‘wide band-gap’ semiconductors and have exciton binding energies of around 24 meV and 60 meV respectively. Materials with exciton binding energy much greater than the thermal energy,  $k_B T$ , in a given environment ( $k_B T = 25$  meV at room temperature) will be much more stable than excitons with binding energies below  $k_B T$ . This suggests that of the three materials considered, with all other things being equal, ZnO is the best choice for room temperature polariton devices. ZnO has been proposed as a material that would be very suitable for polariton lasing, in the visible spectrum, using a planar microcavity at room temperature [80]. This proposal is based on the stability of ZnO excitons at room temperature, the strong light-matter coupling with a very large Rabi splitting (around 120 meV) and the fact that ZnO emits in the relevant region of the electromagnetic spectrum.

However, the confinement of the photon mode must also be taken into account. The lower the dielectric constant difference between the spherical microcavity and the medium outside the sphere (vacuum,  $n = 1.0$ ) the less well the photon mode will be confined to the sphere. The better the confinement, the longer the lifetime of the mode. As shown in Table 2.1, ZnO has a low dielectric constant,  $\epsilon_b = 2.11$  and so the photon modes in ZnO are less well confined to the sphere than those in GaN ( $\epsilon_b = 7.29$ ) or GaAs ( $\epsilon_b = 13.69$ ).

Finally, we must consider the strength of the exciton-polariton coupling. The greater the Rabi splitting between the polariton modes, the stronger the coupling. The calculated splitting for GaAs was 11.9 meV, for GaN 94.4 meV and 142 meV for ZnO. This shows that, of the materials considered, the strongest coupling was found in ZnO.

In the case of sub-micron spheres it seems that to choose a material to support exciton-polaritons one must balance the need for a high exciton binding energy and strong coupling against the need for strong confinement of the optical mode and lifetime of the polariton. Decisions may then be made that are appropriate for the application.

It has been shown that sub-micron spheres are capable of supporting exciton-polariton modes. A semiconductor sphere is a simple structure and there are established techniques for their fabrication. For example, they may be chemically synthesised using colloidal chemistry techniques (spheres of inorganic oxides with diameters of the order nanometers to micrometers can be routinely produced in this way [81]). Alternatively, silica microspheres may be produced as molten droplets under their own surface tension [82]. The required whispering-gallery optical modes might be excited using a tangential fibre taper waveguide to couple into the resonator. Such a method has been shown to work in silica microspheres [83][84]. In pillar microcavities formed using Bragg mirrors, the whispering-gallery modes may be excited by a laser [85].

It should also be recognised that it is difficult to grow high quality Bragg mirrors using GaN and ZnO. The spherical geometry considered in this chapter does not require Bragg mirrors for the confinement of photons and so may be a more accessible way of fabricating exciton-polariton devices with these materials with higher binding energies.

# Chapter 3

## Tamm plasmon-polaritons in cylindrical fibres

In this chapter Tamm plasmon-polaritons (TPPs), a type of surface plasmon-polariton (SPP), are introduced and the requirements for their formation explained. A brief review of SPP properties is given and work done on SPPs in cylindrical fibres is considered. The existing framework for predicting TPPs in planar systems is presented and followed by an investigation into TPPs in cylindrical structures. A transfer matrix model is used to predict the parameters of cylindrical structures that could support TPPs and a discussion is given as to how such structures may be realised.

### 3.1 Surface plasmon-polaritons

SPPs are localized interface states that can exist at the boundary between a metal and a dielectric material. An electromagnetic field may couple to electrons near the metal surface resulting in a state with a discrete frequency at a given in-plane wavevector and a resonance in the optical response. The electromagnetic field components perpendicular to the interface decay in both the metal and the dielectric. Consider the dielectric constant of the metal,  $\varepsilon_M$  to be given by the Drude model [86]:

$$\varepsilon_M = \varepsilon_b \left( 1 - \frac{\omega_p^2}{\omega(\omega + i\Gamma)} \right) \quad (3.1)$$

where  $\varepsilon_b$  is the background dielectric constant,  $\omega_p$  is the plasma frequency and  $\Gamma$  is the plasma collision rate. For a good metal, the plasma frequency is large compared with the frequencies of interest and for the simple case,  $\Gamma = 0$  the dielectric constant is negative. Consider the wavevector components parallel ( $k_{\parallel}$ ) and normal ( $k_{\perp}$ ) to the interface. In the metal we may write:

$$k_{\perp}^2 + k_{\parallel}^2 = \varepsilon_M \frac{\omega^2}{c^2} \quad (3.2)$$

and a state with these wavevectors may be supported in a system that allows the boundary conditions for the electric and magnetic fields to be satisfied. If  $k_{\parallel}$  is real then

$$k_{\perp}^2 = -k_{\parallel}^2 + \varepsilon_M \frac{\omega^2}{c^2} \quad (3.3)$$

and for  $\varepsilon_M$  real and negative,  $k_{\perp}^2$  is negative and  $k_{\perp}$  is imaginary. A propagating wave may be written in the form

$$\mathbf{A} = A_0 \exp [i(\mathbf{k} \cdot \mathbf{r} - \omega t)]. \quad (3.4)$$

An imaginary wavevector indicates an evanescent wave that decays rather than propagates into the material. Hence, the decay of the electromagnetic field in the metal is due to the negative real part of the dielectric constant. The decay of the field in the dielectric material is due to total internal reflection. Similar to Equation 3.3 for the metal, for the dielectric material we have

$$k_{\perp}^2 = -k_{\parallel}^2 + \varepsilon \frac{\omega^2}{c^2} \quad (3.5)$$

where  $\varepsilon$  is the positive, real dielectric constant and  $k_{\perp}^2$  is negative for sufficiently large values of  $k_{\parallel}$ .

Consider a TM wave propagating along a planar interface, in the  $x$ -direction, between a dielectric (which we will call medium 1) with dielectric constant  $\varepsilon_1$  and a metal (which we will call medium 2) with dielectric constant  $\varepsilon_2$  which is real and negative (both materials are non-magnetic and so have  $\mu = 1$ ), as illustrated in Figure 3.1. For a simple incident plane wave in the dielectric, a TM polarised wave has only a magnetic field normal to the plane of incidence and its non-zero field components are  $E_x$ ,  $E_z$  and  $B_y$ . In the case of a surface wave, in the dielectric these

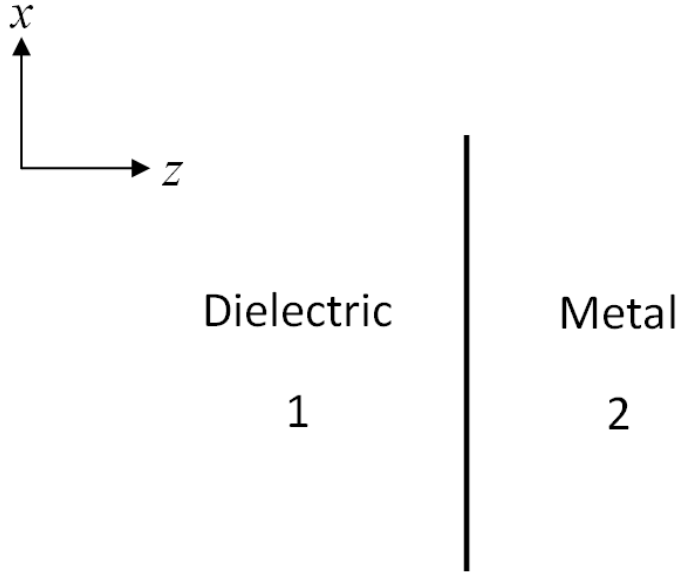


Figure 3.1: Surface plasmons may propagate along the interface between a dielectric and a metal in the  $x$ -direction.

three field components take the form:

$$\begin{aligned}
 E_x^1 &= E_{x0}^1 \exp [i(k_x x - \omega t) - \alpha z] \\
 E_z^1 &= E_{z0}^1 \exp [i(k_x x - \omega t) - \alpha z] \\
 B_y^1 &= B_{y0}^1 \exp [i(k_x x - \omega t) - \alpha z]
 \end{aligned} \tag{3.6}$$

where  $k_x$  is the wavevector in the direction of propagation,  $\alpha$  is a constant describing the decay of the field in the dielectric normal to the interface,  $\omega$  is the angular frequency,  $t$  is time and the superscript 1 denotes fields in medium 1. In the metal the fields are

$$\begin{aligned}
 E_x^2 &= E_{x0}^2 \exp [i(k_x x - \omega t) + \gamma z] \\
 E_z^2 &= E_{z0}^2 \exp [i(k_x x - \omega t) + \gamma z] \\
 B_y^2 &= B_{y0}^2 \exp [i(k_x x - \omega t) + \gamma z]
 \end{aligned} \tag{3.7}$$

where  $\gamma$  is a different constant describing the decay of the field in the metal and the superscript 2 denotes fields in medium 2. The substitution of Equations 3.6 into

Maxwell's Equations 1.4 and 1.5 gives three equations:

$$\begin{aligned}
-(ik_x E_{z0}^1 + \alpha E_{x0}^1) &= i\omega B_{y0}^1 \\
\alpha B_{y0}^1 &= -i\omega \frac{\varepsilon_1}{c^2} E_{x0}^1 \\
ik_x B_{y0}^1 &= -i\omega \frac{\varepsilon_1}{c^2} E_{z0}^1.
\end{aligned} \tag{3.8}$$

By the same argument, substituting Equations 3.7 for material 2 into Equations 1.4 and 1.5 we have:

$$\begin{aligned}
-(ik_x E_{z0}^2 - \gamma E_{x0}^2) &= i\omega B_{y0}^2 \\
-\gamma B_{y0}^2 &= -i\omega \frac{\varepsilon_2}{c^2} E_{x0}^2 \\
ik_x B_{y0}^2 &= -i\omega \frac{\varepsilon_2}{c^2} E_{z0}^2.
\end{aligned} \tag{3.9}$$

Applying the conditions that the tangential components of the electric and magnetic fields must be continuous across the boundary at  $z = 0$  gives the relation

$$\frac{\varepsilon_1}{\varepsilon_2} = -\frac{\alpha}{\gamma} \tag{3.10}$$

The wave equation in medium 1(2) may be written:

$$\nabla^2 E^{1(2)} = \frac{\varepsilon_{1(2)}}{c^2} \frac{\partial^2 E^{1(2)}}{\partial t^2} \tag{3.11}$$

where  $c$  is the speed of light in vacuum. Substitution of the fields given in Equations 3.6 and 3.7 into Equation 3.11 for materials 1 and 2 gives

$$\alpha^2 = k_x^2 - \frac{\omega^2}{c^2} \varepsilon_1 \tag{3.12}$$

and

$$\gamma^2 = k_x^2 - \frac{\omega^2}{c^2} \varepsilon_2 \tag{3.13}$$

respectively. A SPP requires the  $z$ -component of the wavevector to be imaginary. This may be achieved when  $\omega^2 \varepsilon_{1,2}/c^2 < k_x^2$ . Substitution of Equations 3.12 and 3.13 into 3.10 gives the dispersion relation

$$k_x = \frac{\omega}{c} \sqrt{\left( \frac{\varepsilon_1 \varepsilon_2}{\varepsilon_1 + \varepsilon_2} \right)}. \tag{3.14}$$

For the TE polarisation the non-zero field components should be  $B_x$ ,  $B_z$  and  $E_y$  and for a wave travelling in the  $x$ -direction in medium 1 and medium 2 we should seek solutions of the form:

$$\begin{aligned}
B_x^1 &= B_{x0}^1 \exp [i(k_x x - \omega t) - \alpha z] \\
B_z^1 &= B_{z0}^1 \exp [i(k_x x - \omega t) - \alpha z] \\
E_y^1 &= E_{y0}^1 \exp [i(k_x x - \omega t) - \alpha z] \\
B_x^2 &= B_{x0}^2 \exp [i(k_x x - \omega t) + \gamma z] \\
B_z^2 &= B_{z0}^2 \exp [i(k_x x - \omega t) + \gamma z] \\
E_y^2 &= E_{y0}^2 \exp [i(k_x x - \omega t) + \gamma z].
\end{aligned} \tag{3.15}$$

Substituting the field components from Equations 3.15 into Maxwell's equations and applying the tangential boundary conditions gives

$$\alpha = -\gamma. \tag{3.16}$$

The wave equation for the magnetic field with the fields given in Equations 3.15 gives the same relations as those in Equations 3.12 and 3.13. However, the excitation can not be localized at the interface if Equation 3.16 holds since the field would not decay away from the interface in one direction. Hence TE surface plasmon-polaritons can not exist.

The dispersion relation illustrated in Figure 3.2 is for TM-polarised SPPs at an interface between a lossless metal (medium 2) with plasma frequency  $\omega_p = 8.9$  eV, corresponding to gold, and SiO<sub>2</sub> (medium 1 with  $\varepsilon_1 = 5.617$ ). The dispersion lies outside the light cone for photons in medium 1 given by  $\omega = ck/\sqrt{\varepsilon_1}$ . This means that photons incident on the metal layer from medium 1 do not have sufficiently large in-plane wavevector,  $k_x$  to excite a surface plasmon-polariton mode at any frequency. To overcome this, a diffraction grating may be used at the metal-dielectric interface. The periodic patterning of the metal surface allows the in-plane wavevector to be increased by integer multiples of  $2\pi/a$  where  $a$  is the distance between lines in the grating [87]. An alternative to the use of a diffraction grating is to include a thin spacer layer with refractive index lower than that of the dielectric material 1 at the dielectric - metal interface. If the thickness of the spacer layer is of the order

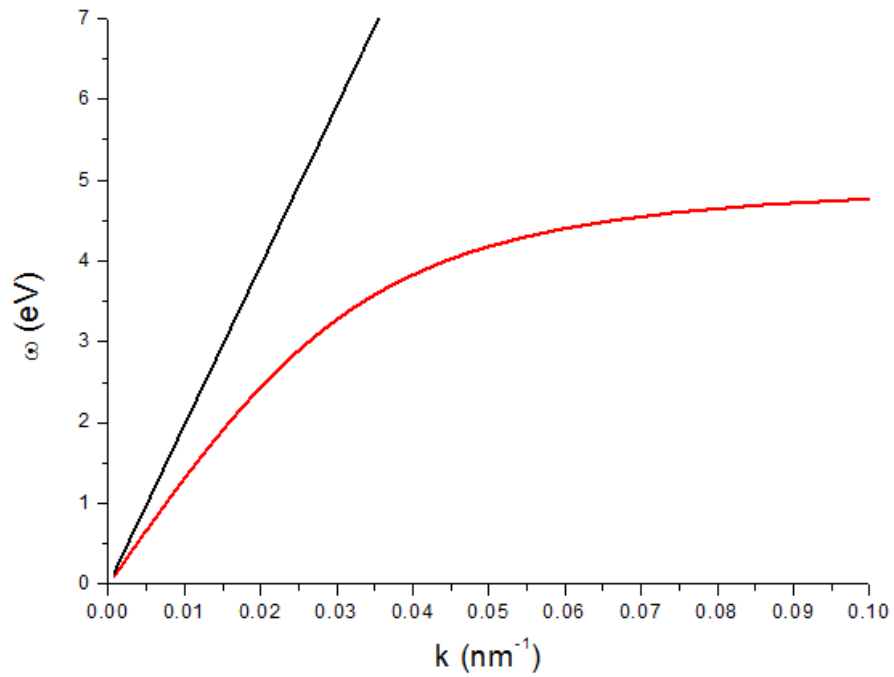


Figure 3.2: The dispersion relations for a photon (black) and a surface plasmon-polariton (red) at an interface between gold and  $\text{SiO}_2$ . The SPP dispersion lies outside the light cone of bulk  $\text{SiO}_2$ .

of the wavelength of light in that medium then the evanescent wave from medium 1 has an in-plane wavevector proportional to the higher refractive index and so is able to excite a surface plasmon at the spacer layer - metal interface. This is called frustrated total internal reflection due to the energy not being totally reflected but tunnelling through the low refractive index layer to excite the SPP [88].

### 3.1.1 Uses of surface plasmon-polaritons

Surface plasmon-polaritons (SPPs) are of multidisciplinary interest and have been used in and proposed for many different applications. Their use is well established in commercial sensors for molecular biological systems due to their great sensitivity to small changes in refractive index [31]. In 2005 Fang *et al.* demonstrated subwavelength imaging with a silver superlens that makes use of SPPs to enhance evanescent waves and produce an image with resolution below the diffraction limit [37]. Also in that year, Krasavi *et al.* demonstrated optical switching using the fact that the propagation of SPPs depends strongly on properties of the metal at the interface [38]. Furthermore, the growing field of plasmonics, using SPPs to control light on nanometer scales, promises technological developments such as computer chips able to transfer data very quickly on small length scales [33][89]. In 1998 Ebbesen *et al.* [34] showed that transmission of light through a submicron array of holes in a metal is enhanced by orders of magnitude due to the coupling of light to surface plasmons on the surface of the metal. Plasmonics is not restricted to planar systems. Nanorods, nanoparticles and other nanoscale structures have been shown to exhibit novel effects due to the presence of surface plasmons [2]. For example, metal nanoparticles that exhibit plasmon resonance can be used as bright tags for biosensing [36]. A comprehensive review of surface plasmon-polaritons is given by Pitarke *et al.* [32].

## 3.2 Tamm plasmon-polaritons

Tamm plasmon-polaritons (TPPs) are another type of state that can occur at a metal surface, this time at an interface between a metal and a dielectric Bragg mirror as illustrated in Figure 3.3. The Bragg reflector structure is that introduced in Section 1.2. The existence of TPPs at a metal – Bragg reflector interface was proposed theoretically in 2007 by Kaliteevski *et al.* [41] following the work of Kavokin *et al.* on Tamm states at the interface between two periodic dielectric structures [90]. They were subsequently demonstrated experimentally by Sasin *et al.* [42]. As for conventional surface plasmons, the decay of the field in the metal is due to the

negative dielectric constant. However, the decay of the field in the Bragg mirror is not due to total internal reflection but to the photonic band gap arising from the dielectric layered structure. The name *Tamm* plasmon-polariton comes from the analogy with electronic surface states proposed by Tamm in 1932 [91]. These electronic surface states are the result of the overlapping orbitals of dangling bonds where a periodic lattice has been truncated and they have a wavefunction that decays exponentially away from the interface. Electronic Tamm states were first experimentally observed by Ohno *et al.* in 1990 [92].

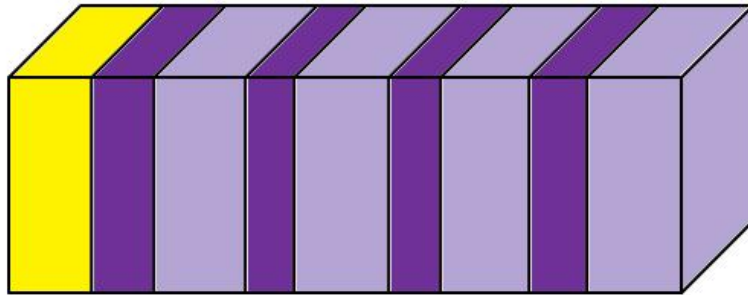


Figure 3.3: A planar structure to support a Tamm plasmon-polariton. The yellow represents the metal layer, the two shades of blue represent the periodic layers of the dielectric Bragg reflector. The TPP is formed at the interface between the metal and the first Bragg reflector layer.

Reflection spectra for an example of a planar Bragg reflector are shown in Figure 3.4. The three spectra are for structures with different numbers of pairs of layers. The plateau region with a reflection coefficient of magnitude equal to unity for the case of 12 pairs of layers (black line) indicates the photonic band gap. It is clear that the more layers there are in the structure, the closer the magnitude of the reflection coefficient is to unity in the band gap.

Contrary to the case for surface plasmons, TPPs can exist in both the TE and TM polarisations. This is because both the Bragg reflector and the metal layer are essentially mirrors acting to confine the light.

Kaliteevski *et al.* [41] showed the requirements for TPPs to exist with zero wavevector parallel to the metal – Bragg reflector interface. Consider an arbitrary

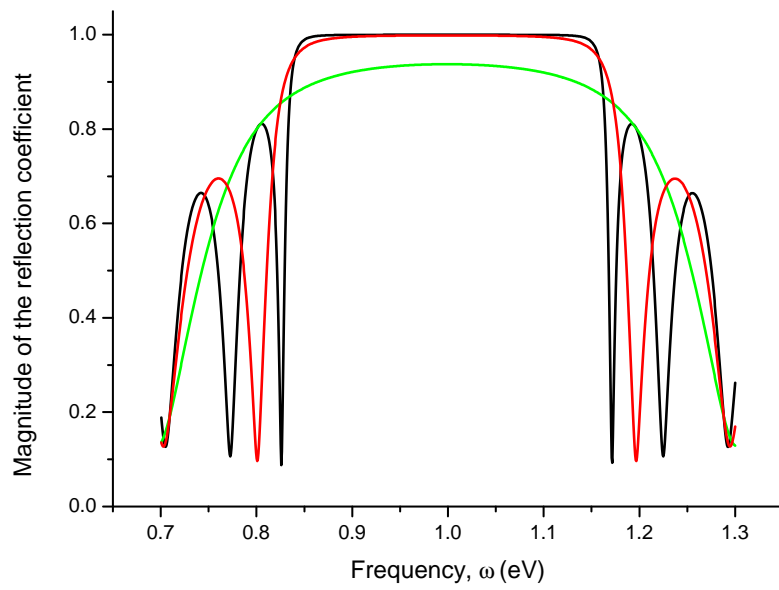


Figure 3.4: The reflection spectra for planar Bragg reflectors with alternating layers of refractive index  $n_A = 2.37$ ,  $n_B = 1.47$ . The black line shows the spectrum for a structure with 12 pairs of layers; red is for 8 pairs of layers and green is for 4 pairs of layers. The thickness of each layer of the Bragg reflector was chosen to give maximum reflection, and to centre the photonic stop band, at a frequency of 1.0 eV.

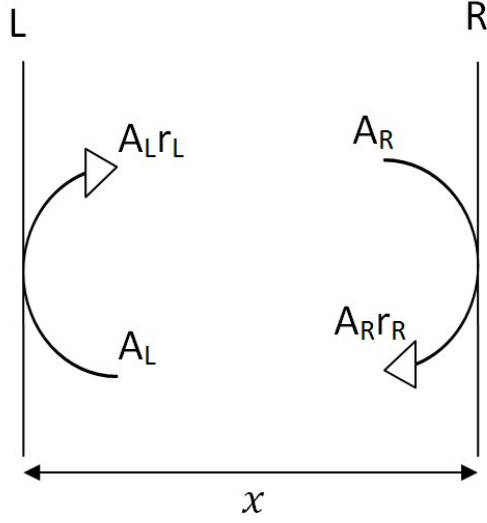


Figure 3.5: Two virtual interfaces, left (L) and right (R) in a homogeneous medium a distance  $x$  apart with fields incident upon each boundary ( $A_R$  and  $A_L$ ) and the fields reflected from each boundary where  $r_R$  and  $r_L$  are the amplitude reflection coefficients from the right and left respectively.

homogeneous layer of thickness  $x$ , with virtual boundaries as shown in Figure 3.5 (this may for example be placed within the first dielectric layer of the Bragg reflector structure adjacent to the metal). L and R mark the left and right hand boundaries respectively. The electric field incident upon the right (left) hand boundary is denoted  $A_{R(L)}$  and the field reflected from that right (left) hand boundary is then  $A_{R(L)}r_{R(L)}$  where  $r_{R(L)}$  is the amplitude reflection coefficient from boundary R(L). On making a transit from left to right across the cavity, radiation accumulates phase  $\Phi = nx\omega/c$  where  $n$  is the refractive index of the layer,  $x$  is the layer thickness and  $\omega$  is the frequency and we can write the transfer matrix equation

$$\begin{pmatrix} \exp(i\Phi) & 0 \\ 0 & \exp(-i\Phi) \end{pmatrix} \begin{pmatrix} A_L r_L \\ A_L \end{pmatrix} = \begin{pmatrix} A_R \\ A_R r_R \end{pmatrix} \quad (3.17)$$

in the basis of left and right propagating waves, or

$$\begin{pmatrix} \exp(i\Phi) & 0 \\ 0 & \exp(-i\Phi) \end{pmatrix} \begin{pmatrix} r_L \\ 1 \end{pmatrix} = A \begin{pmatrix} 1 \\ r_R \end{pmatrix} \quad (3.18)$$

where  $A = A_R/A_L$ . Eliminating  $A$  from the two equations represented by Equation

3.18 gives

$$r_L r_R \exp(2i\Phi) = 1. \quad (3.19)$$

Recalling that the boundaries L and R created a virtual cavity we may eliminate their separation by taking  $x$  to zero leaving

$$r_L r_R = 1. \quad (3.20)$$

This means that at any given point, the product of the amplitude reflection coefficients for left and right propagating waves should be equal to unity for a mode to exist. Alternatively, without reducing  $x$  to zero, we may consider any cavity within the structure and require the round trip phase difference to be an integer multiple of  $2\pi$ . In a planar system, it is apparent that Equation 3.20 can be satisfied at a metal – Bragg reflector interface ( $r_M r_{BR} = 1$ ). The amplitude reflection coefficient for a metal  $r_M$  is close to -1 for frequencies that are much less than the plasma frequency of the metal (see Section 3.2.1). Also the amplitude reflection coefficient for a Bragg reflector,  $r_{BR}$ , is close to -1 if the Bragg reflector structure has each layer with an optical thickness of  $\lambda/4$  where  $\lambda$  is the wavelength of light in the particular layer, the refractive index of the first layer of the Bragg reflector (adjacent to the metal) is greater than that of the next layer (see Section 3.2.2) and there are sufficient layers in the Bragg reflector for the magnitude of the reflection coefficient to be close to unity at frequencies close to the Bragg frequency.

### 3.2.1 Reflection from the metal

The reflection coefficient from the metal,  $r_M$  may be calculated using the Fresnel formula:

$$r_M = \frac{(n_A - n_M)}{(n_A + n_M)} \quad (3.21)$$

where  $n_M = \sqrt{\epsilon_M}$  is the refractive index of the metal,  $n_A$  is the refractive index of the dielectric layer adjacent to the metal. The Drude model given in Equation 3.1 may be used to calculate  $n_M$ . If we consider frequencies well below the metal plasma frequency such that  $\omega \ll \omega_p$  and consider loss as being negligible we can write

$$n_M^2 \approx \epsilon_b \left( 1 - \frac{\omega_p^2}{\omega^2} \right) \quad (3.22)$$

where  $\omega_p^2/\omega^2 \gg 1$  hence

$$n_M \approx i\sqrt{\varepsilon_b} \frac{\omega_p}{\omega}. \quad (3.23)$$

Substituting Equation 3.23 into Equation 3.21 and neglecting terms in  $\omega^2/\omega_p^2$  which are small gives

$$r_M \approx -1 - \frac{2i\omega n_A}{\sqrt{\varepsilon_b}\omega_p} \quad (3.24)$$

$$\approx -\exp\left(\frac{2i\omega n_A}{\sqrt{\varepsilon_b}\omega_p}\right) \quad (3.25)$$

or we can write

$$r_M \approx \exp\left[i\left(\pi + \frac{2\omega n_A}{\sqrt{\varepsilon_b}\omega_p}\right)\right]. \quad (3.26)$$

### 3.2.2 Reflection from the Bragg reflector

The reflection coefficient from a multilayer planar structure may be calculated using a transfer matrix method [93]. As described in the appendix we consider an  $N$  layer Bragg reflector with alternating layers of refractive index  $n_A$  and  $n_B$  with thicknesses  $a$  and  $b$  respectively such that the optical thickness of each layer is:

$$n_A a = n_B b = \frac{\pi c}{2\omega_0} \quad (3.27)$$

where  $\omega_0$  is the Bragg frequency. It then follows that for a frequency close to the Bragg frequency,  $\omega = \omega_0 + \delta\omega$  and a sufficiently large value of  $N$ , the expressions for the reflection coefficient are:

$$\begin{aligned} r_{BR}|_{n_A > n_B} &= -\exp\left[i\pi \frac{n_A}{n_A - n_B} \frac{\delta\omega}{\omega_0}\right] \\ r_{BR}|_{n_B > n_A} &= \exp\left[i\pi \frac{n_B}{n_B - n_A} \frac{\delta\omega}{\omega_0}\right] \end{aligned} \quad (3.28)$$

and we can see that reversing the order of the layers in the Bragg reflector causes a phase change of  $\pi$  in the reflection coefficient.

In order to satisfy the equation  $r_M r_{BR} = 1$  with  $r_M \approx -1$  we require  $r_{BR} \approx -1$  also which can only be achieved for small  $\delta\omega$  if  $n_A > n_B$ . However, the condition  $r_M r_{BR} = 1$  may be satisfied for  $n_B > n_A$  if we are prepared to vary the thickness of the first ( $A$ ) layer of the Bragg reflector from  $\lambda/4$ .

Kaliteevski *et al.* [41] considered the effect on the eigenfrequency of the thickness of the dielectric layer adjacent to the metal. They reported numerical calculations of a TPP structure for non-zero as well as zero in-plane wavevector. The energy for TE and TM modes were found to be degenerate at zero in-plane wavevector and to increase parabolically with increasing in-plane wavevector,  $k$ , with the TM mode having slightly higher energy than the TE mode. The in-plane effective mass,  $m^*$  of the TPP was calculated from the  $\omega(k)$  dispersion curve:

$$m^* = \hbar^2 \left( \frac{\partial^2 \omega}{\partial k^2} \right)^{-1} \quad (3.29)$$

and was reported as  $1.7 \times 10^{-5} m_e$  for the TE mode where  $m_e$  is the mass of an electron. The effective mass was slightly smaller for the TM mode.

Brand *et al.* [94] have reported calculations in which the energy of TPPs may be altered by changing the layer order and the thickness of layers in planar structures.

### 3.2.3 Other work on TPPs

In 2008 TPPs were first demonstrated experimentally by Sasin *et al.* [42]. They investigated Bragg reflector structures made of GaAs/Ga<sub>0.1</sub>Al<sub>0.9</sub>As capped with gold films of thickness 30 and 50 nm. Reflectivity and transmission measurements were made and evidence of TPPs was provided by features in the respective spectra.

TPPs have been shown experimentally to exhibit strong coupling with quantum well excitons producing a polaritonic emission that has the potential to be used in polariton lasers [43]. Strong coupling between TPPs and quantum well excitons has also been demonstrated using angular resolved reflectivity measurements in extremely compact structures with just five layers [48]. A large refractive index contrast between the layers makes possible high reflectivity for such a small Bragg structure which potentially could be used in integrated devices.

It has been predicted that planar Bragg reflectors containing a quantum well in a microcavity layer with metal deposited on the surface can be designed to exhibit strong coupling between a TPP and an exciton-polariton [49]. Furthermore it has been proposed that metal patterning on the surface of the structure could be used to create a channel in which the energy of the hybrid mode is lower than that

of the bare exciton-polariton mode, resulting in confinement and the potential for polariton integrated circuits which might find use in ultrafast information processing [44]. Tamm plasmon-polaritons have also been proposed for use in optical absorbers [46] and switches [47].

### 3.3 Cylindrical structures

This section describes the transfer matrix which allows for the calculation of electromagnetic fields in cylindrical multilayer structures. In Section 3.4 the transfer matrix method is used to describe the fields in simpler structures, such as step-index fibres, by reducing the transfer matrix to the identity matrix. The results of calculations for Tamm plasmon-polaritons obtained for this thesis and reported in Sections 3.4 and 3.6 were obtained using this method.

#### 3.3.1 Transfer matrix method

A method of calculating the mode structure of multilayer optical fibres and similar structures using the transfer matrix method was derived by Al-Bader and Imtaar [50] and independently by Kaliteevski *et al.* [95] and is summarised here.

Consider modes with electric and magnetic fields of the form:

$$\begin{aligned}\mathbf{E} &= E(\boldsymbol{\rho}) \exp [i(\beta \mathbf{z} + m\phi)] \\ c\mathbf{B} &= cB(\boldsymbol{\rho}) \exp [i(\beta \mathbf{z} + m\phi)]\end{aligned}\tag{3.30}$$

where the cylindrical coordinate directions  $\boldsymbol{\rho}$ ,  $\phi$  and  $\mathbf{z}$  are shown in Figure 3.6,  $\beta$  is the propagation constant and  $m$  is the quantum number describing the azimuthal variation of the fields. Taking two of Maxwell's Equations, 1.4 and 1.5, with an assumed time dependence of the form  $\exp(-i\omega t)$  we have:

$$\begin{aligned}\nabla \times \mathbf{E} &= i\omega \mathbf{B} \\ \nabla \times \mathbf{B} &= -i\omega \frac{n^2}{c^2} \mathbf{E}\end{aligned}\tag{3.31}$$

Substituting Equation set 3.30 into Equation set 3.31 the  $\phi$  and  $\rho$  field compo-

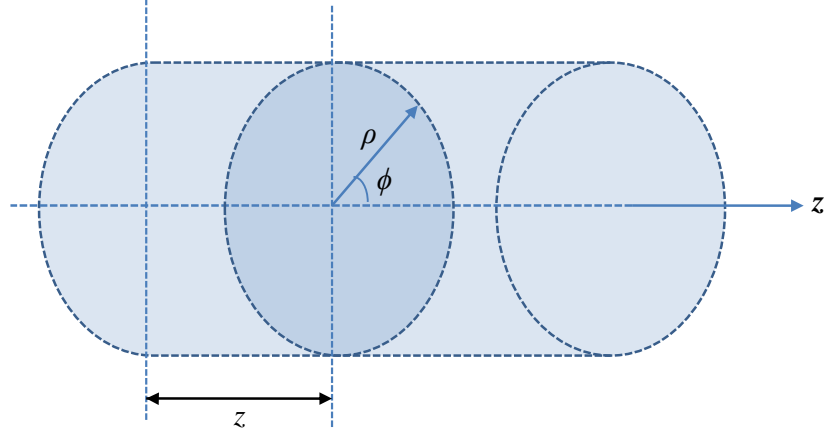


Figure 3.6: In the cylindrical coordinate system  $\rho$  is the radial vector,  $\phi$  is a vector giving the azimuthal angle and  $z$  is parallel to the cylinder axis.

nents may be expressed in terms of  $E_z$  and  $cB_z$  fields:

$$\begin{aligned}
 E_\rho &= \frac{1}{k^2} \left( i\beta \frac{\partial E_z}{\partial \rho} - \frac{k_0 m}{\rho} cB_z \right) \\
 E_\phi &= -\frac{1}{k^2} \left( \frac{\beta m}{\rho} E_z + ik_0 \frac{\partial cB_z}{\partial \rho} \right) \\
 cB_\rho &= \frac{1}{k^2} \left( \frac{n^2 k_0 m}{\rho} E_z + i\beta \frac{\partial cB_z}{\partial \rho} \right) \\
 cB_\phi &= \frac{1}{k^2} \left( ik_0 n^2 \frac{\partial E_z}{\partial \rho} - \frac{\beta m}{\rho} cB_z \right)
 \end{aligned} \tag{3.32}$$

where the radial wavevector  $k$  is given by  $k^2 = (n^2 k_0^2) - \beta^2$  with  $k_0 = \omega/c$ .

The cylindrical form of the scalar wave equation for the component  $E_z$  is

$$\left[ \frac{\partial^2}{\partial \rho^2} + \frac{1}{\rho} \frac{\partial}{\partial \rho} + \frac{1}{\rho^2} \frac{\partial^2}{\partial \phi^2} + (k^2 - \beta^2) \right] E_z(\rho, \phi) = 0 \tag{3.33}$$

which, after separating the variables, may be rewritten in the form of the Bessel equation [96]:

$$\frac{\partial^2 E_z}{\partial \rho^2} + \frac{1}{\rho} \frac{\partial E_z}{\partial \rho} + \left( k^2 - \beta^2 - \frac{m^2}{\rho^2} \right) E_z(\rho) = 0 \tag{3.34}$$

with solutions of the form

$$E_z = A_1 J_m(k\rho) + B_1 N_m(k\rho) \tag{3.35}$$

where  $J_m(x)$  and  $N_m(x)$  are Bessel and Neumann functions respectively and  $A_1$  and  $B_1$  are constants. The forms of the Bessel and Neumann functions for orders  $m = 0$  and 1 are shown in Figures 3.7 and 3.8

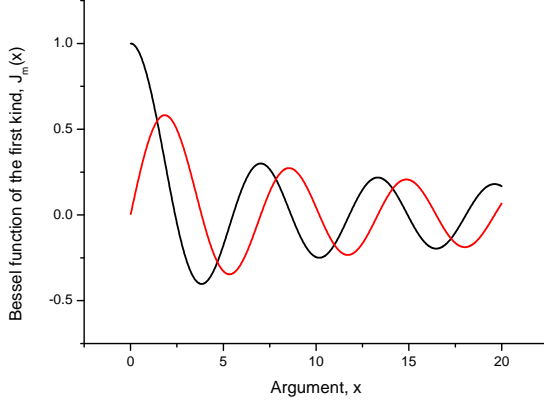


Figure 3.7: Function  $J_m(x)$  for  $m = 0$  (black line) and  $m = 1$  (red line).

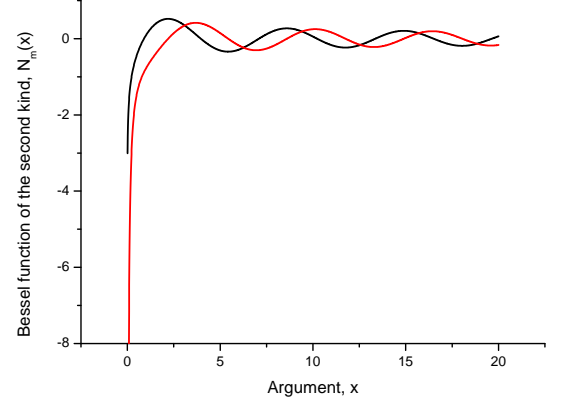


Figure 3.8: Function  $N_m(x)$  for  $m = 0$  (black line) and  $m = 1$  (red line).

A similar analysis for the  $cB_z$ -component gives solutions of the form

$$cB_z = A_2 J_m(k\rho) + B_2 N_m(k\rho) \quad (3.36)$$

where  $A_2$  and  $B_2$  are constants. Substituting Equations 3.35 and 3.36 into the  $E_\phi$  and  $cB_\phi$  components (Equations 3.32) gives:

$$E_\phi = -\frac{\beta m}{k^2 \rho} [A_1 J_m(k\rho) + B_1 N_m(k\rho)] - \frac{ik_0}{k} [A_2 J'_m(k\rho) + B_2 N'_m(k\rho)] \quad (3.37)$$

$$cB_\phi = \frac{ik_0 n^2}{k} [A_1 J'_m(k\rho) + B_1 N'_m(k\rho)] - \frac{\beta m}{k^2 \rho} [A_2 J_m(k\rho) + B_2 N_m(k\rho)] \quad (3.38)$$

where the prime denotes the derivative with respect to the whole argument of the function:  $J'_m(k\rho) = d/d(k\rho)[J_m(k\rho)]$ .

The transfer matrix method in a cylindrical system facilitates the calculation of an electromagnetic field at a radius  $\rho$  given that the field at another radius,  $\rho_0$ , is already known and where  $\rho_0$  and  $\rho$  are points within a layer of the structure.

Specifically, we can write

$$\begin{pmatrix} E_z(\rho) \\ cB_\phi(\rho) \\ cB_z(\rho) \\ E_\phi(\rho) \end{pmatrix} = \hat{M}(\rho_0, \rho) \begin{pmatrix} E_z(\rho_0) \\ cB_\phi(\rho_0) \\ cB_z(\rho_0) \\ E_\phi(\rho_0) \end{pmatrix} \quad (3.39)$$

where  $\hat{M}(\rho_0, \rho)$  is the  $4 \times 4$  transfer matrix between the points  $\rho_0$  and  $\rho$  and we choose to represent the magnetic field component in terms of  $c\mathbf{B}$  in order to maintain consistent units with the electric field components ( $\text{Vm}^{-1}$  or  $\text{m kg s}^{-3} \text{A}^{-1}$  in SI base units). The field components that make up the vectors in Equation 3.39 are parallel to the interfaces in a multilayer fibre. At the interface between two layers with different refractive indices these components must be continuous. The transfer matrix across a multi-layer structure is the product of the transfer matrices for the individual layers correctly ordered to propagate the fields from the selected start point to the selected end point. For example, for a structure with three layers around a core with the inner most layer having an individual transfer matrix  $\hat{M}_1$ , the middle layer having transfer matrix  $\hat{M}_2$  and the outermost layer having transfer matrix  $\hat{M}_3$  we may calculate the fields at the outer edge of the structure by applying the transfer matrix  $\hat{M}_{\text{tot}}$  to the known field at the outside edge of the core where

$$\hat{M}_{\text{tot}} = \hat{M}_3 \cdot \hat{M}_2 \cdot \hat{M}_1. \quad (3.40)$$

Similarly to calculate the field at the edge of the core we should apply the transfer matrix  $\hat{M}'_{\text{tot}}$  to the known field at the edge of the structure where

$$\hat{M}'_{\text{tot}} = \hat{M}_1 \cdot \hat{M}_2 \cdot \hat{M}_3. \quad (3.41)$$

Media with continually varying refractive index can be approximated by a multilayer structure with suitably thin layers.

Once the vector on the left hand side of Equation 3.39 has been determined, the radial field components may be calculated using Equations 3.32. By setting the

right hand vector in Equation 3.39 consecutively to be:

$$\begin{pmatrix} E_z(\rho_0) \\ cB_\phi(\rho_0) \\ cB_z(\rho_0) \\ E_\phi(\rho_0) \end{pmatrix} = \begin{pmatrix} 1 \\ 0 \\ 0 \\ 0 \end{pmatrix}, \begin{pmatrix} 0 \\ 1 \\ 0 \\ 0 \end{pmatrix}, \begin{pmatrix} 0 \\ 0 \\ 1 \\ 0 \end{pmatrix}, \begin{pmatrix} 0 \\ 0 \\ 0 \\ 1 \end{pmatrix} \quad (3.42)$$

expressions may be calculated for the constants  $A_1$ ,  $A_2$ ,  $B_1$  and  $B_2$  in Equations 3.35 and 3.36 and hence the elements of the transfer matrix  $\hat{M}$  may be found. Writing  $\hat{M}$  as

$$\hat{M} = \begin{pmatrix} M_{11} & M_{12} & M_{13} & M_{14} \\ M_{21} & M_{22} & M_{23} & M_{24} \\ M_{31} & M_{32} & M_{33} & M_{34} \\ M_{41} & M_{42} & M_{43} & M_{44} \end{pmatrix} \quad (3.43)$$

the matrix elements are found to be:

$$\begin{aligned} M_{11} &= k\rho_0 \frac{\pi}{2} \left[ N'_m(k\rho_0)J_m(k\rho) - J'_m(k\rho_0)N_m(k\rho) \right] \\ M_{21} &= in^2k_0\rho_0 \frac{\pi}{2} \left[ N'_m(k\rho_0)J'_m(k\rho) - J'_m(k\rho_0)N'_m(k\rho) \right] \\ &\quad + \frac{i\beta^2m^2\pi}{k^2k_0\rho} \frac{\pi}{2} \left[ N_m(k\rho_0)J_m(k\rho) - J_m(k\rho_0)N_m(k\rho) \right] \\ M_{31} &= -\frac{i\beta m\pi}{k_0} \frac{\pi}{2} \left[ N_m(k\rho_0)J_m(k\rho) - J_m(k\rho_0)N_m(k\rho) \right] \\ M_{41} &= -\frac{\beta m\rho_0\pi}{k\rho} \frac{\pi}{2} \left[ N'_m(k\rho_0)J_m(k\rho) - J'_m(k\rho_0)N_m(k\rho) \right] \\ &\quad + \frac{\beta m\pi}{k} \frac{\pi}{2} \left[ N'_m(k\rho)J_m(k\rho_0) - J'_m(k\rho)N_m(k\rho_0) \right] \end{aligned}$$

$$\begin{aligned}
M_{12} &= \frac{ik^2\rho_0}{n^2k_0} \frac{\pi}{2} [N_m(k\rho_0)J_m(k\rho) - J_m(k\rho_0)N_m(k\rho)] \\
M_{22} &= k\rho_0 \frac{\pi}{2} \left[ N'_m(k\rho)J_m(k\rho_0) - J'_m(k\rho)N_m(k\rho_0) \right] \\
M_{32} &= 0 \\
M_{42} &= \frac{-i\beta m}{n^2k_0} \frac{\rho_0}{\rho} \frac{\pi}{2} [N_m(k\rho_0)J_m(k\rho) - J_m(k\rho_0)N_m(k\rho)] \\
\\
M_{13} &= \frac{i\beta m}{n^2k_0} \frac{\pi}{2} [N_m(k\rho_0)J_m(k\rho) - J_m(k\rho_0)N_m(k\rho)] \\
M_{23} &= -\frac{\beta m}{k} \frac{\pi}{2} \left[ N_m(k\rho_0)J'_m(k\rho) - J_m(k\rho_0)N'_m(k\rho) \right] \\
&\quad - \frac{\beta m}{k} \frac{\pi}{2} \frac{\rho_0}{\rho} \left[ N'_m(k\rho_0)J_m(k\rho) - J'_m(k\rho_0)N_m(k\rho) \right] \\
M_{33} &= k\rho_0 \frac{\pi}{2} \left[ N'_m(k\rho_0)J_m(k\rho) - J'_m(k\rho_0)N_m(k\rho) \right] \\
M_{43} &= -\frac{i\beta^2 m^2}{n^2k^2k_0\rho} \frac{\pi}{2} [N_m(k\rho_0)J_m(k\rho) - J_m(k\rho_0)N_m(k\rho)] \\
&\quad - ik_0\rho_0 \frac{\pi}{2} \left[ N'_m(k\rho_0)J'_m(k\rho) - J'_m(k\rho_0)N'_m(k\rho) \right] \\
\\
M_{14} &= 0 \\
M_{24} &= \frac{i\beta m}{k_0} \frac{\rho_0}{\rho} \frac{\pi}{2} [N_m(k\rho_0)J_m(k\rho) - J_m(k\rho_0)N_m(k\rho)] \\
M_{34} &= -\frac{ik^2\rho_0}{k_0} \frac{\pi}{2} [N_m(k\rho_0)J_m(k\rho) - J_m(k\rho_0)N_m(k\rho)] \\
M_{44} &= k\rho_0 \frac{\pi}{2} \left[ N'_m(k\rho)J_m(k\rho_0) - J'_m(k\rho)N_m(k\rho_0) \right]. \tag{3.44}
\end{aligned}$$

The field at the centre of the core,  $\rho = 0$ , must be finite hence the constants  $B_1$  and  $B_2$  in Equations 3.35 and 3.36 in the core are necessarily zero giving:

$$\begin{aligned}
E_z|_{\text{core}} &= A_{1c}J_m(k_c\rho) \\
cB_z|_{\text{core}} &= A_{2c}J_m(k_c\rho) \tag{3.45}
\end{aligned}$$

where the subscript  $c$  denotes parameter values for the core region. Outside the fibre at radius greater than  $\rho = \rho_f$  if a decaying solution is possible and is sought,  $A_1$  and  $A_2$  in Equations 3.35 and 3.36 will be zero and we can write:

$$\begin{aligned}
E_z|_f &= B_{1f}K_m(k_f\rho) \\
cB_z|_f &= B_{2f}K_m(k_f\rho) \tag{3.46}
\end{aligned}$$

where the subscript  $f$  denotes parameter values outside the final layer of the structure and  $K_m(x)$  is the modified Bessel function of the second kind. Modified Bessel functions grow or decay exponentially and their behaviour for  $m = 0$  and  $m = 1$  is shown in Figures 3.9 and 3.10.

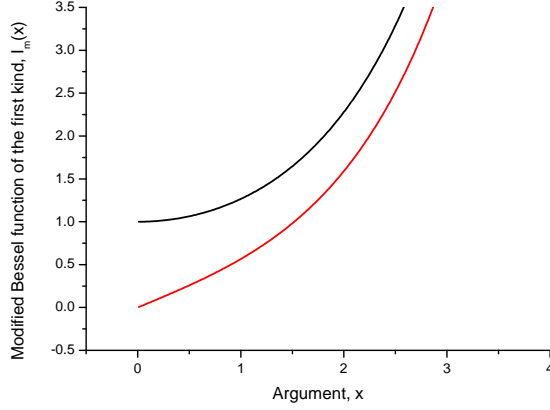


Figure 3.9: Function  $I_m(x)$  for  $m = 0$  (black line) and  $m = 1$  (red line).

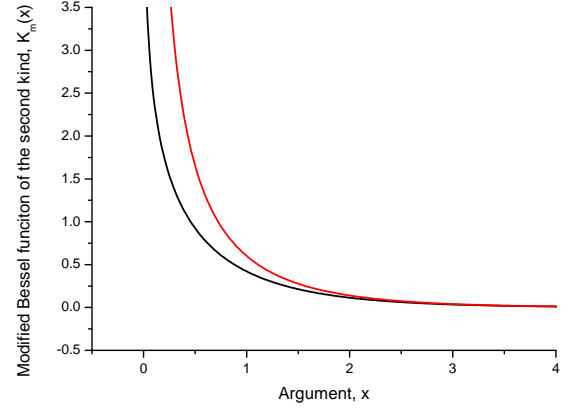


Figure 3.10: Function  $K_m(x)$  for  $m = 0$  (black line) and  $m = 1$  (red line).

Using Equations 3.37, 3.38 and 3.45, the field at the inner edge of the core,  $\rho_c$  can be written in matrix form:

$$\begin{pmatrix} E_z(k_c \rho_c) \\ cB_\phi(k_c \rho_c) \\ cB_z(k_c \rho_c) \\ E_\phi(k_c \rho_c) \end{pmatrix} = \begin{pmatrix} J_m(k_c \rho_c) & 0 \\ \frac{ik_0 n_c^2}{k_c} J'_m(k_c \rho_c) & -\frac{\beta m}{k_c^2 \rho_c} J_m(k_c \rho_c) \\ 0 & J_m(k_c \rho_c) \\ -\frac{\beta m}{k_c^2 \rho_c} J_m(k_c \rho_c) & -\frac{ik_0}{k_c} J'_m(k_c \rho_c) \end{pmatrix} \begin{pmatrix} A_{1c} \\ A_{2c} \end{pmatrix} \\ = \hat{\Omega}_c \begin{pmatrix} A_{1c} \\ A_{2c} \end{pmatrix}. \quad (3.47)$$

In a similar way Equations 3.32 and 3.46 give the field at the outside edge of the

fibre at radius  $\rho_f$  as:

$$\begin{aligned} \begin{pmatrix} E_z(k_f \rho_f) \\ cB_\phi(k_f \rho_f) \\ cB_z(k_f \rho_f) \\ E_\phi(k_f \rho_f) \end{pmatrix} &= \begin{pmatrix} K_m(k_f \rho_f) & 0 \\ \frac{ik_0 n_f^2}{k_f} K'_m(k_f \rho_f) & -\frac{\beta m}{k_f^2 \rho_f} K_m(k_f \rho_f) \\ 0 & K_m(k_f \rho_f) \\ -\frac{\beta m}{k_f^2 \rho_f} K_m(k_f \rho_f) & -\frac{ik_0}{k_f} K'_m(k_f \rho_f) \end{pmatrix} \begin{pmatrix} B_{1f} \\ B_{2f} \end{pmatrix} \\ &= \hat{\Omega}_f \begin{pmatrix} B_{1f} \\ B_{2f} \end{pmatrix}. \end{aligned} \quad (3.48)$$

The field at the outside edge of the fibre may also be found by applying the appropriate transfer matrix,  $\hat{M}$  to the field at the edge of the core. Using Equation 3.39 with  $\rho_0 = \rho_c$  and  $\rho = \rho_f$  and Equations 3.47 and 3.48 for the fields at the edge of the core and the edge of the fibre we have:

$$\begin{aligned} \hat{M} \times \hat{\Omega}_c \begin{pmatrix} A_{1c} \\ A_{2c} \end{pmatrix} - \hat{\Omega}_f \begin{pmatrix} B_{1f} \\ B_{2f} \end{pmatrix} &= \begin{pmatrix} 0 \\ 0 \end{pmatrix} \\ \left( \hat{M} \times \hat{\Omega}_c | - \hat{\Omega}_f \right) \begin{pmatrix} A_{1c} \\ A_{2c} \\ B_{1f} \\ B_{2f} \end{pmatrix} &= \begin{pmatrix} 0 \\ 0 \\ 0 \\ 0 \end{pmatrix} \end{aligned} \quad (3.49)$$

where  $(\hat{M} \times \hat{\Omega}_c | - \hat{\Omega}_f)$  is a  $4 \times 4$  matrix where the first two columns are given by  $\hat{M} \times \hat{\Omega}_c$  and the second two columns are given by  $-\hat{\Omega}_f$ . Equation 3.49 has non-zero solutions for  $A_{1c}$ ,  $A_{2c}$ ,  $B_{1f}$  and  $B_{2f}$  when the determinant of  $(\hat{M} \times \hat{\Omega}_c | - \hat{\Omega}_f)$  is equal to zero.

Modes of the multilayer fibre can be found numerically by initially specifying the physical parameters of the structure under consideration, allowing the frequency to vary and searching for the roots of the determinant. The coefficients  $A_{1c}$ ,  $A_{2c}$ ,  $B_{1f}$  and  $B_{2f}$  can then be found for the given frequency by solving the simultaneous equations in Equation 3.49.

## 3.4 Cylindrical structures with metallic features

### 3.4.1 Cylindrical surface plasmon-polaritons

Surface plasmon-polaritons can exist at cylindrical metal/dielectric interfaces as well as in planar structures. A study of SPPs occurring on the outside of a solid metal cylinder including derivation of the dispersion relations was carried out by Pfeiffer *et al.* in 1974 [97]. Schröter and Dereux studied SPPs in a thin cylindrical tube noting that there are two surface plasmon branches relating to symmetric and antisymmetric plasma distribution between the inner and outer metal/dielectric interfaces. [98]. The dispersion relation for SPPs on the inside of an essentially infinite metal tube is simple to find (e.g. [99]) and it is instructive to look at that case here.

Consider a structure consisting of a metal tube of radius  $\rho_m$  and relative permittivity  $\varepsilon_m$  filled with a dielectric material of permittivity  $\varepsilon$ . The axial component of the electric field of a TM mode in the dielectric has the form:

$$E_z = AI_0(\alpha\rho) \exp [i(\beta z - \omega t)] \quad (3.50)$$

where the modified Bessel function has been chosen to ensure that the field is finite on the axis,  $\alpha = (\beta^2 - \varepsilon\omega^2/c^2)^{1/2}$  where  $\beta$  is the propagation constant and  $A$  is a constant. The  $cB_\phi$  field component is given by:

$$\begin{aligned} cB_\phi &= -\frac{1}{\alpha^2} \frac{i\omega\varepsilon}{c} \frac{\partial E_z}{\partial \rho} \\ &= -A \frac{i\omega\varepsilon}{\alpha c} I_0'(\alpha\rho) \exp [i(\beta z - \omega t)]. \end{aligned} \quad (3.51)$$

In the metal the field has the form:

$$E_z = DK_0(\gamma\rho) \exp [i(\beta z - \omega t)] \quad (3.52)$$

$$cB_\phi = -D \frac{i\omega\varepsilon_m}{\gamma c} K_0'(\gamma\rho) \exp [i(\beta z - \omega t)] \quad (3.53)$$

where the modified Bessel function describes decay into the metal,  $\gamma = (\beta^2 - \varepsilon_m\omega^2/c^2)^{1/2}$  and  $D$  is a constant. Continuity of the tangential fields at  $\rho = \rho_m$

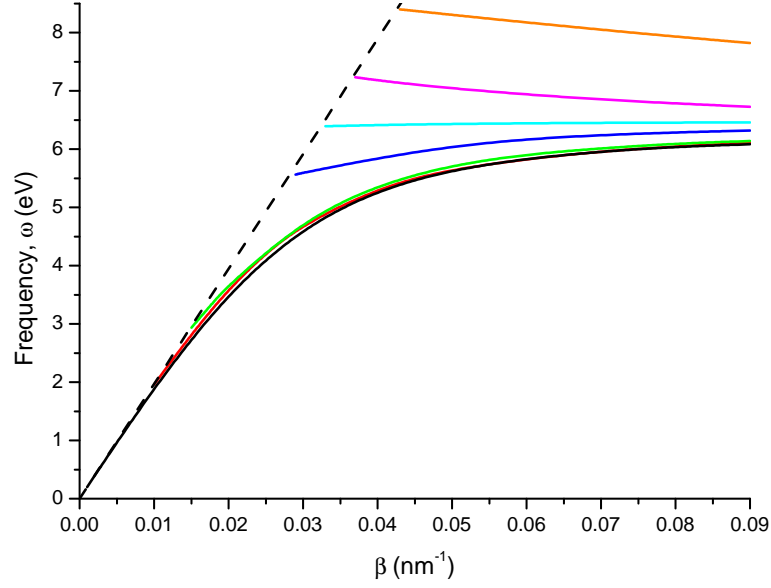


Figure 3.11: Dispersion curves for cylindrical surface plasmons on the inside of gold tubes ( $\omega_p = 8.9$  eV) with various radii and filled with air. The black line shows the dispersion curve for the similar planar system. Red indicates a tube radius of 1000 nm, green = 400 nm, blue = 80nm, cyan = 50 nm, magenta = 30 nm and orange = 10 nm. The dashed line marks the cut off at  $\omega = c\beta$ .

gives:

$$AI_0(\alpha\rho_m) = DK_0(\gamma\rho_m) \quad (3.54)$$

$$A\frac{\varepsilon}{\alpha}I'_0(\alpha\rho_m) = D\frac{\varepsilon_m}{\gamma}K'_0(\gamma\rho_m). \quad (3.55)$$

Dividing Equation 3.55 by Equation 3.54 gives:

$$\frac{\varepsilon}{\alpha} \frac{I'_0(\alpha\rho_m)}{I_0(\alpha\rho_m)} = \frac{\varepsilon_m}{\gamma} \frac{K'_0(\gamma\rho_m)}{K_0(\gamma\rho_m)} \quad (3.56)$$

which may be written in a similar form to Equation 3.10, for planar surface plasmons:

$$\frac{\varepsilon}{\varepsilon_m} = -\frac{\alpha R_K}{\gamma R_I} \quad (3.57)$$

where  $R_I = I'_0(\alpha\rho_m)/I_0(\alpha\rho_m)$  and  $R_K = -K'_0(\gamma\rho_m)/K_0(\gamma\rho_m)$ .

Figure 3.11 shows the dispersion curves for cylindrical surface plasmons on the inside of metal tubes with various radii as given by Equation 3.56. The permittivity

of the metal was modelled as  $\varepsilon_m = 1 - (\omega_p/\omega)^2$  with  $\omega_p = 8.9$  eV. The dielectric inside the metal tube was taken to be air ( $\varepsilon = 1.0$ ). The black line shows the dispersion curve for a planar system of the same materials and it can be seen that there is no cut-off value in this case. The coloured lines refer to tubes of different radii: red for 1000 nm, green for 400 nm, blue for 80nm, cyan for 50 nm, magenta for 30 nm and orange for 10 nm. The dashed line marks the cut-off at  $\omega = c\beta$ . This cut-off occurs because there are no solutions to Equation 3.56 to the left of this line. Interestingly there appears to be a change in sign of the group velocity for tubes with radii less than 50 nm. The negative slope of the dispersion curve tells us that for tube radii less than 50 nm the modes have negative group velocity whereas the positive slope of the curve for tube radii greater than 50 nm tells us that the modes have positive group velocity. For 50 nm the mode has a nearly constant frequency irrespective of  $\beta$  and hence has essentially zero group velocity.

### 3.4.2 Surface plasmon-polaritons in optical fibres

Daniel Colladon's 19th century demonstration of light being guided by a falling stream of water (Figure 3.12) was an early demonstration of total internal reflection, used in ubiquitous fibre optics today [100] facilitating global telephone calls, ethernet cabling, fibre-optic sensing, medical imaging and many other applications. The optics of step-index cylindrical optical fibres consisting of a dielectric core of high refractive index,  $n_1$  and a dielectric cladding material with lower refractive index  $n_2$  is well understood and the theory of propagating modes in such fibres may be found in many optical electronics texts, for example [101][102][103].

The inclusion of a metal core, layer or cladding in an optical fibre structure allows SPP and hybrid SPP-waveguide modes to be included in the mode spectrum of the fibre. For example the dispersion of modes in optical fibre structures with a thin metal layer between the core and cladding was investigated in 1993 by Al-Bader and Imtaar [50] while a comprehensive study of step-index fibres where the core or cladding has negative dielectric constant was carried out in 1994 by Prade and Vinet [51].

More recently there has been interest in hybrid waveguides combining the advan-

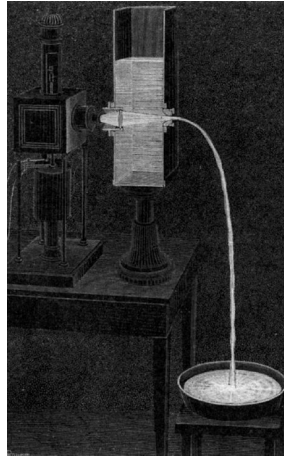


Figure 3.12: Colladon's *light fountain* demonstration, published in *La Nature*, 1884. Light focused by a lens onto an aperture in a container of water causes the light to be confined to the stream by total internal reflection.

tages of well localized surface plasmon polaritons at metal dielectric interfaces and the long propagation lengths obtainable in traditional optical fibre type structures [104][105]. Our transfer matrix method was used to reproduce an example result from the paper by Chen [105]. Chen proposed a structure composed of a metal core with refractive index  $0.1453 + 11.3587i$  surrounded by a thin layer of silica with refractive index  $n = 1.445$  and then a silicon layer with refractive index  $n = 3.455$  in air for obtaining tight confinement of light in the silica layer. This is clearly a theoretical material as the real part of the refractive index is less than unity, hence, the speed of light in the material would be greater than that of light in vacuum. Figure 3.13 shows the radial component of the electric field for the fundamental mode at a frequency of 0.7 eV in a structure consisting of a 100 nm radius metal core surrounded by a 50 nm thick layer of silica and a 200 nm thick layer of silicon. The field is discontinuous at each of the boundaries and is enhanced at the metal – silica layer boundary.

Figure 3.14 shows the dispersion relation for the fundamental mode ( $m = 1$ ) for a structure with a 200 nm core of refractive index  $n_1 = 2.37$  surrounded by a layer of refractive index  $n_2 = 1.47$  and essentially infinite metal cladding. The thickness of the  $n_2$  layer was varied and the dispersion relations are shown in the figure in different colours: the solid black line indicates zero thickness of the low

refractive index layer and the metal surrounds the 200 nm core of refractive index  $n_1$ , red corresponds to an  $n_2$  layer of thickness of 25 nm, green 50 nm, blue 100 nm, cyan 200 nm and magenta 400 nm. The dashed black line corresponds to the case of an infinite middle layer and the computations were carried out for a 200 nm core of refractive index  $n = 2.37$  surrounded by an essentially infinite cladding of refractive index  $n = 1.47$  with no metal. This particular case is a simple optical fibre structure in which, in order for the mode to be confined to the fibre, the allowed values of  $\beta$  are constrained between the values  $n_1k_0$  and  $n_2k_0$ . With the inclusion of the metal cladding the restriction on the values of  $\beta$  is removed because the light is now confined to the structure by reflection from the metal. It can be seen in the dispersion curves for structures that have the metal cladding that as the thickness of the middle, low refractive index layer is increased the dispersion curve tends to the no metal case. This is to be expected as for a very thick low refractive index layer the field will have decayed away before it reaches the metal cladding and therefore not be affected by it. The decay length in the low refractive index layer at a frequency of 0.9886 eV was calculated to be 355 nm.

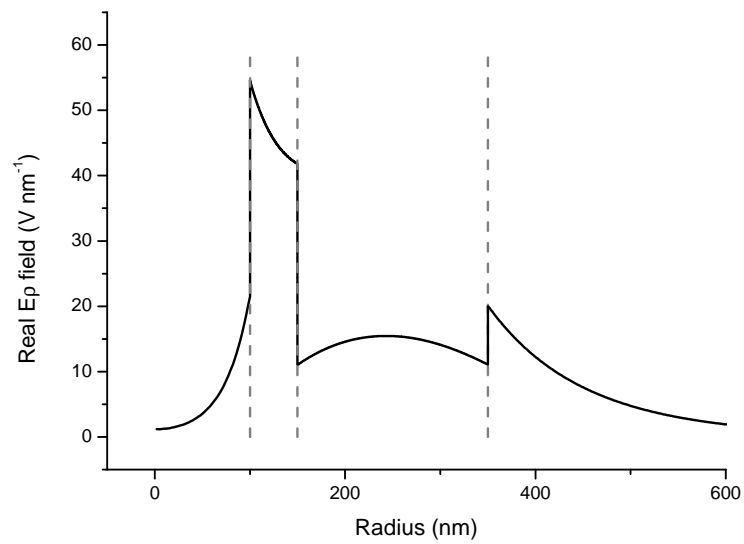


Figure 3.13: The  $E_\rho$  field component for a structure with a 100 nm radius metal core surrounded by a 50 nm thick layer of silica, a 200 nm thick layer of silicon and air. The vertical dashed lines indicate the boundary between each of the layers.

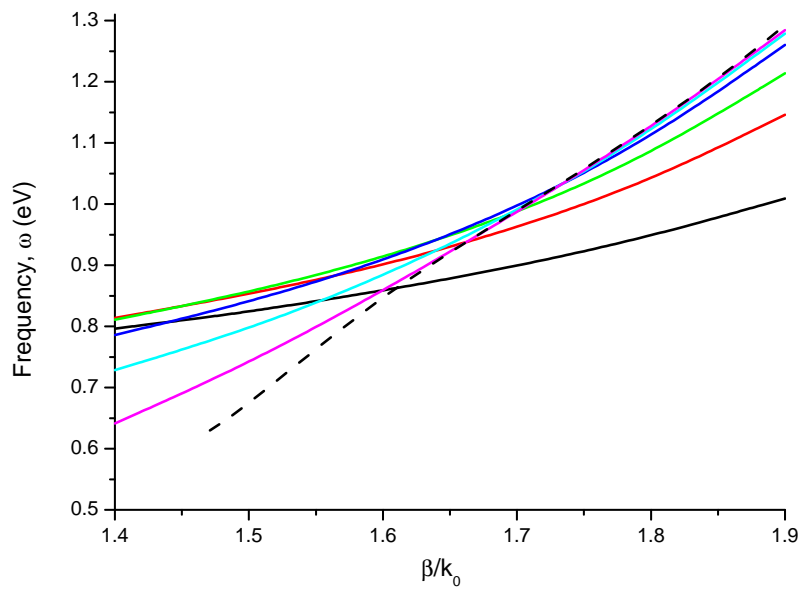


Figure 3.14: Dispersion relation for the fundamental mode in a structure with a 200 nm core of refractive index  $n = 2.37$  surrounded by a layer of refractive index  $n = 1.47$  and infinite metal cladding. Colours indicate the thickness of the middle, low refractive index layer: solid black = 0 nm (no low refractive index layer), red = 25 nm, green = 50 nm, blue = 100 nm, cyan = 200 nm and magenta = 400nm. The dashed black line is for the case with an infinite low refractive index layer and no metal.

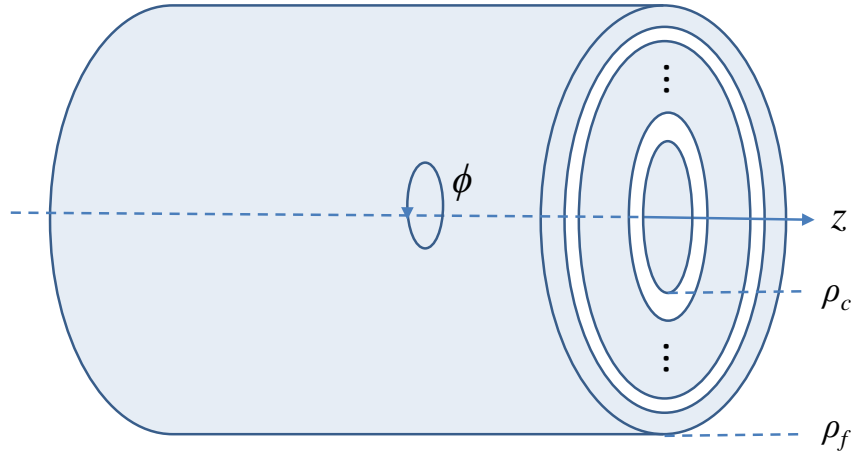


Figure 3.15: A cylindrical fibre aligned along the  $z$ -axis with a core region surrounded by layers of different refractive index, shown in blue and white. The dotted region represents repetition of the alternative refractive index layers.  $\rho_c$  and  $\rho_f$  indicate the radii of the core and the final layer of the structure respectively.

### 3.5 Multilayer cylindrical structures with metallic features

In this section the parameters of cylindrical Bragg reflector structures such as that illustrated in Figure 3.15 are discussed with a view to enabling them to support Tamm plamon-polaritons (TPPs). The required metallic element can be included in the structure as either the core or as an outer cladding or in both locations. It is of fundamental interest to study TPPs in cylindrical fibres as a natural extension to work already carried out on planar systems and simpler forms of cylindrical structures. However, the other driving force behind such a study is the prospect of devices and new technology that may come about as a result of the work. As discussed in Section 3.1 surface plasmons are already widely used in various applications and the field of plasmonics is still growing, driven by industrial, analytical

and medical applications. TPPs in planar structures have been shown to have the advantage of existing in both the TE and TM-polarisations and that they may be excited without the need for diffraction gratings or prisms. The cylindrical fibre is an obvious geometry to put forward for the task of delivering TPPs with high resolution to specific points in space or on a surface. This suggests that cylindrical TPPs may also exhibit such benefits over traditional surface plasmon-polaritons and have something to add to the field of plasmonics.

### 3.5.1 Cylindrical Bragg reflector structures

To obtain optimum reflectivity in a Bragg reflector, the reflected waves from all the dielectric interfaces should be in phase. In a planar Bragg reflector the layer thicknesses for optimum reflectivity are constant for each refractive index. However, in a cylindrical Bragg reflector, the phase of a reflected wave depends on the position (radius  $\rho$ ) of the interface and hence the optimal thickness of each layer is different and dependent on position. A numerical method for calculating the layer thicknesses for the optimum cylindrical Bragg reflector is given in [106] but this is non-trivial. Hence for the work in this thesis, for simplicity we use constant, quarter wavelength thicknesses which have been generally accepted to provide effective reflection of cylindrical waves in most circumstances [107].

### 3.5.2 Cylindrical structures for Tamm plasmon-polaritons

Following the theory set out in Section 3.2, for a TPP to exist there should be a phase difference equal to an integer multiple of  $2\pi$  or zero in a ‘round trip’ of the radiation in the dielectric layer adjacent to the metal as illustrated in Figure 3.16 for a metal core and in Figure 3.17 for metal cladding outside the structure. There are three components to the round trip phase difference: the phase change on reflection from the metal, the phase change on reflection from the Bragg reflector and the phase change of the wave on travelling from the inner to the outer radius of the dielectric layer and back again. We note that for cylindrical waves the initial and final radii are significant for calculating the phase change on propagation and not

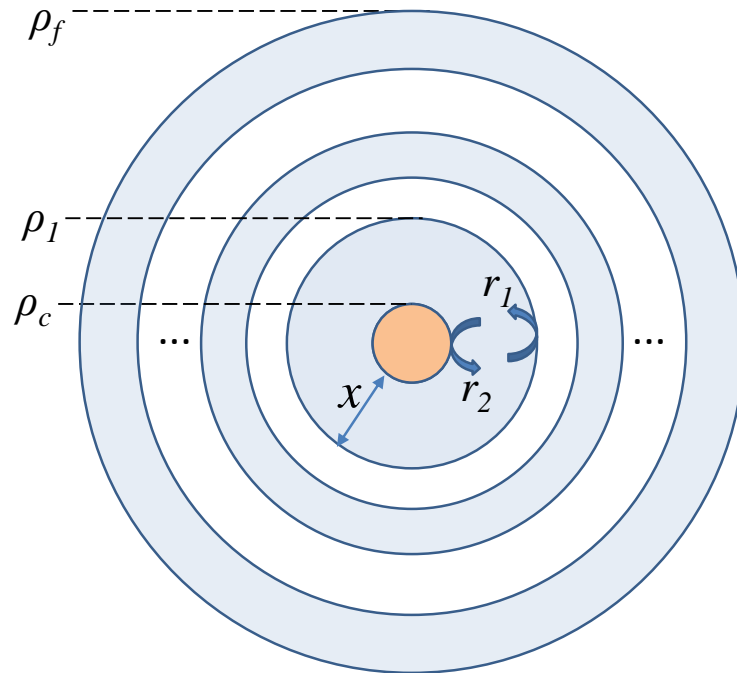


Figure 3.16: The round trip phase difference in a dielectric layer (blue) adjacent to a metal core (orange) is given by the phase change on reflection from the Bragg reflector ( $r_1$ ), the phase change on reflection from the metal ( $r_2$ ) and twice the phase change of a wave travelling across the dielectric layer marked  $x$ . The dots represent repeated layers of the Bragg reflector. Key radii are marked:  $\rho_c$  is the core radius,  $\rho_1$  is the outer radius of the first dielectric layer and  $\rho_f$  is the outer radius of the final layer of the structure.

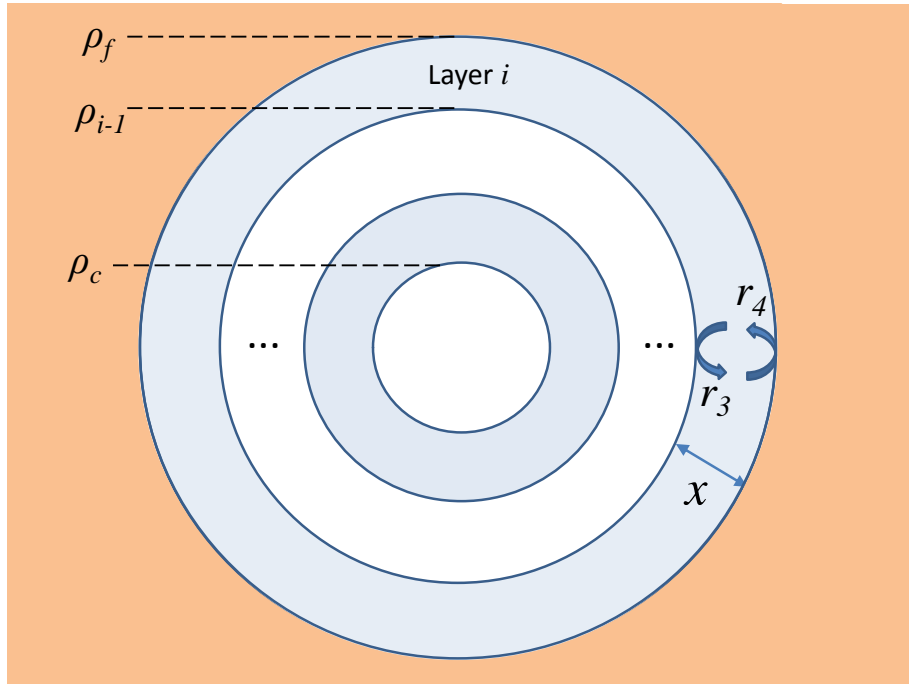


Figure 3.17: The round trip phase difference in a dielectric layer (blue) adjacent to essentially infinite metal cladding outside (orange) is given by the phase change on reflection from the Bragg reflector ( $r_3$ ), the phase change on reflection from the metal ( $r_4$ ) and twice the phase change of a wave travelling across the dielectric layer marked  $x$ . The dots represent repeating layers of the Bragg reflector.

just the layer thickness as is the case for plane waves.

### Metal core

A method for calculating the reflection coefficient from the inside of a cylindrical Bragg reflector, the reflection marked  $r_1$  in Figure 3.16, is presented in [107] for the case of TE and TM-polarised waves ( $\beta = 0$ ). The results given in that paper were used in the calculations presented here and the method was also used to obtain the reflection coefficients marked  $r_2$  in Figure 3.16 and  $r_3$  and  $r_4$  in Figure 3.17. Hence the formalism is presented here in notation consistent with this thesis.

The field components in a multilayered cylindrical structure may be written as a sum of diverging and converging waves. For the TM-mode the transverse fields of

the outgoing waves are:

$$\begin{aligned} E_z^+ &= AH_m^{(1)}(k\rho) \exp(im\phi) \\ cB_\phi^+ &= inAH_m^{(1)'}(k\rho) \exp(im\phi) \end{aligned} \quad (3.58)$$

while for the converging waves they are:

$$\begin{aligned} E_z^- &= BH_m^{(2)}(k\rho) \exp(im\phi) \\ cB_\phi^- &= inBH_m^{(2)'}(k\rho) \exp(im\phi) \end{aligned} \quad (3.59)$$

and  $k = nk_0$  as  $\beta = 0$ . Hence the total fields are written:

$$E_z = E_z^+ + E_z^- \quad (3.60)$$

$$\begin{aligned} cB_\phi &= cB_\phi^+ + cB_\phi^- \\ &= in \left[ E_z^+ \frac{H_m^{(1)'}(k\rho)}{H_m^{(1)}(k\rho)} + E_z^- \frac{H_m^{(2)'}(k\rho)}{H_m^{(2)}(k\rho)} \right]. \end{aligned} \quad (3.61)$$

Let

$$C_{mi}^{(1,2)} = \frac{H_m^{(1,2)'}(k_i\rho)}{H_m^{(1,2)}(k_i\rho)} \quad (3.62)$$

where  $i$  denotes the layer. Then we can write:

$$cB_\phi = in [E_z^+ C_m^{(1)} + E_z^- C_m^{(2)}]. \quad (3.63)$$

Now consider a diverging wave in the dielectric layer adjacent to the metal core with  $E_z$  having a value equal to unity at the outer radius of the layer  $\rho_1$ . Any converging  $E_z$  wave in layer 1 is due to the combined reflections from the many interfaces in the multilayer Bragg structure. Letting the reflection coefficient  $r_1$  describe the effective reflected field amplitude from the Bragg reflector at the outer radius of the the first layer  $\rho_1$  we can write the total fields at  $\rho_1$  as:

$$E_z(\rho_1) = 1 + r_1 \quad (3.64)$$

$$cB_\phi(\rho_1) = in_1 C_{m1}^{(1)} + in_1 C_{m1}^{(2)} r_1 \quad (3.65)$$

where  $n_1$  is the refractive index of the first dielectric layer and the  $cB_\phi$  diverging and converging components have been calculated using the formula:

$$cB_\phi = \frac{i}{k_0} \frac{\partial E_z}{\partial \rho} \quad (3.66)$$

a simplification of Equation 3.38. Outside the multilayered structure there are no converging waves and the amplitude of field component  $E_z$  is given by the transmission coefficient  $t$ :

$$E_z(\rho_f) = t \quad (3.67)$$

$$cB_\phi(\rho_f) = in_f C_{mf}^{(1)} t \quad (3.68)$$

where  $n_f$  is the refractive index outside the structure. The field amplitudes at radii,  $\rho_1$  and  $\rho_f$  are linked by the transfer matrix,  $\hat{T}$ :

$$\hat{T} \begin{pmatrix} E_z(\rho_1) \\ cB_\phi(\rho_1) \end{pmatrix} = \begin{pmatrix} E_z(\rho_f) \\ cB_\phi(\rho_f) \end{pmatrix} \quad (3.69)$$

$$\hat{T} \begin{pmatrix} 1 + r_1 \\ in_1 C_{m1}^{(1)} + in_1 C_{m1}^{(2)} r_1 \end{pmatrix} = \begin{pmatrix} t \\ in_f C_{mf}^{(1)} t \end{pmatrix}. \quad (3.70)$$

The components of the transfer matrix across a single layer of refractive index  $n$  bounded by radii  $\rho_0$  and  $\rho$  for a TM-mode are given by Equations 3.97 – 3.100 and  $\hat{T}$  is the result of multiplying the matrices for each layer from the outermost to the innermost consecutively. Multiplying out Equation 3.70 gives:

$$T_{11}(1 + r_1) + T_{12}in_1(C_{m1}^{(1)} + C_{m1}^{(2)}r_1) = t \quad (3.71)$$

$$T_{21}(1 + r_1) + T_{22}in_c(C_{m1}^{(1)} + C_{m1}^{(2)}r_1) = in_f C_{mf}^{(1)} t. \quad (3.72)$$

Substituting Equation 3.71 into Equation 3.72 gives

$$r_1 = \frac{in_f C_{mf}^{(1)} (T_{11} + in_1 C_{m1}^{(1)} T_{12}) - T_{21} - in_1 C_{m1}^{(1)} T_{22}}{T_{21} + in_1 C_{m1}^{(2)} T_{22} - in_f C_{mf}^{(1)} (T_{11} + in_1 C_{m1}^{(2)} T_{12})}. \quad (3.73)$$

For the TE-mode the same method can be followed resulting in the reflection coefficient:

$$r_1^{TE} = \frac{-\frac{i}{n_f} C_{mf}^{(1)} (T_{11}^{TE} - \frac{i}{n_1} C_{m1}^{(1)} T_{12}^{TE}) - T_{21}^{TE} + \frac{i}{n_1} C_{m1}^{(1)} T_{22}^{TE}}{T_{21}^{TE} - \frac{i}{n_1} C_{m1}^{(2)} T_{22}^{TE} + \frac{i}{n_f} C_{mf}^{(1)} (T_{11}^{TE} - \frac{i}{n_1} C_{m1}^{(2)} T_{12}^{TE})} \quad (3.74)$$

where  $T_{ij}^{TE}$  denotes the transfer matrix elements obtained by the multiplication of matrices  $\hat{T}$  with elements given by Equations 3.92 – 3.95 for consecutive layers.

Next we calculate the the reflection coefficient marked  $r_2$  in Figure 3.16, for light incident on a cylindrical metal core, with refractive index  $n_M = i\alpha$ , from a dielectric material with refractive index  $n_1$ . For the TM-mode take the total  $E_z$  and  $cB_\phi$  fields for converging and diverging waves given by Equations 3.60 and 3.63. Consider a converging wave in the first dielectric layer (refractive index  $n_1$ ) and let the  $E_z$  amplitude at the inner radius of that layer,  $\rho_c$  be unity. The reflection from the metal core at  $\rho_c$  has amplitude given by the reflection coefficient  $r_2$  hence the fields at  $\rho_c$  are given by:

$$E_z(\rho_c) = 1 + r_2 \quad (3.75)$$

$$cB_\phi(\rho_c) = in_1 \left( C_{m1}^{(2)} + C_{m1}^{(1)} r_2 \right). \quad (3.76)$$

In the metal core the fields must be decaying and also finite at the centre of the core. Therefore they may be written in terms of the modified Bessel function of the first kind,  $I_m(x)$ :

$$\begin{aligned} E_z|_{\text{core}} &= DI_m(\alpha k_0 \rho) \\ cB_\phi|_{\text{core}} &= \frac{i}{k_0} \frac{\partial E_z}{\partial \rho} \\ &= i\alpha DI'_m(\alpha k_0 \rho) \end{aligned} \quad (3.77)$$

where  $D$  is a constant. Equating the tangential field components across the core boundary,  $\rho_c$  gives:

$$\begin{aligned} 1 + r_2 &= DI_m(\alpha k_0 \rho_c) \\ in_1 \left( C_{m1}^{(2)} + C_{m1}^{(1)} r_2 \right) &= i\alpha DI'_m(\alpha k_0 \rho_c). \end{aligned} \quad (3.78)$$

Eliminating the constant  $D$  from the two equations and writing  $I'_m(\alpha k_0 \rho_c)/I_m(\alpha k_0 \rho_c) = d_m$  gives

$$r_2 = - \left( \frac{1 - (n_1 C_{m1}^{(2)}/\alpha d_m)}{1 - (n_1 C_{m1}^{(1)}/\alpha d_m)} \right). \quad (3.79)$$

The similar argument for the TE-polarisation gives

$$r_2^{TE} = - \left( \frac{1 + (\alpha C_{m1}^{(2)}/n_1 d_m)}{1 + (\alpha C_{m1}^{(1)}/n_1 d_m)} \right). \quad (3.80)$$

The final contribution to the phase change for a round trip of radiation in a dielectric layer is due to the phase change of the Hankel function describing the cylindrical wave at different radii and can be calculated directly.

## Metal cladding

The reflection coefficient marked  $r_3$  in Figure 3.17, for light incident on the outside of a cylindrical Bragg reflector from dielectric layer  $i$ , may be calculated using the same method as the previous cases. In this case, for the TM mode, we take the  $E_z$  field amplitude at the inner radius of the  $i^{\text{th}}$  layer to be unity and the fields at  $\rho_{i-1}$  can be written:

$$E_z(\rho_{i-1}) = 1 + r_3 \quad (3.81)$$

$$cB_\phi(\rho_{i-1}) = in_i \left( C_{mi}^{(2)} + C_{mi}^{(1)} r_3 \right). \quad (3.82)$$

Recalling that the field in the core of the Bragg reflector should take the form of a Bessel function of the first kind to ensure a finite field at the origin, for the TM-mode we have:

$$r_3 = \frac{in_f C_{mf}^{(2)} P - Q}{Q - in_f C_{mf}^{(1)} P} \quad (3.83)$$

where  $P = T_{11}J_m(k_c\rho_c) + T_{12}in_c J'_m(k_c\rho_c)$ ,  $Q = T_{21}J_m(k_c\rho_c) + T_{22}in_c J'_m(k_c\rho_c)$  and the transfer matrix elements have been calculated to describe the field as it evolves from core to exterior. The magnitude of the reflection coefficient,  $r_3$  is unity for all frequencies. Given that  $k$  is real in the outermost dielectric layer, it can be seen from Equation set 3.100 that  $T_{11}$  and  $T_{22}$  are real while  $T_{21}$  and  $T_{12}$  are imaginary. This means that the constant  $P$  is real and  $Q$  is imaginary. Writing  $Q$  as  $iQ_{\text{mag}}$  where  $Q_{\text{mag}}$  is the magnitude of  $Q$  and recognising that  $C_{mf}^{(1)} = a + ib$  and  $C_{mf}^{(2)} = a - ib$  are complex conjugates of each other we have:

$$r_3 = -\frac{Q_{\text{mag}} - n_f a P + in_f b P}{Q_{\text{mag}} - n_f a P - in_f b P} \quad (3.84)$$

which clearly has unit magnitude hence the only difference in the reflection coefficient with changing frequency will be in the phase.

For the TE-polarisation we have:

$$r_3^{TE} = -\frac{q + (iC_{mf}^{(2)}p)/n_f}{q + (iC_{mf}^{(1)}p)/n_f} \quad (3.85)$$

where  $p = T_{11}J_m(k_c\rho_c) - T_{12}iJ'_m(k_c\rho_c)/n_f$  and  $q = T_{21}J_m(k_c\rho_c) - T_{22}iJ'_m(k_c\rho_c)/n_f$ .

For a Bragg reflector structure with metal cladding on the outside the reflection coefficient  $r_4$  in Figure 3.17 may be calculated using a similar method to that presented in [107]. Again, ignoring losses, the magnitude of the reflection coefficient is unity and we are interested in the phase. For the TM-mode let the amplitude of the diverging  $E_z$  wave at the outside edge of the Bragg reflector,  $\rho_f$  be unity and the amplitude of the  $E_z$  wave reflected from the metal is given by  $r_4$ . Hence we have:

$$E_z(\rho_f) = 1 + r_4 \quad (3.86)$$

$$cB_\phi(\rho_f) = in_i \left( C_{mi}^{(1)} + C_{mi}^{(2)} r_4 \right). \quad (3.87)$$

Recognising that the field in the metal outside the structure must be decaying we have:

$$\begin{aligned} E_z|_{\text{outside}} &= DK_m(\alpha k_0 \rho) \\ cB_\phi|_{\text{outside}} &= i\alpha DK'_m(\alpha k_0 \rho). \end{aligned} \quad (3.88)$$

Again we match the tangential field components across the boundary to obtain the reflection coefficient and writing  $K'_m(\alpha k_0 \rho_f)/K_m(\alpha k_0 \rho_f) = g_m$  we have:

$$r_4 = - \left( \frac{1 - \left( n_i C_{mi}^{(1)} / \alpha g_m \right)}{1 - \left( n_i C_{mi}^{(2)} / \alpha g_m \right)} \right). \quad (3.89)$$

Similarly for the TE-mode we have:

$$r_4^{TE} = - \left( \frac{1 - \left( \alpha C_{mi}^{(1)} / n_i g_m \right)}{1 - \left( \alpha C_{mi}^{(2)} / n_i g_m \right)} \right). \quad (3.90)$$

The phase change of the wave on propagation across the the  $i^{\text{th}}$  layer is calculated in the same way as detailed for the case of a metal core.

### 3.5.3 A simplification of the transfer matrix problem

As described in Section 3.3.1 the modes of a multilayer fibre may be found by solving Equation 3.49. For the special cases of either the azimuthal number,  $m = 0$  or the propagation constant,  $\beta = 0$  the  $4 \times 4$  matrix reduces to two more easily solvable  $2 \times 2$  matrix problems. It can be seen in Equation set 3.32 that the field components

$E_\phi$ ,  $E_\rho$ ,  $cB_\phi$  and  $cB_\rho$  each depend on both  $E_z$  and  $cB_z$ . Setting  $m = 0$  or  $\beta = 0$  decouples the equations in set 3.32. The case  $\beta = 0$  corresponds to no propagation of the mode along the fibre axis and we have two distinct modes: that with  $E_\phi$  and  $E_\rho$  dependent only on  $cB_z$  and only these three components non-zero (the TE-mode) or that with  $cB_\phi$  and  $cB_\rho$  dependent only on  $E_z$  (the TM-mode). Similarly for the case  $m = 0$  the components  $E_\phi$  and  $cB_\rho$  depend only on  $cB_z$  and  $E_\rho$  and  $cB_\phi$  depend only on  $E_z$ . This means for  $m = 0$  there are modes with only  $E_\phi$ ,  $cB_\rho$  and  $cB_z$  non-zero (a TE-like mode) or only  $E_\rho$ ,  $cB_\phi$  and  $cE_z$  non-zero (a TM-like mode).

The  $2 \times 2$  transfer matrix,  $\hat{T}$  for a TE-mode ( $\beta = 0$ ,  $m \neq 0$ ) in a cylindrical layered structure is defined by:

$$\begin{pmatrix} cB_z(\rho) \\ E_\phi(\rho) \end{pmatrix} = \hat{T} \begin{pmatrix} cB_z(\rho_0) \\ E_\phi(\rho_0) \end{pmatrix} \quad (3.91)$$

and has the matrix elements:

$$T_{11} = k\rho_0 \frac{\pi}{2} \left[ N'_m(k\rho_0)J_m(k\rho) - J'_m(k\rho_0)N_m(k\rho) \right] \quad (3.92)$$

$$T_{21} = -ik_0\rho_0 \frac{\pi}{2} \left[ N'_m(k\rho_0)J'_m(k\rho) - J'_m(k\rho_0)N'_m(k\rho) \right] \quad (3.93)$$

$$T_{12} = -in^2k_0\rho_0 \frac{\pi}{2} \left[ N_m(k\rho_0)J_m(k\rho) - J_m(k\rho_0)N_m(k\rho) \right] \quad (3.94)$$

$$T_{22} = k\rho_0 \frac{\pi}{2} \left[ N'_m(k\rho)J_m(k\rho_0) - J'_m(k\rho)N_m(k\rho_0) \right] \quad (3.95)$$

where the radial wavevector has reduced to  $k = nk_0$  with  $k_0 = \omega/c$ . Comparison with the complete  $4 \times 4$  transfer matrix shows that the TE-polarisation is represented in the lower block diagonal of the complete matrix  $\hat{M}$ .

Similarly the transfer matrix,  $\hat{T}$  for a TM-mode in a cylindrical layered structure is defined by:

$$\begin{pmatrix} E_z(\rho) \\ cB_\phi(\rho) \end{pmatrix} = \hat{T} \begin{pmatrix} E_z(\rho_0) \\ cB_\phi(\rho_0) \end{pmatrix} \quad (3.96)$$

with matrix elements corresponding to the upper block diagonal of  $\hat{M}$ :

$$T_{11} = k\rho_0 \frac{\pi}{2} \left[ N'_m(k\rho_0)J_m(k\rho) - J'_m(k\rho_0)N_m(k\rho) \right] \quad (3.97)$$

$$T_{21} = ink\rho_0 \frac{\pi}{2} \left[ N'_m(k\rho_0)J'_m(k\rho) - J'_m(k\rho_0)N'_m(k\rho) \right] \quad (3.98)$$

$$T_{12} = ik_0\rho_0 \frac{\pi}{2} \left[ N_m(k\rho_0)J_m(k\rho) - J_m(k\rho_0)N_m(k\rho) \right] \quad (3.99)$$

$$T_{22} = k\rho_0 \frac{\pi}{2} \left[ N'_m(k\rho)J_m(k\rho_0) - J'_m(k\rho)N_m(k\rho_0) \right]. \quad (3.100)$$

For the TE-like and TM-like modes with  $m = 0$ ,  $\beta \neq 0$ , the form of Equations 3.91 and 3.96 is still valid as it is only the  $\rho$  field component that changes for  $m = 0$  or  $\beta = 0$ . However, the transfer matrices  $\hat{T}$  are different and are given, for the TE-like mode by:

$$T_{11} = k\rho_0 \frac{\pi}{2} \left[ N'_0(k\rho_0)J_0(k\rho) - J'_0(k\rho_0)N_0(k\rho) \right] \quad (3.101)$$

$$T_{21} = ik_0\rho_0 n^2 \frac{\pi}{2} \left[ N'_0(k\rho_0)J'_0(k\rho) - J'_0(k\rho_0)N'_0(k\rho) \right] \quad (3.102)$$

$$T_{12} = \frac{ik^2\rho_0}{k_0 n^2} \frac{\pi}{2} \left[ N_0(k\rho_0)J_0(k\rho) - J_0(k\rho_0)N_0(k\rho) \right] \quad (3.103)$$

$$T_{22} = k\rho_0 \frac{\pi}{2} \left[ N'_0(k\rho)J_0(k\rho_0) - J'_0(k\rho)N_0(k\rho_0) \right] \quad (3.104)$$

and for the TM-like mode by:

$$T_{11} = k\rho_0 \frac{\pi}{2} \left[ N'_0(k\rho_0)J_0(k\rho) - J'_0(k\rho_0)N_0(k\rho) \right] \quad (3.105)$$

$$T_{21} = -ik_0\rho_0 \frac{\pi}{2} \left[ N'_0(k\rho_0)J'_0(k\rho) - J'_0(k\rho_0)N'_0(k\rho) \right] \quad (3.106)$$

$$T_{12} = \frac{-ik^2\rho_0}{k_0} \frac{\pi}{2} \left[ N_0(k\rho_0)J_0(k\rho) - J_0(k\rho_0)N_0(k\rho) \right] \quad (3.107)$$

$$T_{22} = k\rho_0 \frac{\pi}{2} \left[ N'_0(k\rho)J_0(k\rho_0) - J'_0(k\rho)N_0(k\rho_0) \right] \quad (3.108)$$

where the radial wavevector  $k$  depends on  $\beta$ .

For the general case where  $m \neq 0$  and  $\beta \neq 0$  there is no decoupling of the fields which results in hybrid modes containing all six field components. These modes may be envisaged as *skew* rays in the ray picture that spiral about the axis as they propagate along the length of the fibre mixing the TE and TM components [101][108].

## 3.6 Results

In this section the results of numerical calculations of the electromagnetic fields in cylindrical multilayer structures, using the transfer matrix method introduced in Section 3.3.1, are presented. The purpose of this work was to ascertain the structural parameters required to support cylindrical Tamm plasmon-polaritons. The results given are for an example structure with dielectric layers of titanium dioxide,  $\text{TiO}_2$  ( $n = 2.37$ ) and silica,  $\text{SiO}_2$  ( $n = 1.47$ ). The refractive index values were taken from Lee *et al.* [109] and are appropriate for a free space wavelength of 900 nm but don't change too quickly for longer wavelengths. These materials were chosen because they allow for a large refractive index contrast ratio. The electronic band gap of  $\text{TiO}_2$  is around 3.8 eV [110] and for  $\text{SiO}_2$  it is 8.9 eV [111], these are both high compared to the energy corresponding to optical wavelengths: typical optical fibres carry wavelengths around 1550 nm which is equivalent to approximately 0.7 eV. This means that  $\text{TiO}_2$  and  $\text{SiO}_2$  will absorb very little in the frequency range we are interested in and so treating them as lossless materials is a reasonable approximation.  $\text{TiO}_2$  and  $\text{SiO}_2$  are both common, robust materials that would be unlikely to suffer great degradation over time were they to be used in devices. The metal considered was gold ( $\omega_p = 8.9$  eV) as this is commonly used in optoelectronic devices.

### 3.6.1 Bragg reflector

We consider a cylindrical multilayer structure with a titanium dioxide,  $\text{TiO}_2$ , core, taken to have refractive index  $n = 2.37$ . The core is surrounded by 8 pairs of layers, alternately silica,  $\text{SiO}_2$ , with refractive index  $n = 1.47$  and  $\text{TiO}_2$ . The optical thickness of each layer is a quarter wavelength; for a free space wavelength of 1240 nm this gives layer thicknesses of 211 nm and 131 nm for the  $\text{SiO}_2$  and  $\text{TiO}_2$  respectively. An infinite, planar structure with these parameters would have its photonic stop band centred at 1 eV.

The reflection coefficient of an outgoing wave in the core with  $m = 0$ ,  $\beta = 0$ , taken at the core boundary, may be calculated using Equation 3.73 for a TM mode and Equation 3.74 for a TE mode. For the case where there is no metal included

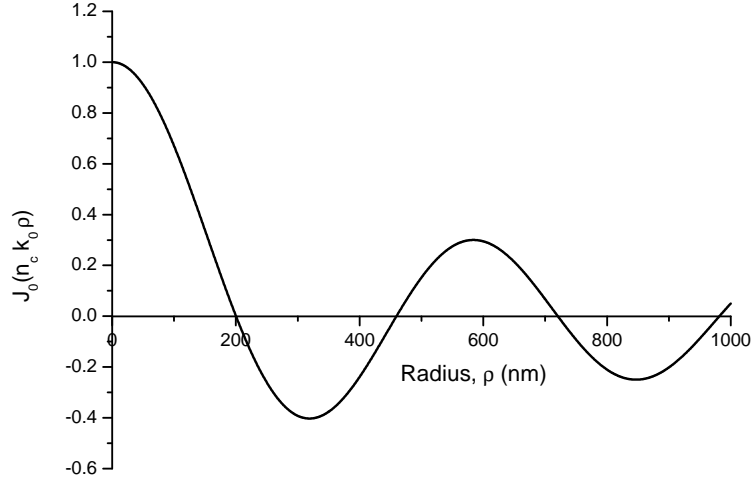


Figure 3.18: Bessel function of the first kind in a medium of refractive index  $n = 2.37$  with frequency 1.0 eV. The first node occurs at a radius 200 nm.

in the structure, we take  $n_1$  to be the refractive index of the dielectric core. For a TM mode to exist in the core there should be a non-zero  $E_z$  field at the core boundary. We require that the electric field component tangential to the boundary should have a phase change of zero on reflection so that its reflection coefficient is +1 and the outgoing and incoming waves add together to give an antinode in the field at the boundary. On the other hand, for a TE mode to exist in the core, the  $E_\phi$  field component should have an antinode at the core boundary. In the homogeneous core medium, an antinode in the  $E_\phi$  field component corresponds to a node in the  $cB_z$  field component. Figure 3.18 shows that for  $m = 0$ ,  $\beta = 0$  the Bessel function of the first kind has a node at around 200 nm. Using this core radius a TE mode was found to exist at a frequency of  $0.9792 - 1 \times 10^{-9}i$  eV. The fields for this mode can be seen in Figure 3.19 a): the black line shows the  $E_\phi$  field component while the red line shows the  $cB_z$  field component. The vertical dashed lines indicate the edge of each layer in the structure. It can be seen that there is a node in the  $cB_z$  field at 200 nm. We note that the  $E_\phi$  field component varies smoothly across all of the interfaces while the  $cB_z$  field component, though continuous in value, has a discontinuous gradient at each interface. This is consistent with the second equation

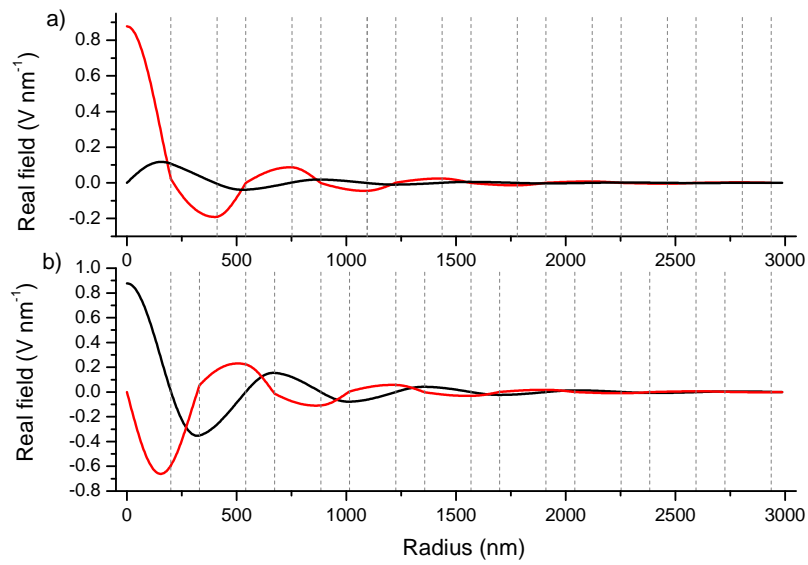


Figure 3.19: a) TE mode: the  $E_\phi$  (black line) and  $cB_z$  (red line) fields for a BR structure with  $\text{TiO}_2$  core with radius 200 nm surrounded by 8 pairs of  $\text{SiO}_2/\text{TiO}_2$  layers at a frequency 0.9792 eV. b) TM mode: the  $E_z$  (black line) and  $cB_\phi$  (red line) fields for a BR structure with  $\text{TiO}_2$  core with radius 200 nm surrounded by 8 pairs of  $\text{TiO}_2/\text{SiO}_2$  layers at a frequency 0.9942 eV.

in the set 3.32; when  $m = 0$  and  $\beta = 0$  it may be rearranged to give:

$$\frac{\partial cB_z}{\partial \rho} = in^2 E_\phi \quad (3.109)$$

and as  $n$  is discontinuous across the boundary so also is  $\partial cB_z/\partial \rho$ . Figure 3.19 b) shows the  $E_z$  (black) and  $cB_\phi$  (red) fields for a TM mode in a structure also with a  $\text{TiO}_2$  core of radius 200 nm. However, in this case the layers of the Bragg reflector structure have been reversed:  $\text{TiO}_2/\text{SiO}_2$  in order to accommodate the mode. The mode frequency is  $0.9942 - 1 \times 10^{-9}i$  eV. Just as in the planar case, as discussed in Section 3.2.2, reversing the order of the Bragg reflector layers changes the phase change on reflection from the core boundary to  $\pi$  and means that the mode with a node in the  $E_z$  component is supported.

In both the TE and the TM cases, the modes can be seen to decay essentially to zero through the layers of the Bragg reflector. This and the very small imaginary component of the frequencies shows that the Bragg reflector is sufficiently opaque that there is very little radiative loss through a structure with 8 pairs of layers (or more). It is therefore reasonable to neglect the imaginary component of the frequency in most calculations. Figure 3.20 shows the magnitude and phase of the reflection coefficient for the  $\text{SiO}_2/\text{TiO}_2$  structure whose fields are illustrated in Figure 3.19 a). Note that the TE mode frequency of 0.9892 eV sits comfortably within the photonic stop band that is apparent in the magnitude of the reflection spectrum as a wide plateau region with reflection coefficient of magnitude close to unity. The photonic band gap is centred around the Bragg frequency,  $\omega_0 = 1$  eV and has width,  $\Delta\omega = 0.3773$  eV. However, as shown previously in Figure 3.4 the band width and quality of the band gap depends on the number of layers in the Bragg reflector structure. The width of the photonic band gap in an infinite planar Bragg reflector may be approximated by the formula [93]:

$$\Delta\omega \approx \omega_0 \frac{4 |n_1 - n_2|}{\pi (n_1 + n_2)}. \quad (3.110)$$

Using this approximation, a planar Bragg reflector structure with  $\text{SiO}_2$  and  $\text{TiO}_2$  layers of refractive index  $n = 1.47$  and  $n = 2.37$  respectively with its band gap centred around  $\omega_0 = 1$  eV would have a band width  $\Delta\omega = 0.2984$  eV. Increasing the number of layers in a cylindrical Bragg reflector with quarter wavelength thickness

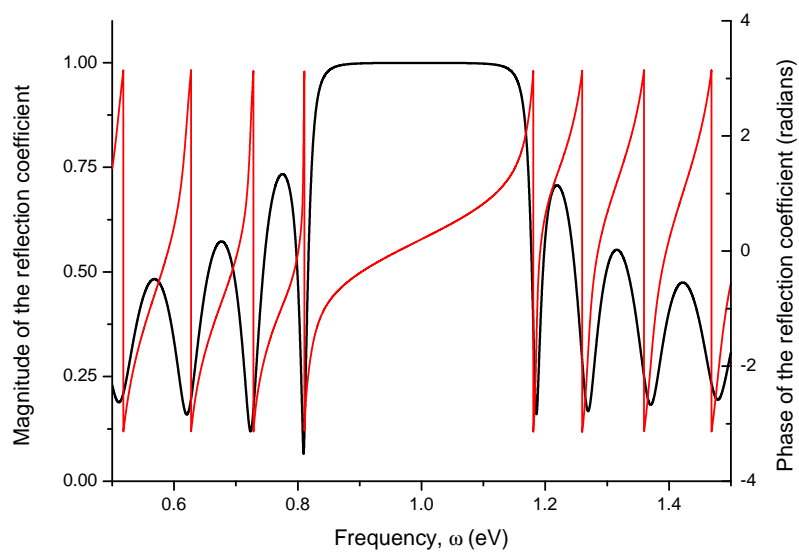


Figure 3.20: The reflection spectrum (black, magnitude and red, phase) for a cylindrical DBR with a core refractive index  $n_c = 2.37$  and 8 pairs of surrounding layers with refractive indices  $n_1 = 1.47$  and  $n_2 = 2.37$ . The thicknesses of each layer of the DBR were chosen to be  $\lambda/4$  giving effective reflection, and centring the photonic stop band, at a frequency of 1.0 eV.

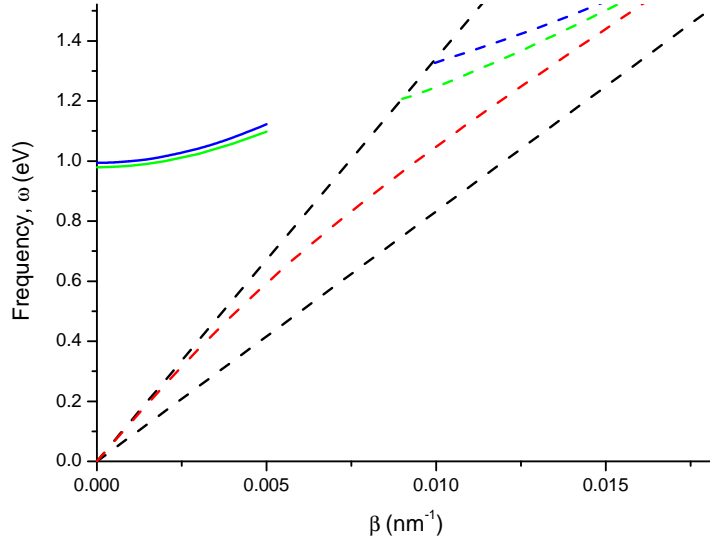


Figure 3.21: Solid lines represent the dispersion curves for a TE (green) and TM (blue) mode whose field profiles for  $\beta = 0$  are shown in Figure 3.19. For comparison, the dispersion curves of modes in a simple optical fibre structure with a  $\text{TiO}_2$  core ( $n = 2.37$ ) and  $\text{SiO}_2$  ( $n = 1.47$ ) cladding are shown as dashed lines: TE,  $m = 0$  mode (green) and TM  $m = 0$  (blue). All confined modes in this simple optical fibre have dispersion curves that lie between the dashed black lines.

layers causes the band width to tend to the value obtained for the infinite planar structure. It is clear from Equation 3.110 that the width of the band gap in a Bragg reflector will be larger the greater the difference in the refractive index of the two materials.

The solid lines in Figure 3.21 illustrate the dispersion curves for the TE (green) and TM (blue) modes for Bragg reflector structures containing no metal, whose instantaneous fields for  $\beta = 0$  are shown in Figure 3.19. The structures that support these modes have been described in the caption to Figure 3.19 and the surrounding text. The dashed black lines indicate the limits on the mode dispersion curves for any mode in a simple optical fibre structure made of the same materials ( $\text{TiO}_2$  core of refractive index 2.37 and  $\text{SiO}_2$  cladding of refractive index 1.47). For comparison, the coloured dashed lines illustrate the modes of this optical fibre with core radius 200 nm: red shows the fundamental,  $m = 1$  mode, green shows the TE,  $m = 0$  mode

and blue shows the TM,  $m = 0$  mode. The Bragg reflector mode dispersions are parabolic and lie to the left of the light cone for modes in a simple optical fibre. The range of  $\beta$  shown for the Bragg reflector structure is smaller than that shown for the simple optical fibre. This is because, for large values of  $\beta$ , the structure required for a bound mode would be different to that for the case  $\beta = 0$ . By retaining the structure that supports the  $\beta = 0$  mode the calculations fail to find solutions for large values of  $\beta$ .

### 3.6.2 Indication of modes in a Bragg reflector structure

For some cylindrical Bragg reflector structures, it appeared that there was an indication of the frequency of a mode in the core in the phase of the reflection spectrum calculated from the outside of the structure (Equations 3.83 and 3.85). Figure 3.22 shows the phase of the reflection coefficient as a function of frequency, calculated for a TM mode with  $m = 0$ , for a structure with a TiO<sub>2</sub> core surrounded by 9 pairs of SiO<sub>2</sub>/TiO<sub>2</sub> Bragg reflector layers. The feature in the phase of the reflection coefficient occurs at a frequency 0.9234 eV. There was no indication of this mode in the magnitude of the reflection coefficient which was consistently unity at and around this frequency. This is an example of a case where a change in phase is clearly visible as a signature of a state which gives no apparent change in reflection coefficient. The same phenomenon has been reported in planar Bragg reflector structures e.g. [112]. Experimentally, this could be useful in that reflection spectroscopy could be used to detect bound modes in cylindrical Bragg reflector structures.

Note that the mode indicated in Figure 3.22 is not the same TM mode, or the same structure, as that illustrated in part b of Figure 3.19. The indication of mode frequency discussed here did not appear consistently in all the calculations carried out and so this was not used, for the results presented in this thesis, as a method of finding modes.

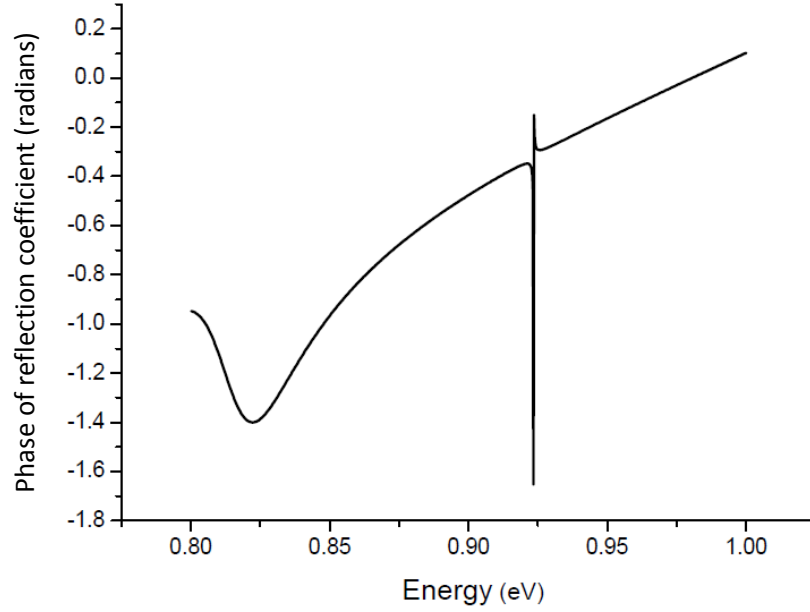


Figure 3.22: The phase of the reflection coefficient calculated from the outside of the Bragg reflector structure for a TM mode in a structure with a 150nm  $\text{TiO}_2$  core and 9 pairs of  $\text{SiO}_2/\text{TiO}_2$  layers shows a sharp feature at frequency 0.9234 eV.

### 3.6.3 Metal core

For a Tamm plasmon-polariton to exist we require an interface between a metal and a Bragg reflector structure. In Section 3.6.1 we showed that a Bragg reflector structure containing no metal and a  $\text{TiO}_2$  core supported a TE mode at a frequency of 0.9792 eV. We now investigate the changes required to the structure in order to support a mode at the same frequency when a thin metal core is included in the structure. The Bragg reflector structure with a metal core is illustrated in Figure 3.16. The core is assumed to be a lossless metal with plasma frequency  $\omega_p = 8.9$  eV and radius 30 nm. The layer adjacent to the metal is  $\text{TiO}_2$  and this is surrounded by 8 pairs of  $\text{SiO}_2/\text{TiO}_2$  layers. It is necessary to calculate the required thickness of the  $\text{TiO}_2$  layer adjacent to the metal in order to support the mode. The phase change on reflection from the Bragg reflector ( $r_1$  in Figure 3.16) varies with frequency and may be calculated from Equation 3.74 for the TE polarisation, this is shown in Figure 3.23. At the TE mode frequency for the metal free structure, 0.9792 eV, the

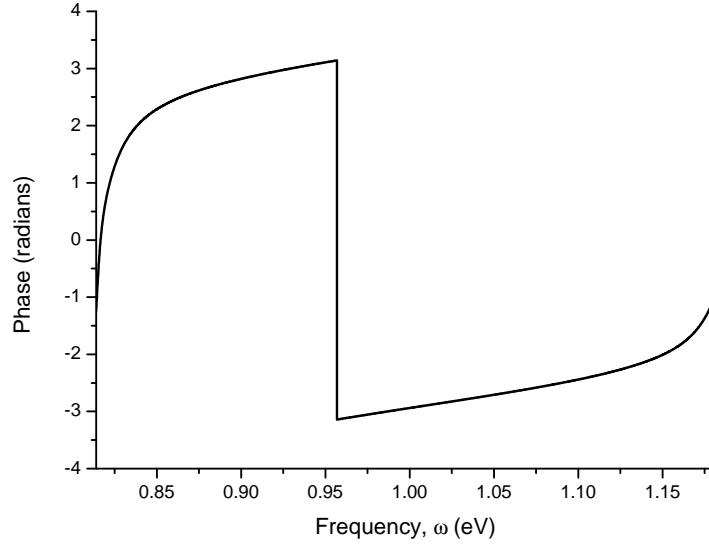


Figure 3.23: Phase of the reflection coefficient,  $r_1$ , from the inside of a Bragg reflector varying with frequency across the photonic band gap for the TE polarisation as calculated from Equation 3.74.

phase is -3.03487 radians. Equation 3.80 is used to calculate the phase change on reflection from a metal cylinder of radius 30 nm in  $\text{TiO}_2$ . At the TE mode frequency the value is -1.278510 radians. The total phase change for a round trip in the  $\text{TiO}_2$  layer surrounding the metal should be an integer multiple of  $2\pi$  or zero. The total from these two components is -4.31338 radians and therefore we require

$$\begin{aligned}
 -4.31338 + 2\Phi &= 0 \\
 \Phi &= 2.15669
 \end{aligned}
 \tag{3.111}$$

where  $\Phi$  is the necessary phase change for a wave travelling from the edge of the metal core across the  $\text{TiO}_2$  layer to the first boundary with  $\text{SiO}_2$ . By considering the ratio of the Hankel function of the first kind for argument  $k\rho$  (where  $k$  is the radial wavevector in the  $\text{TiO}_2$  layer and  $\rho$  is the radius) to the Hankel function of the first kind for argument  $k\rho_c$  where  $\rho_c$  is the radius of the metal core, the required radius to obtain a phase change of 2.15669 is calculated to be 201 nm. Hence we propose that in order to support a TPP TE mode at a frequency of 0.9792 eV the structure should consist of: a 30 nm metal core surrounded by a 201 nm thick layer of  $\text{TiO}_2$

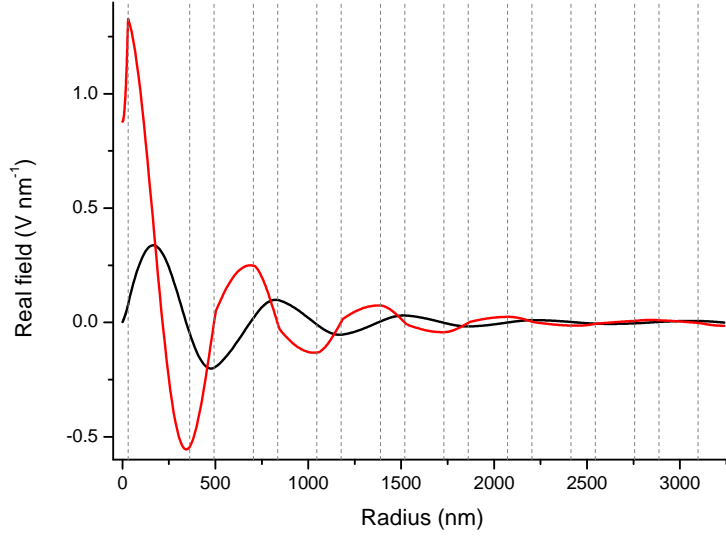


Figure 3.24: The  $E_\phi$  (black) and  $cB_z$  (red) fields components for a TE mode with  $m = 0$ ,  $\beta = 0$  in a Bragg reflector structure with a 30 nm metal core, a 201 nm thick  $\text{TiO}_2$  layer and 8 pairs of  $\text{SiO}_2/\text{TiO}_2$  layers. The vertical dashed line indicates the edge of the metal core. The mode frequency is 0.9792 eV.

followed by a Bragg reflector structure with alternating quarter wavelength thickness layers of  $\text{SiO}_2$  and  $\text{TiO}_2$ . The instantaneous  $E_\phi$  (black line) and  $cB_z$  (red line) field components for this structure can be seen in Figure 3.24. The vertical dashed lines indicate the dielectric boundaries and it is clear that the field components have the characteristic decay of a TPP state in both the metal and the Bragg reflector where the decay of the field is faster in the metal than it is in the Bragg reflector. This shows that, as for the planar case, TPPs can exist in the TE polarisation in cylindrical multilayer structures.

It is possible to tune the mode frequency of the multilayer fibre by altering the thickness of the layer adjacent to the metal. Figure 3.25 shows the instantaneous fields of a) a TM and b) a TE mode both with frequency 1 eV for the case  $m = 0$ ,  $\beta = 0$ . The structures both consist of a 30 nm metal core surrounded by a  $\text{TiO}_2$  layer and then 8 pairs of  $\text{SiO}_2/\text{TiO}_2$  Bragg reflector layers. The only difference in the structures is in the thickness of the  $\text{TiO}_2$  layer adjacent to the metal; in the case of the TM mode the thickness is 426 nm and for the TE mode, 346 nm.

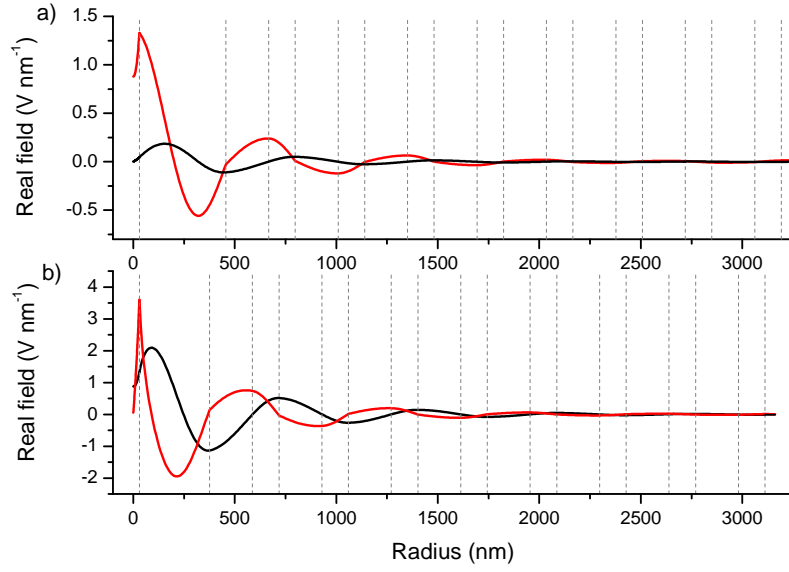


Figure 3.25: a) TE mode with  $\beta = 0$  and frequency 1 eV in a multilayer structure with a metal core of radius 30 nm and TiO<sub>2</sub> layer adjacent to the metal with thickness of 426 nm. The black line shows the  $E_\phi$  field component while the red line shows the  $cB_z$  field component. b) TM mode with  $\beta = 0$  and frequency 1 eV for the same structure but with an adjacent TiO<sub>2</sub> layer thickness of 346 nm. The black line shows the  $E_z$  field component while the red line shows the  $cB_\phi$  field component. All boundaries are marked with vertical dashed lines.

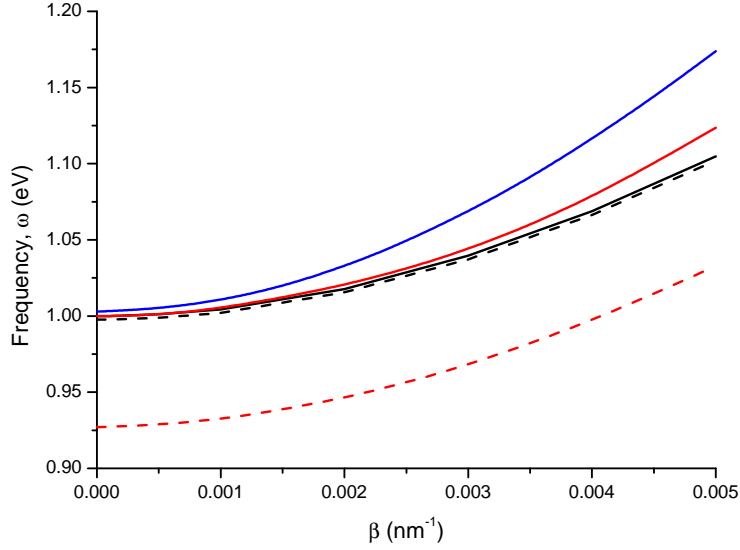


Figure 3.26: The solid lines show the dispersion curves for  $m = 0$ , TE (black) and TM (red) modes for the structures required to give a mode frequency at  $\beta = 0$  of 1 eV. The dashed lines show the dispersion curves for the same structures with the metal core removed and replaced by  $\text{TiO}_2$ .

Increasing the propagation constant  $\beta$  and finding the corresponding mode frequencies gives the dispersion curve shown in Figure 3.26. The TE mode dispersion is shown as a solid black line and the TM mode as a solid red line. The dashed curves indicate the dispersion for the same structures but with the metal core removed and replaced by  $\text{TiO}_2$  (again black for the TE and red for the TM mode). The blue solid line is the dispersion curve for a hybrid mode with  $m = 1$ ,  $\beta = 0$  in a structure consisting of a 30 nm metal core surrounded by a  $\text{SiO}_2$  cavity layer of thickness 483 nm and 8 pairs of  $\text{TiO}_2/\text{SiO}_2$  layers. The curves have been obtained using a curve fitting algorithm in OriginPro 8.1 and are found to be parabolic with adjusted  $R^2$  values greater than 0.999. This parabolic dispersion is characteristic of TPPs in the planar geometry. The effective mass  $m^*$  of the TPPs may be calculated using the relation

$$m^* = \hbar^2 \left[ \frac{d^2\omega}{d\beta^2} \right]^{-1}. \quad (3.112)$$

For the TM-polarisation the curve fit is given by  $\omega = 0.9995 + 4914.3 \beta^2$ . The

standard error on the coefficient of  $\beta^2$  is  $\pm 28.4$  which gives an effective mass of  $(1.240 \pm 0.018) \times 10^{-6} m_e$ . For the TE-polarisation the curve fit is given by  $\omega = 1.0001 + 4214.9 \beta^2$ . The standard error on the coefficient of  $\beta^2$  is  $\pm 24.0$  which gives an effective mass of  $(1.434 \pm 0.003) \times 10^{-6} m_e$ . The TE – TM splitting increases quadratically with  $\beta$  in agreement with results obtained for the planar case [41]. For  $m = 1$  the dispersion curve fit is given by  $\omega = 1.0031 + 7343.1 \beta^2$ . The standard error on the coefficient of  $\beta^2$  is  $\pm 24.3$  which gives an effective mass of  $(8.297 \pm 0.027) \times 10^{-7} m_e$ . The group velocity  $v_g$  may also be found from the dispersion curve using the relation:

$$v_g = \frac{\partial \omega}{\partial \beta} \quad (3.113)$$

The TPPs have zero group velocity at  $\beta = 0$ . At very small values of  $\beta$ , for example  $\beta = 1 \times 10^{-9} \text{ nm}^{-1}$  the group velocity for the TM mode is found to be  $9.8286 \times 10^4 \text{ ms}^{-1}$ , for the TE mode  $v_g = 8.4298 \times 10^4 \text{ ms}^{-1}$  and for the  $m = 1$  mode  $v_g = 1.4686 \times 10^4 \text{ ms}^{-1}$ . These values are several orders of magnitude lower than the speed of light in vacuum and the speed of light in  $\text{TiO}_2$  ( $1.27 \times 10^6 \text{ ms}^{-1}$ ) earning TPPs the term ‘slow light’. As the value of  $\beta$  increases, the group velocity also increases. Above  $\beta$  values of approximately  $1 \times 10^{-5} \text{ nm}^{-1}$  the light in this structure has a velocity comparable to, or greater than, the speed of light in  $\text{TiO}_2$ .

Figure 3.27 shows the instantaneous field components for the TE and TM modes that exist for  $\beta = 0$  for the same structures as the fields in Figure 3.25 but without the metal core. In each case the 30 nm metal core has been replaced by  $\text{TiO}_2$ . Comparing Figure 3.27 to Figure 3.25 it is clear that the metal has made very little difference to the field components of the TE mode. However, for the TM mode, to accommodate the metal, the field in the adjacent  $\text{TiO}_2$  layer changes significantly. There is a corresponding change in frequency of the TM mode from 0.92 eV without the metal to 1.0 eV with the metal core.

Figure 3.28 shows the variation of mode frequency with the thickness of the  $\text{TiO}_2$  layer adjacent to the metal core for  $m = 1$  and  $m = 0$  (TM and TE modes) all for  $\beta = 0$ . As discussed in Section 3.5.2 changing the thickness of a layer changes the phase accumulated in crossing it, therefore it is possible to select a particular mode frequency by picking the appropriate layer thickness.

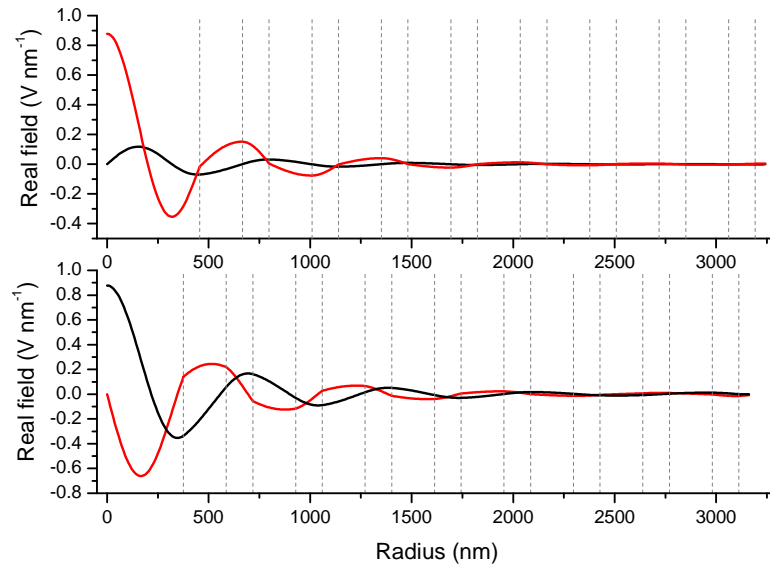


Figure 3.27: a) TE mode with  $\beta = 0$  and frequency 0.9976 eV in a multilayer structure with a TiO<sub>2</sub> core of radius 456 nm surrounded by 8 pairs of SiO<sub>2</sub>/TiO<sub>2</sub> layers. The black line shows the  $E_\phi$  field component while the red line shows the  $cB_z$  field component. b) TM mode with  $\beta = 0$  and frequency 0.9200 eV for the same structure but with a TiO<sub>2</sub> core of radius 376 nm. The black line shows the  $E_z$  field component while the red line shows the  $cB_\phi$  field component. All interfaces are marked with vertical dashed lines.

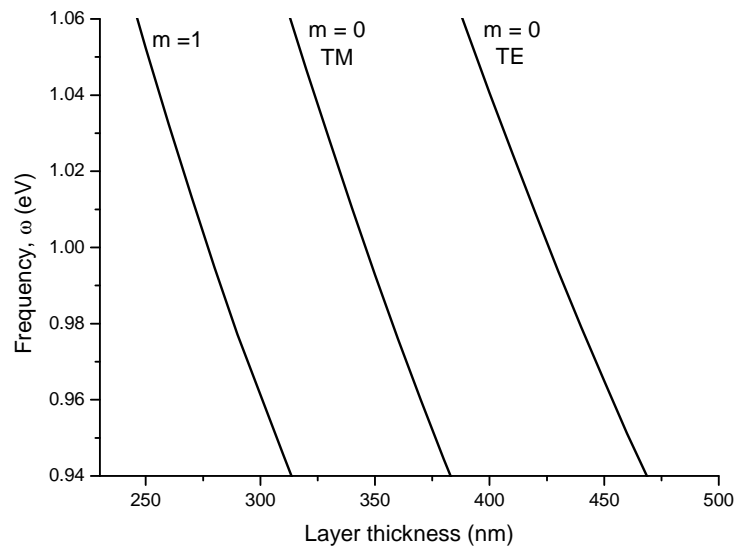


Figure 3.28: Variation of mode frequency with varying thickness of the  $\text{TiO}_2$  layer adjacent to the metal core for  $m = 0$  and  $m = 1$ .

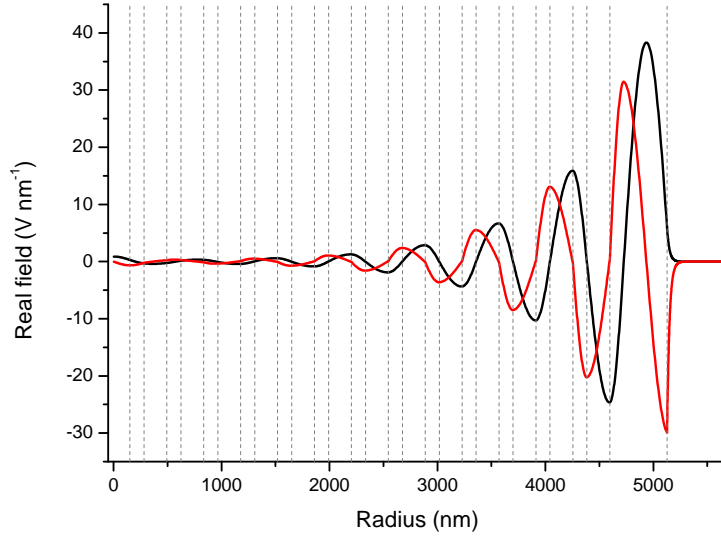


Figure 3.29: The  $E_z$  (black) and  $cB_\phi$  (red) field components of a TM mode of frequency 1.0 eV in a cylindrical structure with 150 nm  $\text{TiO}_2$  core, 14 pairs of  $\text{TiO}_2/\text{SiO}_2$  Bragg reflector layers (of thickness 131 nm and 211 nm respectively), a  $\text{SiO}_2$  cavity layer of thickness 400 nm all surrounded by essentially infinite metal.

### 3.6.4 Metal cladding

Next we consider a structure such as that illustrated in Figure 3.17, a cylindrical Bragg reflector with an infinite metal cladding around the outside. Figures 3.29 and 3.30 show the instantaneous field components of a TM and TE mode respectively, each with frequency 1 eV.

Figure 3.29 shows the instantaneous, real  $E_z$  (black) and  $cB_\phi$  (red) field components for a TM mode with  $m = 0$ ,  $\beta = 0$  and frequency 1 eV, for a structure with a  $\text{TiO}_2$  core of radius 150 nm surrounded by 14 pairs of  $\text{TiO}_2/\text{SiO}_2$  layers. The thickness of the  $\text{SiO}_2$  layers is 211 nm and the  $\text{TiO}_2$  layers have thickness 131 nm. There is a  $\text{SiO}_2$  cavity layer of thickness 400 nm surrounding the Bragg reflector structure and an essentially infinite, lossless metal with plasma frequency 8.9 eV around the outside. The radius of the core was chosen so that it would not support a mode at the centre of the structure. The thickness of the cavity layer was chosen to support a round trip phase change of  $2\pi$ . The fields can be seen to decay both

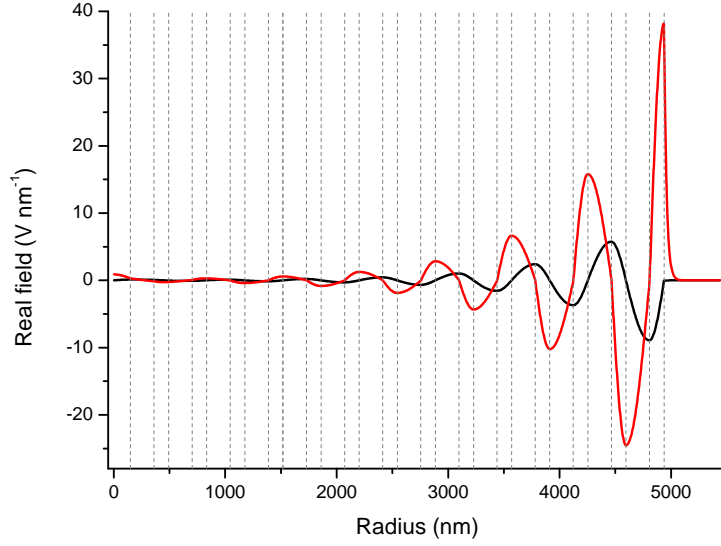


Figure 3.30: The  $cB_z$  (red) and  $E_\phi$  field components of a TE mode with frequency 1 eV and  $\beta = 0$  in a structure with a  $\text{TiO}_2$  core of radius 150 nm surrounded by 14 pairs of  $\text{SiO}_2/\text{TiO}_2$  layers, where the  $\text{SiO}_2$  layers have thickness 211 nm and the  $\text{TiO}_2$  layers have thickness 131 nm. The  $\text{TiO}_2$  cavity layer adjacent to the metal surrounding the structure has a thickness of 130 nm. Vertical dashed lines mark the dielectric boundaries.

into the metal (to the right of the final boundary line) and into the Bragg reflector (to the left of the final boundary line). We note that the field value at the centre of the core in the Bragg reflectors is not zero. This is because the field in the core has been chosen to be the  $m = 0$  Bessel function of the first kind, as it must be to avoid a divergence at the origin. The magnitude of this function at the origin is unity. However, by considering the field values at the core relative to that at the edge of the metal the field can be seen to have decayed substantially.

As another example, Figure 3.30 shows the real  $cB_z$  (red) and  $E_\phi$  (black) fields for the TE,  $m = 0$ ,  $\beta = 0$  mode at frequency 1 eV in a multilayer cylindrical structure with a  $\text{TiO}_2$  core of radius 150 nm surrounded by 14 pairs of  $\text{SiO}_2/\text{TiO}_2$  layers and a  $\text{TiO}_2$  cavity layer of thickness 130 nm all enclosed in a lossless metal with plasma frequency 8.9 eV. It can be seen that the field is greatest inside the cavity layer

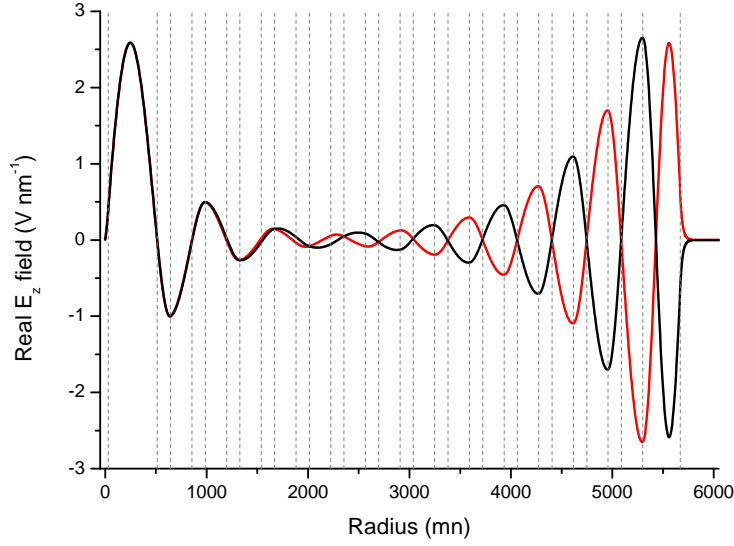


Figure 3.31: The  $E_z$  field component for two split modes, one with frequency 1.00406 eV (black line) and the other 1.00589 eV (red). Both were calculated for  $m = 1$ ,  $\beta = 0$  in a structure consisting of: a metal core of radius 30 nm; a SiO<sub>2</sub> cavity layer adjacent to the core of thickness 483 nm; 14 pairs of layers alternating TiO<sub>2</sub>/SiO<sub>2</sub> with respective thickness 131 nm/ 211 nm; a final TiO<sub>2</sub> cavity layer of thickness 370 nm adjacent to the semi-infinite metal cladding outside.

adjacent to the metal and decays very rapidly into the metal and more slowly into the Bragg reflector structure.

In both these examples the frequency at the centre of the photonic band gap of the Bragg reflector was chosen to be 1 eV and the structure was designed accordingly. Note that the order of the layers in the Bragg reflector to support a TE mode is the opposite of that required to support a TM mode.

### 3.6.5 Metal core and metal cladding

Figure 3.31 shows the instantaneous, real,  $E_z$  field components for the split modes of a coupled multilayered system with  $m = 1$  and  $\beta = 0$ . The structure has a 30 nm metal core and semi-infinite metal cladding outside. There is a SiO<sub>2</sub> cavity layer adjacent to the metal core with a thickness of 483 nm and a TiO<sub>2</sub> cavity layer

adjacent to the metal cladding with a thickness of 370 nm. The interim Bragg reflector structure has 14 pairs of alternating  $\text{TiO}_2/\text{SiO}_2$  layers of thickness 131 nm / 211 nm respectively. Close to the core this structure is the same as that considered for supporting the  $m = 1, \beta = 0$  mode for the case with metal in the core only. The fields of the two modes in Figure 3.31 can be seen to follow exactly the same pattern close to the core but progressively become out of phase in the Bragg reflector layers and are in antiphase at the outer edge. As such they represent symmetric and antisymmetric modes. The frequency splitting between the modes is just 1.83 meV or 0.44 THz.

The frequency splitting varies with the number of layers in the Bragg reflector as it depends on the overlap of the electromagnetic fields of the inner and outer modes in the Bragg reflector layers. Figure 3.32 shows the frequency difference in the dispersion curves for the two coupled modes in a structure with 10 pairs of Bragg reflector layers. The black line is the dispersion curve for the symmetric mode and the higher frequency, red line is for the antisymmetric mode. Using Equation 3.113 the group velocities of the two split modes may be calculated. They were found to be  $1.6008 \times 10^4 \text{ ms}^{-1}$  and  $1.6866 \times 10^4 \text{ ms}^{-1}$  for the symmetric and antisymmetric modes respectively. These group velocities are slightly higher than that calculated for the same mode, for the case with metal included only in the core of the structure.

### 3.7 Discussion

In this chapter it has been shown theoretically that cylindrical Bragg reflector structures are capable of supporting Tamm plasmon-polaritons by having a metal core, metal cladding around the outside of the structure or metal in both of these locations. The cylindrical TPPs can exist in both the TE and TM polarisations for the special cases  $m = 0$  or  $\beta = 0$  and can also be formed from hybrid cylindrical modes when  $m \neq 0$  and  $\beta \neq 0$ . In the case of metal both in the core and around the outside of the fibre it has been shown that two split modes can be supported with a frequency difference which, for the specific example considered here, was in the terahertz regime. If a transition between these two excitations could be induced, it

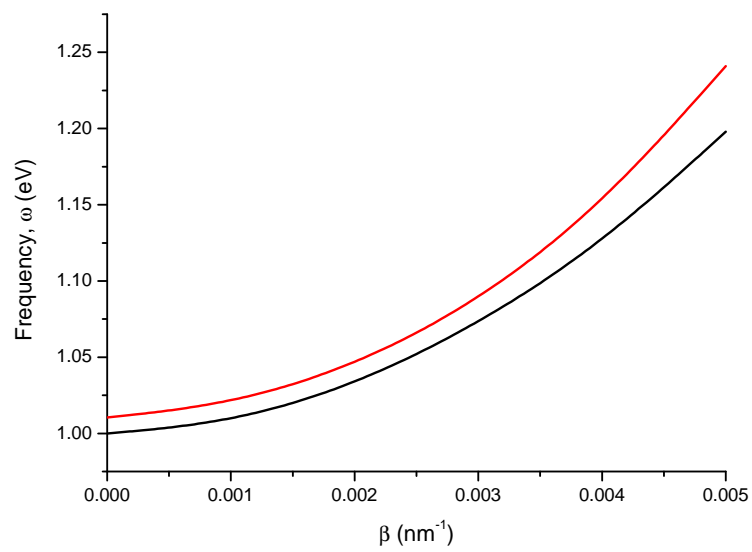


Figure 3.32: The split dispersion curves for a structure with a metal core and a metal cladding as described in Figure 3.31. The black line is the dispersion curve for the symmetric mode and the higher frequency, red line is for the antisymmetric mode. This structure has only 10 pairs of layers in the Bragg reflector rather than the 14 pairs in Figure 3.31 to enhance the splitting and hence show it more clearly.

may be possible to use this splitting as a means of emission or detection of terahertz radiation.

It has been shown that TPPs in cylindrical structures have low group velocities, as is the case for planar TPPs, earning them the term ‘slow light’. Slow light has a compressed spatial pulse length which may give a longer interaction time and an enhancement of light-matter interactions compared with light travelling at more conventional speeds [113]. Slow light has also been proposed as a useful tool in information processing [14]: some logic elements require a time delay in processing, current attempts to achieve this in photonics use long optical fibres which means that the scale of the components is necessarily large. Slow light may be a way around this.

The materials in the Bragg reflector structures considered in this chapter,  $\text{TiO}_2$  and  $\text{SiO}_2$ , were chosen due to their large refractive index contrast. Without using semiconductor materials or resorting to using refractive indices that do not correspond to real materials it would be difficult to find materials that allowed for a significantly larger contrast. As discussed in Section 3.6.1 the greater the contrast in the refractive indices of materials in a Bragg reflector, the greater the width of the photonic band gap.  $\text{SiO}_2$  and  $\text{TiO}_2$  are both common materials.  $\text{SiO}_2$  is routinely used in the fabrication of optical fibres and so the techniques for drawing  $\text{SiO}_2$  fibres are widely known. It may then be possible to evaporate or sputter further layers around the initial core fibre to produce a multilayer structure. However the accuracy required in the thickness of each layer would need to be of the order of a few nanometers and this would prove challenging using current techniques. Coating a fibre with metal could be achieved by evaporation. Producing a cylindrical structure with a metal core could perhaps be achieved by etching a hole in a cylindrical dielectric and then adding the metal or by deposition on the metal or a fibre pulling technique.

Despite the current difficulties facing the fabrication of cylindrical multilayer structures there is a lot of interest in the field of plasmonics with an emphasis on the nanoscale and it seems to the author that this will drive forwards the technologies required to make the components if useful effects can be theoretically demonstrated.

The materials have been modelled as lossless for calculational simplicity. In some cases the neglect of losses in the materials as well as leakage through the Bragg reflectors is a good approximation as extinction coefficients of less than  $10^{-6}$  are achievable. The electronic band gaps of both  $\text{SiO}_2$  and  $\text{TiO}_2$  are large enough to avoid absorption at the frequencies of interest and in Section 3.6.1 it was shown that radiative loss in the cylindrical Bragg reflector structures was small and could reasonably be ignored. Loss in the metal could be included by introducing a non-zero value for  $\Gamma$  in Equation 3.1, which would make the dielectric constant of the metal complex. Including losses in the calculations would then involve finding zeros in the determinant of the matrix in Equation 3.49 in the complex plane. Brand *et al.* [114] have shown for planar systems that there may be an indication of the TPP state if losses are included in the calculations. They showed that, for a 50 nm metal layer, a large field enhancement lead to large losses in the metal which in turn gave a large dip in the reflectivity spectrum.

Research on Tamm plasmon-polaritons has grown over the last few years and papers have been published that increase our fundamental understanding of these interface states and the structures that may support them as well as proposing applications. For example, it has been shown that optical Tamm states can exist above the bulk plasma frequency for structures designed using certain materials, for example indium tin oxide [115]. Optical Tamm states have also been shown to exist at an interface between a photonic crystal and a magnetophotonic crystal [116] or a magnetic metal [117]. The enhancement of Faraday rotation and sharp transmission peaks are suggested as useful characteristics for magnetotunable filters. Highly efficient unidirectional transmission in an all-optical diode has been demonstrated using the interface states between a one-dimensional photonic crystal structure of  $\text{SiO}_2$  and  $\text{TiO}_2$  and a thick layer of silver [45] and strong optical absorbers using TPPs at a thick metal, truncated photonic crystal interface have been proposed and demonstrated [46].

It seems that there are many potential applications for TPPs and that others may now take cylindrical TPPs forward and include these in proposals for new devices.

# Chapter 4

## Disorder in Two-Dimensional Photonic Crystals

In this chapter the effects of disorder on a 2D photonic crystal formed by a hexagonal array of air holes in a dielectric slab are considered and an attempt is made to quantify the effects of disorder in the radius of the air holes. Other work on disorder in photonic crystals is briefly reviewed.

### 4.1 Introduction

The Bragg reflector structure introduced in Section 1.2 is a type of one-dimensional photonic crystal, a structure with a periodic modulation in dielectric constant,  $\varepsilon$ . Figure 4.1 illustrates different photonic crystal structures classified as one-, two- or three-dimensional depending on how many directions in which the dielectric constant varies. Examples of such periodic structures are found to occur naturally, for example, in the gemstone opal, the wings of the Lycaenid butterfly and the cases of many tropical beetles, each of which exhibits iridescent colouring due to their internal structure. Photonic crystal structures may also be engineered using techniques such as evaporation growth or etching. An electromagnetic wave propagating through a photonic crystal is partially reflected and partially transmitted at each interface and the multiply reflected and refracted rays interfere with one another. It was first shown by Lord Rayleigh in 1888, for one-dimensional periodic structures,

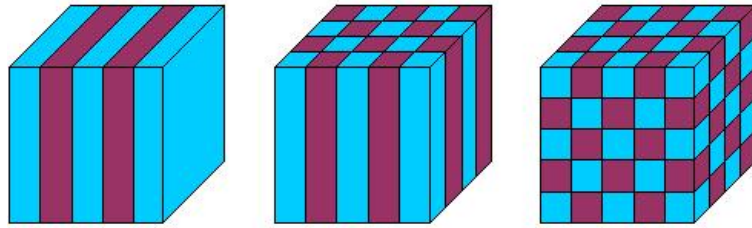


Figure 4.1: Representations of one-, two- and three-dimensional photonic structures (left to right). Different colours represent homogeneous blocks of material with different values of dielectric constant,  $\varepsilon$ .

that there is a frequency gap where complete destructive interference occurs and no electromagnetic waves can propagate [118]. One dimensional photonic crystal structures, such as the Bragg reflector, have been discussed in chapter 1. Bragg reflectors are highly efficient dielectric mirrors and tunable Bragg reflectors can have the range of frequencies at which they operate changed using compression to alter the refractive index of the layers in the structure. One-dimensional photonic crystals may also be structured to produce anti-reflection coatings by choosing layer thicknesses that align the reflected waves for destructive interference. These are used, for example, in telescopes and in spectacles. However, it was not until 1987 with the works of Yablonovitch [5] and John [6] that uses for higher-dimensional, periodic structures were proposed and the term *photonic crystal* was first used. Yablonovitch [5] proposed that spontaneous emission from atoms would be completely inhibited when the atoms were contained within a three-dimensional photonic crystal structure with a photonic band gap that overlapped the electric band edge. Any photon that would result from an electron-hole recombination having a frequency forbidden to propagate in the surrounding medium due to the photonic band gap, would be unable to be emitted from the atom. This effective suppression of spontaneous emission can be implemented in order to increase the efficiency of many devices, for example, LEDs and semiconductor lasers [119]. Around the same time John [6] proposed that defects in a three-dimensional photonic crystal structure would lead to strong localization of photons at the defect site.

Photonic crystal devices can also be used as highly effective waveguides by uti-

lizing a band gap that does not allow light to propagate outside of a waveguide channel [9]. This is most advantageous when attempting to channel light around a sharp corner. An optical fibre waveguide relying on total internal reflection requires a radius of curvature of no less than approximately  $10^3 \mu\text{m}$  to bend light round a  $90^\circ$  corner without unacceptable losses. A photonic crystal can perform the same operation on a scale of the order  $1 \mu\text{m}$  [120]. These phenomena have led to the design and fabrication of optical integrated circuits based on photonic crystals [121].

### 4.1.1 Electromagnetic waves in photonic crystals

The electromagnetic modes that are able to propagate through a photonic crystal must satisfy Maxwell's equations and the relevant boundary conditions. For good dielectric materials, such as those considered here, we have no currents or charges and can write  $\rho = 0$  and  $\mathbf{J} = 0$ . Hence Equations 1.2 – 1.5 may be simplified to:

$$\nabla \cdot \mathbf{D} = 0 \quad (4.1)$$

$$\nabla \cdot \mathbf{B} = 0 \quad (4.2)$$

$$\nabla \times \mathbf{E} = -\frac{\partial \mathbf{B}}{\partial t} \quad (4.3)$$

$$\nabla \times \mathbf{H} = \frac{\partial \mathbf{D}}{\partial t}. \quad (4.4)$$

The magnetic field may take the form:

$$\mathbf{H} = \mathbf{a} \exp(i\mathbf{k} \cdot \mathbf{r}) \quad (4.5)$$

where  $\mathbf{a}$  is the amplitude of the magnetic field strength,  $\mathbf{k}$  is the wavevector and in order to satisfy Equations 4.1 and 4.2 we require that  $\mathbf{a} \cdot \mathbf{k} = 0$  to give a transverse wave. Assuming a time dependence of the form  $\exp(-i\omega t)$ , Equations 4.3 and 4.4 give:

$$\nabla \times \mathbf{E} = i\omega\mu_0\mathbf{H} \quad (4.6)$$

$$\nabla \times \mathbf{H} = -i\omega\varepsilon\varepsilon_0\mathbf{E} \quad (4.7)$$

and by eliminating  $\mathbf{E}$  we obtain an eigenvalue equation where the eigenvectors give the field patterns of the harmonic modes:

$$\nabla \times \left[ \frac{1}{\varepsilon(\mathbf{r})} \nabla \times \mathbf{H}(\mathbf{r}) \right] = \frac{\omega^2}{c^2} \mathbf{H}(\mathbf{r}). \quad (4.8)$$

The solutions of Equation 4.8, energy as a function of wavevector, give the band structure of the photonic crystal. Any range of frequencies at which electromagnetic radiation cannot propagate through a photonic crystal is termed a *photonic band gap*.

In two- and three-dimensional photonic crystals the photonic band gap exists independent of the angle of incident light. Also in two- and three-dimensional structures there exist two distinct polarisations of light, commonly referred to as TE- and TM-polarisations: TE-polarised light has no electric field component in the direction of propagation and therefore has non-zero components  $H_x$ ,  $H_z$  and  $E_y$  and TM-polarisation light has no magnetic field component in the direction of propagation and therefore has non-zero components  $E_x$ ,  $E_z$  and  $H_y$ . Each polarisation has its own band structure independent from the other and the two may exhibit quite different behaviors as we discuss later. With current growth techniques, two- and three-dimensional photonic crystals are less simple to fabricate than one-dimensional structures and are more likely to suffer from imperfections and disorder however their increased complexities may give greater technological value.

## 4.2 Disorder in photonic crystals

Some form of disorder - any deviation from a perfect structure - is inherent in any photonic crystal. In order to assess their device potential and to make effective use of the optical properties of photonic crystals it is necessary to understand how disorder affects them. Of particular interest is the question of how disorder affects the photonic band gap.

Changes to the photonic band gap caused by well defined defects in photonic crystals are well known. For example a cavity defect, such as a double thickness layer in a one-dimensional photonic crystal or a missing feature in a two-dimensional photonic crystal, can create a localized mode at a frequency within the photonic band gap [122] [123]. Figure 4.2 shows the power transmission coefficient for a planar Bragg reflector structure with a cavity defect at its centre. The defect mode appears as a peak in the transmission spectrum dip. Defects giving rise to localized

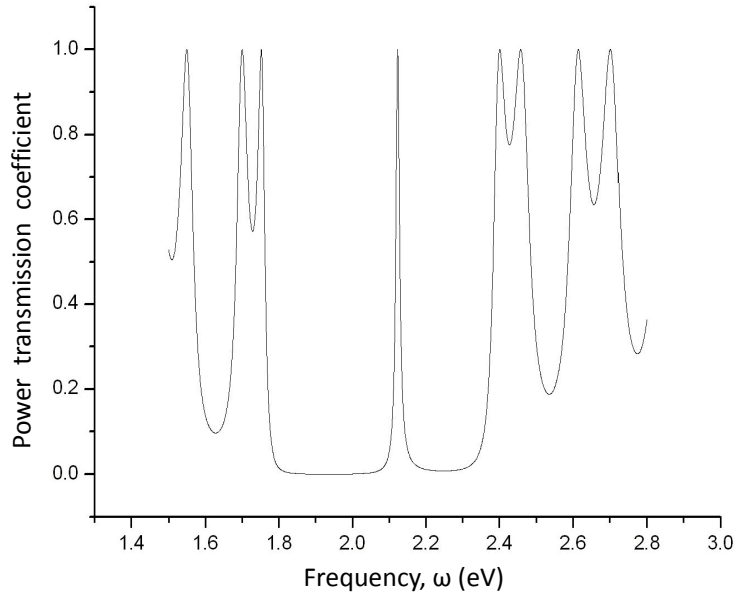


Figure 4.2: The power transmission coefficient for a planar Bragg reflector structure with a cavity defect at its centre. The defect mode can be seen as a peak in the transmission spectrum dip.

modes, such as that illustrated in Figure 4.2, have found application as resonant cavities, optical filters and lasers e.g. [10]. However, here we are concerned with more random disorder that is likely to be the result of the manufacturing process. The two-dimensional photonic crystal that is considered in this thesis is formed by an array of cylindrical holes in a slab of dielectric material. Disorder in such a structure may be due to variation in the size or shape of the holes, including roughness of the hole edge, or to the position of the axis of each hole.

#### 4.2.1 Disorder in two-dimensional photonic crystals

Early work on disorder in two-dimensional photonic crystals presented qualitative results for the effect of disorder on the photonic band gap. For example, Sigalas *et al.* [124] [125] used a transfer matrix method to study hexagonal and square arrays of cylinders of one dielectric constant in a slab of material of a different dielectric constant. The disorder imposed on the system took the form of variation in the cylinder radii, the position of the cylinder axes and the dielectric constant of the

cylinders. The disorder was measured as a filling ratio between the area covered by the cylinders and the background material in the plane perpendicular to the cylinder axes. The calculations were run at microwave frequencies so they could be compared to experimental results and the method was shown to give excellent agreement. They found that for wide photonic band gaps a greater amount of disorder was required to form localized states to close up the band gap. Band gaps occurring at higher frequencies were found to generally be narrower than gaps at lower frequencies and hence required less disorder to close them.

Ryu *et al.* [126] also investigated hexagonal and square arrays of cylinders of one dielectric constant in a slab of material of a different dielectric constant with either the cylinders or the background having a dielectric constant corresponding to air. They focused on disorder in the radii of the cylinders and introduced a Gaussian distribution of radii with mean  $r_0$  and standard deviation  $\delta r$ . Their results were also qualitative observations of the effect of disorder on the band gap. They found that for small fluctuations in the standard deviation of the distribution of radii there was little effect on the band gap whereas for large fluctuations in the standard deviation states appeared in the band gap causing it to narrow and close. They also found that increasing the mean radius caused the width of the band gap of the structures with air holes to increase and the width of the band gap of the structures with dielectric rods to decrease.

Much of the more recent work carried out on disorder in photonic crystals introduces a ‘disorder parameter’ to describe the amount of deviation from the ideal structure. In the early 2000s, Kaliteevski *et al.* investigated two-dimensional photonic crystals formed by an array of cylindrical air holes in a slab of GaAs with refractive index  $n = 3.6$  [127] [128]. They defined a disorder parameter  $\delta$  to describe the change in cylinder radius from that of the ideal crystal,  $r_0$  such that the disordered radii are uniformly distributed in the interval  $r_0(1 - \delta)$  to  $r_0(1 + \delta)$ . Two different polarisations of light were considered, each having a different photonic band structure. The so called TE-polarisation, having no electric field component in the direction of propagation, has an incomplete band gap while the so called TM-polarisation, with no magnetic field component in the direction of propagation has

a complete band gap. An incomplete band gap means that the range of frequencies that is forbidden to propagate is only restricted in certain reciprocal space directions whereas a complete band gap occurs for all wavevectors simultaneously. Kaliteevski *et al.* used a transfer matrix to model the transmission spectra of light through the photonic crystal. For both polarisations, the transmission spectra for the disordered photonic crystal structures were compared with that for the ideal, non-disordered structure. The transmission of light through the photonic crystal was modelled for both ‘ballistic’ light, that emerging from the far side of the structure parallel to the input beam, and ‘scattered’ light, light emerging at all other angles. For the case of the incomplete band gap, the transmission coefficients were averaged over many different configurations of the same disorder parameter. It was found that for light traveling ballistically through the disordered crystal, small peaks appear in the transmission dip due to localized photonic states. An increase in disorder led to more peaks appearing in the transmission dip, the amplitude of the peaks increased and the transmission dip became broader. For the case of a complete band gap it was asserted that for the ideal structure the frequency of the minimum of the transmission coefficient corresponds to the frequency at the centre of the photonic band gap. It was found for light traveling ballistically through a disordered structure peaks appeared in the transmission spectra causing an increase in the average transmission of light at the frequency of the centre of the photonic band gap. The increase in transmission coefficient over all frequencies was such that the frequency of the minimum of the transmission coefficient did not change. It was found that a critical value of disorder was required in order that localized states would appear at the frequency of the centre of the band gap and hence increase light transmission at this frequency.

In 2005 Beggs *et al.* considered the same hexagonal array of air holes in a dielectric structure with background refractive index  $n = 3.6$  for the polarisation with a complete band gap. In this study the disorder was in the shift of position of the cylinder axes from their ideal lattice position [129]. Reflection and transmission spectra were modelled for the ideal structure and structures with different disorder parameters. For small amounts of disorder there was little change from the ideal

case. For increasing amounts of disorder, the transmission dip narrows as localized states appear at the edges of the photonic band gap. For large amounts of disorder, states appear across all of the former photonic band gap causing an overall increase in transmission. This was confirmed by analysis of the density of states; it was shown using a plane wave method that for small disorder localized states were confined to the edges of the photonic band gap and that there was an extremely low probability of a localized state being found at the centre of the band gap. At some threshold value of disorder the probability of localized states being introduced at the centre of the band gap increased to a significant value.

Although studies have been carried out on disorder in two-dimensional photonic crystals, no quantitative relationship to relate the disorder parameter to the relative width of the photonic band gap has been proposed. Such a relationship has however been found in the simpler one-dimensional photonic crystals: Kaliteevski *et al.* [17] studied disorder in the thickness and refractive index of layers in a one-dimensional photonic crystal and also combined the two to look at disorder in optical thickness. They used a transfer matrix method to investigate the effect of disorder on the band gap. This led to the formulation of an empirical relationship for a threshold disorder parameter defined as the ‘amount’ of disorder that a one-dimensional photonic structure can withstand before the photonic band gap becomes degraded beyond an acceptable density of states at its centre. This acceptable level was defined by the ratio,  $S_{th}$ , of the density of states at the centre to that at the edge of the photonic band gap. The dependence found was expressed as

$$\delta_{th} = \frac{5}{2\sqrt{-\ln S_{th}}} \sqrt{\frac{\Delta\omega}{\omega_0}} \quad (4.9)$$

where  $\Delta\omega/\omega_0$  is the relative band width of the photonic band gap. It was found that the dependence of the threshold disorder parameter,  $\delta_{th}$  was only weakly dependent on the ratio  $S_{th}$ . Hence the threshold disorder parameter could be approximated for nearly all cases by the relation

$$\delta_{th} \approx \sqrt{\frac{1}{3} \left( \frac{\Delta\omega}{\omega_0} \right)} \quad (4.10)$$

For ensembles of  $10^6$  configurations of structures with the same disorder parameter, the mean transmission coefficient and its standard deviation were calculated. These

quantities were plotted as a function of disorder parameter and it was found that the point at which the standard deviation becomes larger than the mean value was well described by the threshold disorder parameter,  $\delta_{th}$  given by Equation 4.10. As  $\delta$  increases, localized modes appear in the photonic band gap. For  $\delta < \delta_{th}$  these modes appear at the edges of the photonic band gap and cause a slight increase in transmission coefficient. For  $\delta > \delta_{th}$  localized modes may, for some configurations, appear close to the centre of the photonic band gap, increasing the transmission coefficient by a much greater amount. The crossing of the mean and standard deviation is identified as being due to the wide range of values (0 to 1) that the transmission coefficient for the frequency at the centre of the band gap may take when  $\delta > \delta_{th}$ . This occurs for any individual structure in the ensemble and hence the standard deviation is greater than the mean value.

The work presented in this chapter considers the same two-dimensional photonic crystal structure as in [128] and [129] for the case of a complete photonic band gap and for a range of values of the background refractive index in an attempt to find a unifying relationship between the disorder parameter and the relative band width,  $\Delta\omega/\omega_0$ . The analysis is inspired by the relationship found for one-dimensional photonic crystals in [17].

### 4.3 Introduction to *OmniSim*

The results in this section were obtained by running simulations using the commercially available software package, *OmniSim*. *OmniSim* uses Finite Difference Time Domain (FDTD) calculations to simulate electromagnetic fields propagating through areas of different refractive index which may be designed within the software. The FDTD method is a way of computationally calculating electric and magnetic fields at different points in time and space. It was first proposed in 1966 by K. Yee [130] and is outlined here.

Maxwell's equations, given in Equations 1.2 – 1.5, may be discretised in time and space. It can be seen that the change in electric field with time depends on the change in magnetic field in space and that the change in magnetic field with time

depends on the change in electric field in space. For propagation of the field only in the  $x$ -direction, the finite steps in time and space for the electric and magnetic fields are given by the formulae [131]:

$$\begin{aligned}\frac{\partial f}{\partial t} &\equiv \lim_{\Delta t \rightarrow 0} \frac{f(x, t_2) - f(x, t_1)}{\Delta t} \approx \frac{f(x, t_2) - f(x, t_1)}{\Delta t} \\ \frac{\partial f}{\partial x} &\equiv \lim_{\Delta x \rightarrow 0} \frac{f(x_2, t) - f(x_1, t)}{\Delta x} \approx \frac{f(x_2, t) - f(x_1, t)}{\Delta x}\end{aligned}\quad (4.11)$$

where  $f$  may represent either the electric or magnetic field. Hence for each step forward in time the electric and magnetic fields may be calculated alternately, in a ‘leap-frog’ manner.

The structure under consideration is a slab of semiconductor material containing a hexagonal array of cylindrical air holes as shown in Figure 4.3. The lattice parameter  $a$  is defined as the distance between the centres of adjacent cylinders and the angle between each of the outer cylinders is  $60^\circ$ . To use the FDTD method

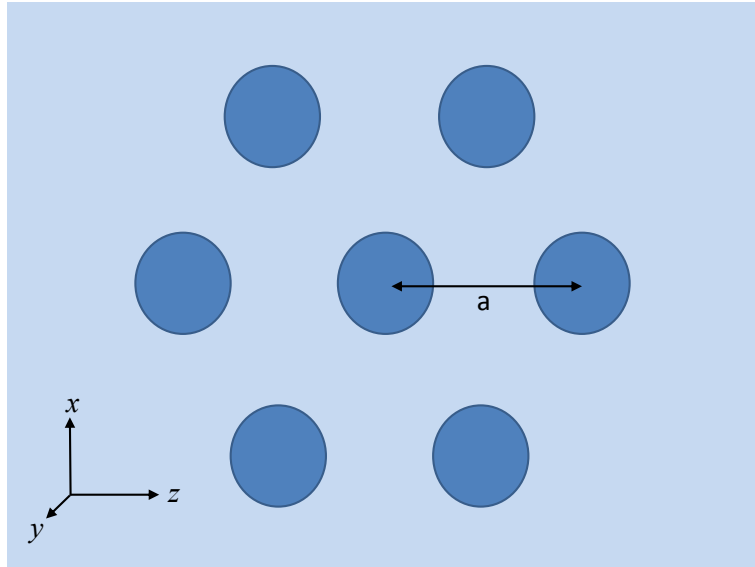


Figure 4.3: An  $x$ - $z$  plane view of the structure of a hexagonal array of cylindrical air holes (dark blue) in a slab of semiconductor (light blue) showing the lattice parameter,  $a$ . The  $y$ -direction is out of the page.

the structure must be split into a grid of points at which the electric and magnetic fields can be calculated. As the lattice dimension in the  $x$ -direction is an irrational number ( $\sqrt{3}a/2$ ) the lattice as it stands cannot be split into an integer number of grid points. Nevertheless it is important for the calculation that the grid sampling

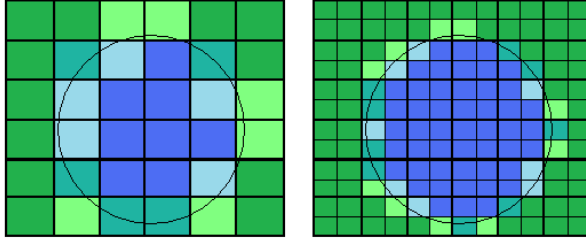


Figure 4.4: The colours in the grid represent the different refractive indices that are assigned to each square. Squares completely inside the circle have one refractive index, squares completely outside the circle have another. The grid on the right has twice as many squares as that on the left and the circle is more clearly defined.

points occur at the same place within each of the cylinders. To achieve this a ratio of integers is chosen to approximate the irrational lattice length.  $\sqrt{3}/2 \approx 0.866$ . The ratios  $6/7 \approx 0.857$  and  $7/8 \approx 0.875$  are equally different from the ratio required and the 1 by  $6/7$  grid was chosen. The smaller the grid spacing, the more accurately the array of cylinders is represented.

Figure 4.4 shows how the computer program interprets the device in terms of the grid spacing. The 2D device is pixelated into squares. Squares that fall completely inside the cylinders are assigned refractive index i.e. dark blue colour, squares that fall completely outside the cylinders are assigned another refractive index i.e. dark green. Squares that overlap the boundaries (shown light blue, light green and turquoise in the figure) are assigned an average refractive index by area of cylinder/background that they cover.

The time interval,  $\delta t$  used by *OmniSim* is calculated automatically by the FDTD engine, so that it is just small enough to meet the Courant stability condition, using the formula [132]

$$\delta t = 0.99 \sqrt{\frac{1}{3}} \frac{\text{grid spacing}}{c} \quad (4.12)$$

where  $c$  is the speed of light in a vacuum. However, the number of time steps can be chosen. *OmniSim* simulates light entering the structure as a pulse and it is important to choose a number of time steps large enough that the pulse has completely traversed the structure and that any reflections have had time to decay away. The number of time steps used was chosen by running several initial calculations with

increasing numbers of time steps until the output did not change. As with all computational methods, the accuracy of the calculation becomes limited by the length of time available.

Using a pulsed input gives a whole range of frequency responses with just one calculation. A sinusoidal pulse may be written as a function of time:

$$f(t) = \sin \omega_0 t \quad (4.13)$$

for  $|t| < \tau/2$ . The Fourier transform of this function is

$$\begin{aligned} F(\omega) &= \int_{-\infty}^{\infty} f(t) \exp(i\omega t) dt = \int_{-\tau/2}^{\tau/2} \sin \omega_0 t \exp(i\omega t) dt \\ &= \frac{1}{2i} \int_{-\tau/2}^{\tau/2} \exp(i(\omega + \omega_0)t) - \exp(i(\omega - \omega_0)t) dt \\ F(\omega) &= -i \left( \frac{\sin [(\omega + \omega_0)\tau/2]}{\omega + \omega_0} - \frac{\sin [(\omega - \omega_0)\tau/2]}{\omega - \omega_0} \right). \end{aligned} \quad (4.14)$$

Function 4.14 has zeros where  $(\omega \pm \omega_0)\tau/2 = n\pi$  and  $n$  is an integer value. This means that frequencies given by Equation 4.15:

$$\omega = \frac{2n\pi}{\tau} \pm \omega_0 \quad (4.15)$$

are not represented by the sinusoidal pulse. The longer the pulse duration, the fewer frequencies are missed. As explained later, the frequency we are most interested in is that corresponding to the centre of the band gap for each of the photonic crystals under consideration. Therefore it was necessary to choose a pulse time such that the centre of band gap frequency, and those close to it, were not missing from the calculations.

## 4.4 The photonic crystal structure

### 4.4.1 The ideal structure

The ideal structure is that of a perfect photonic crystal with the radius,  $r_0$  of every air cylinder being the same:  $r_0 = 0.4a$ . The ideal structure as it appears in *OmniSim* is shown in Figure 4.5. The program models light propagating through the structure. Light is ‘emitted’ from the excitor, shown in yellow at the bottom of Figure 4.5 and ‘detected’ by the two sensors, shown in shades of red. The bright red line is sensor 1 and the darker red line at the top of the figure is sensor 2. For this investigation the light is TM-polarised so that the photonic crystal under consideration has a complete band gap, the non-zero field components are  $E_x$ ,  $E_z$  and  $H_y$ . The device dimensions are  $15 \mu\text{m}$  in the  $z$ -direction by  $15.5 \mu\text{m}$  in the  $x$ -direction where the extra  $0.5 \mu\text{m}$  in the  $x$ -direction allows for the placement of the excitor and sensors. The ideal photonic crystal should also be infinite in order to avoid the effects of any edges therefore boundary conditions were applied at the edges of the device, in the  $x$ - $y$  plane at  $z = \pm 7.5 \mu\text{m}$  to simulate periodic repetition of the device. The lattice parameter,  $a = 1.0 \mu\text{m}$ .

In our investigations several different refractive indices are considered for the substrate. GaN has a refractive index  $n = 2.43$ , other refractive indices were then chosen without specific reference to any named material. The lowest refractive index considered was  $n = 1.8$ , below this value the photonic band gap for the TM-polarisation is very small due to the low contrast between the holes and the substrate. Above a substrate refractive index of  $n = 3.0$  the results from the *OmniSim* program were not consistent, with instabilities possibly being due to the large refractive index contrast. Therefore data collected for  $n \geq 3.0$  has been excluded and the highest refractive index considered in the analysis was  $n = 2.7$ .

The band structure for a photonic crystal consisting of a slab of GaN with cylindrical air holes in a hexagonal array is illustrated in Figure 4.6. The black lines give the band structure for the TM-polarisation while the red dashed lines give the band structure for the TE-polarisation. It can be seen that there is a complete band gap for the TM-polarisation between the first and second bands that exists in all

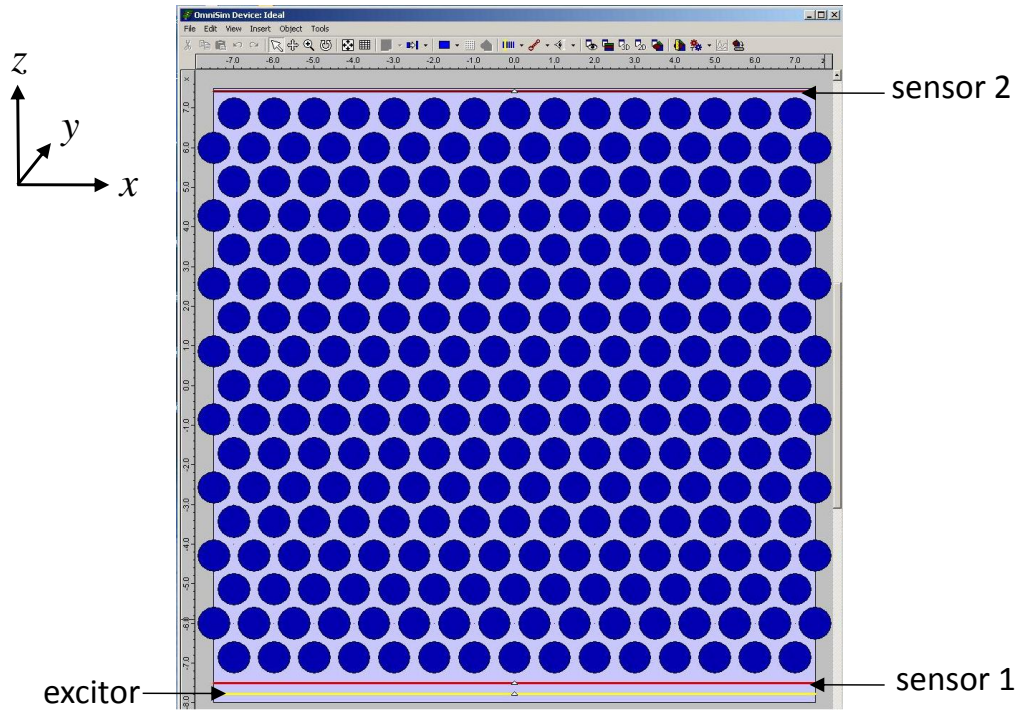


Figure 4.5: Screen shot of the ideal structure as it appears in *OmniSim*. The radius of each air cylinder is  $0.4a$  where  $a$  is the lattice parameter. The light blue background represents the substrate material. The photonic crystal has varying dielectric constant in the  $x$ - $z$  plane and is homogeneous in the  $y$ -direction. The excitor (yellow) and the two sensors (red) are indicated.

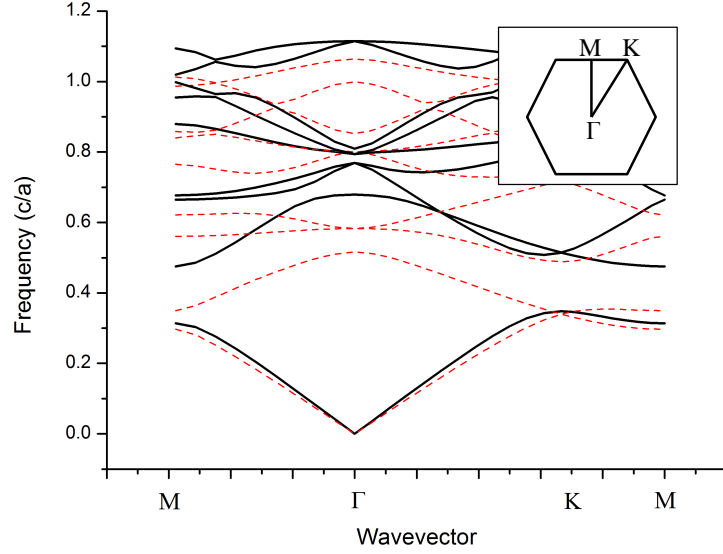


Figure 4.6: The band structure for TM (black) and TE (red) polarised light in a GaN slab (refractive index  $n = 2.43$ ) with a hexagonal array of cylindrical air holes each with radius  $0.4a$ . The inset shows the first Brillouin zone of the ideal crystal and marks the wavevector directions within the crystal.

wavevector directions simultaneously. The TE-polarisation has an incomplete band gap and is not considered in the work presented in this thesis. The relative band width is defined as  $\Delta\omega/\omega_0$  where  $\Delta\omega$  is the frequency difference between the upper and lower bands either side of the band gap and  $\omega_0$  is the frequency at the centre of the band gap.

The band gap of the ideal crystal structure may also be shown as a dip in the relative transmission of a TM-polarised light pulse across the crystal. Figure 4.7 shows the amount of light at different frequencies recorded at sensor 2 relative to that passing through sensor 1 (see Figure 4.5). The large dip in the transmission corresponds to frequencies for which propagating states do not exist in an infinite crystal - the photonic band gap. The dip in the curve is not perfectly smooth and this is an artifact of the simulation process and the fact that the crystal under consideration is not infinite.

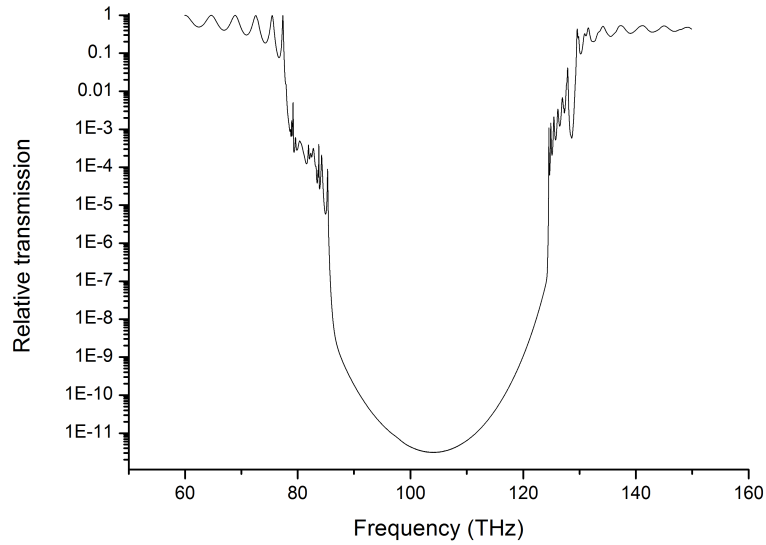


Figure 4.7: Relative transmission of a TM pulse across an ideal photonic crystal structure such as that shown in Figure 4.5 with GaN as the background material.

#### 4.4.2 The disordered structure

For the disordered structures, the level of disorder is defined by the same parameter  $\delta$  as used in [128]. The radius of each of the cylinders in the array is randomly attributed a value in the range  $r_0(1 - \delta)$  to  $r_0(1 + \delta)$  such that the distribution of radii is that shown in Figure 4.8.

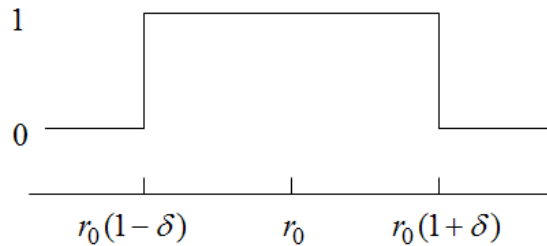


Figure 4.8: The distribution of cylinder radii depending on the disorder parameter,  $\delta$ .

The maximum disorder parameter that can be considered before the cylindrical air holes start merging into larger, non-uniform areas of refractive index  $n = 1.0$  is

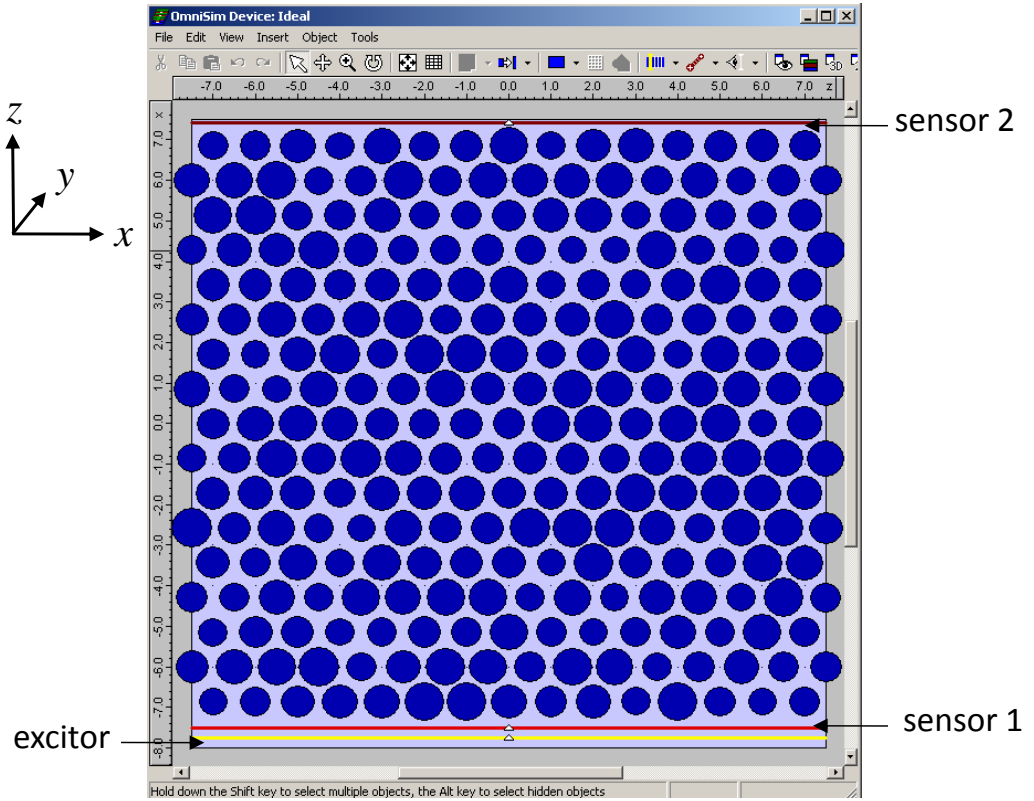


Figure 4.9: An example disordered structure as it appears in *OmniSim*. The radius of each cylinder is randomly attributed from a distribution about  $r_0 = 0.4a$  where  $a$  is the lattice parameter, as shown in Figure 4.8.

given by

$$0.5a = r_{\max} = r_0(1 + \delta_{\max}) \quad (4.16)$$

where  $a$  is the lattice parameter. We have  $r_0 = 0.4a$  and therefore the maximum disorder parameter that may be considered is  $\delta_{\max} = 0.25$ .

## 4.5 Analysis

The following sections describe two different ways of analysing the data given by the simulations. An analysis of the flux transmitted through the photonic crystal gives an interpretation of the threshold disorder parameter  $\delta_{\text{th}}^F$  and a directional analysis of the energy flow through the structure gives an interpretation of a differently defined threshold disorder parameter  $\delta_{\text{th}}^E$ .

### Flux analysis

For this analysis, the total flux transmitted through sensor 2, relative to the total flux transmitted through sensor 1, as a function of frequency was recorded from the *OmniSim* simulations. For each value of the disorder parameter  $\delta$ , the simulation was run with ten different random configurations of the cylinders with disordered radii. In each case the flux was recorded and a threshold disorder,  $\delta_{\text{th}}^F$  was defined to be the disorder value at which the standard deviation of the fluxes for different configurations became greater than the mean value. The reference for this analysis is the flux through sensor 1.

### Energy analysis

In the next analysis, the real and imaginary parts of the  $H_y$  field component were recorded from the simulation as a function of position along sensor 2 for the frequency at the centre of the photonic band gap. This was used to calculate the energy flow through sensor 2 as a function of scattering angle. Following [128] and [129] we consider ‘ballistic’ and ‘scattered’ light separately. Light passing through sensor 2 with scattering angle close to zero is defined as ‘ballistic’, whereas light passing through sensor 2 with all other scattering angles is defined as ‘scattered’. It may be the case that some light undergoes multiple scattering events before passing through sensor 2 with scattering angle close to zero and is designated as ballistic light. In this analysis the threshold disorder,  $\delta_{\text{th}}^E$  is defined as the disorder value for which the energy in the scattered light becomes greater than that in the ballistic light. The reference for this analysis is the total energy flow through sensor 2.

We present empirical formulae relating the different threshold disorder parameters to the relative band width and separately to the mean refractive index of the photonic crystals. The frequency limits of the band gap for photonic crystals with different substrate refractive indices are also considered.

#### 4.5.1 Flux analysis

It is known that disorder in a photonic crystal causes degradation of the photonic band gap e.g. [17]. For small values of disorder this affects only the edges of the band gap but for larger values of disorder, states may appear towards the centre of the band gap. To investigate the quality of the centre of the photonic band gap, simulations to calculate the relative flux transmitted through the crystal were carried out. The total flux transmitted through sensor 2 was recorded as a function of frequency relative to the total flux transmitted through sensor 1. The thick black line in Figure 4.10 shows the relative transmitted flux as a function of frequency for the ideal photonic crystal with background refractive index  $n = 2.7$ . Similar simulations were carried out for photonic crystals with a degree of disorder in the radii of the air cylinders. The thin dotted black line in Figure 4.10 shows the relative transmitted flux in the case of one random configuration of disordered radii with disorder parameter  $\delta = 0.18$ . As discussed in Section 4.2, defects in photonic crystals cause states to appear in the photonic band gap. In this investigation we are interested in the effect of disorder applied to the whole crystal rather than individual defects. Therefore, in order to smooth artifacts arising from any particular distribution of the range of radii, the simulation was run for ten different random configurations for each disorder parameter. The thick red line in Figure 4.10 shows the mean relative transmitted flux for 10 random configurations of disorder with  $\delta = 0.18$ . We note that ten is not a very large number of configurations from which to calculate statistics however the number of simulations was restricted by the time taken to run each one.

For each value of disorder we were interested in the effect on the transmission

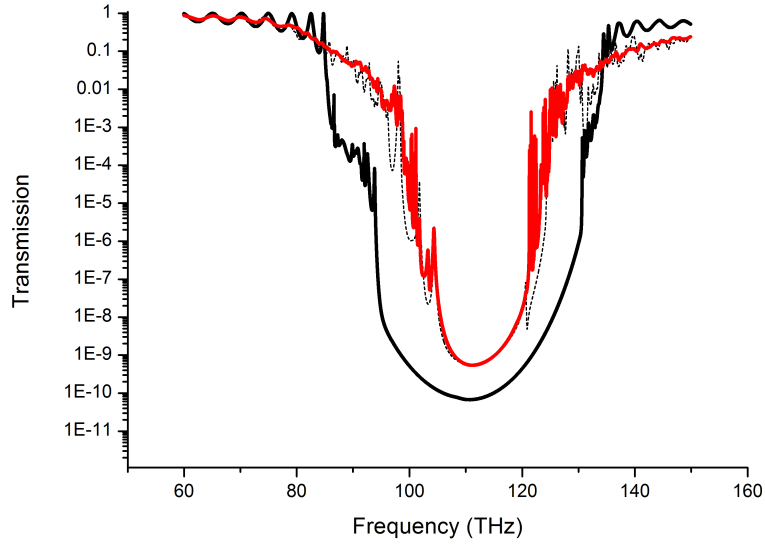


Figure 4.10: Relative transmitted flux as a function of frequency for the ideal structure (thick black line) with background refractive index  $n = 2.7$ , a randomly disordered structure with  $\delta = 0.18$  (thin black line) and the mean relative transmitted flux for 10 random configurations of disorder parameter  $\delta = 0.18$  (red).

at the frequency at the centre of the band gap,  $\omega_0$ . In order to take into account any peaks close to the centre, the arithmetic mean and standard deviation of the relative transmitted flux values for frequencies in the mid-1/20<sup>th</sup> of the band gap were calculated. The mid-1/20<sup>th</sup> of the band gap was chosen following the works of Kaliteevski *et al.* [128] – [17]. Preliminary calculations showed that the mean taken over the mid-1/10<sup>th</sup> or mid-1/40<sup>th</sup> differed from the mid-1/20<sup>th</sup> by less than 4 % at disorder parameter  $\delta = 0.18$ .

Figure 4.11 shows the mean and standard deviation of the relative transmitted flux, in the relevant frequency range, as a function of disorder parameter  $\delta$ , for photonic crystals with different background refractive indices: a)  $n = 1.8$ , b)  $n = 2.0$ , c)  $n = 2.2$ , d)  $n = 2.43$ , e)  $n = 2.7$ . The thick black line is a b-spline fit to the mean relative transmitted flux for frequencies in the mid 1/20<sup>th</sup> of the band gap. The thick red line is a b-spline fit to the standard deviation of the same set of values.

All cases in Figure 4.11 show an increasing amount of light transmitted at the

central frequency of their respective photonic band gaps with increasing disorder except for graph b) which exhibits a decrease in transmission for the highest level of disorder considered. This may be an artifact of the random configurations of disorder considered.

Kaliteevski *et al.* [17] found that, for the case of one dimensional photonic crystals with disorder imposed on the thickness of the layers, the threshold disorder parameter could be approximated by the relation given in Equation 4.10. For ensembles of many structures with the same disorder parameter, differing from each other only by the random fluctuations in layer thickness, the mean transmission coefficient and its standard deviation were calculated. These quantities were plotted as a function of disorder parameter and it was found that the point at which the standard deviation became larger than the mean value was well described by the threshold disorder parameter,  $\delta_{th}$  given by Equation 4.10. Defining the threshold disorder for the two-dimensional case in a similar manner we have that  $\delta_{th}^F$  is the disorder parameter for which the standard deviation of the relative transmitted flux for frequencies in the mid  $1/20^{th}$  of the photonic band gap becomes greater than the mean. This threshold is indicated in a) to e) in Figure 4.11 by the right hand dotted green construction lines. The dotted black lines in Figure 4.11 indicate the mean relative transmitted flux plus one standard deviation and the horizontal green construction line intersects to give an estimate of the one standard deviation error on  $\delta_{th}^F$ .

Figure 4.12 shows the threshold disorder parameter  $\delta_{th}^F$  as a function of the relative band width  $\Delta\omega/\omega_0$  for the complete band gap measured in the M direction of the crystal (illustrated in Figure 4.6).

Although there is a slight decrease in threshold disorder with increasing relative band width, the horizontal red line shows that a constant  $\delta_{th}^F$  of  $0.2048 \pm 0.0012$  fits the data within the estimated error bounds and the variation of  $\delta_{th}^F$  with relative band width is negligible.

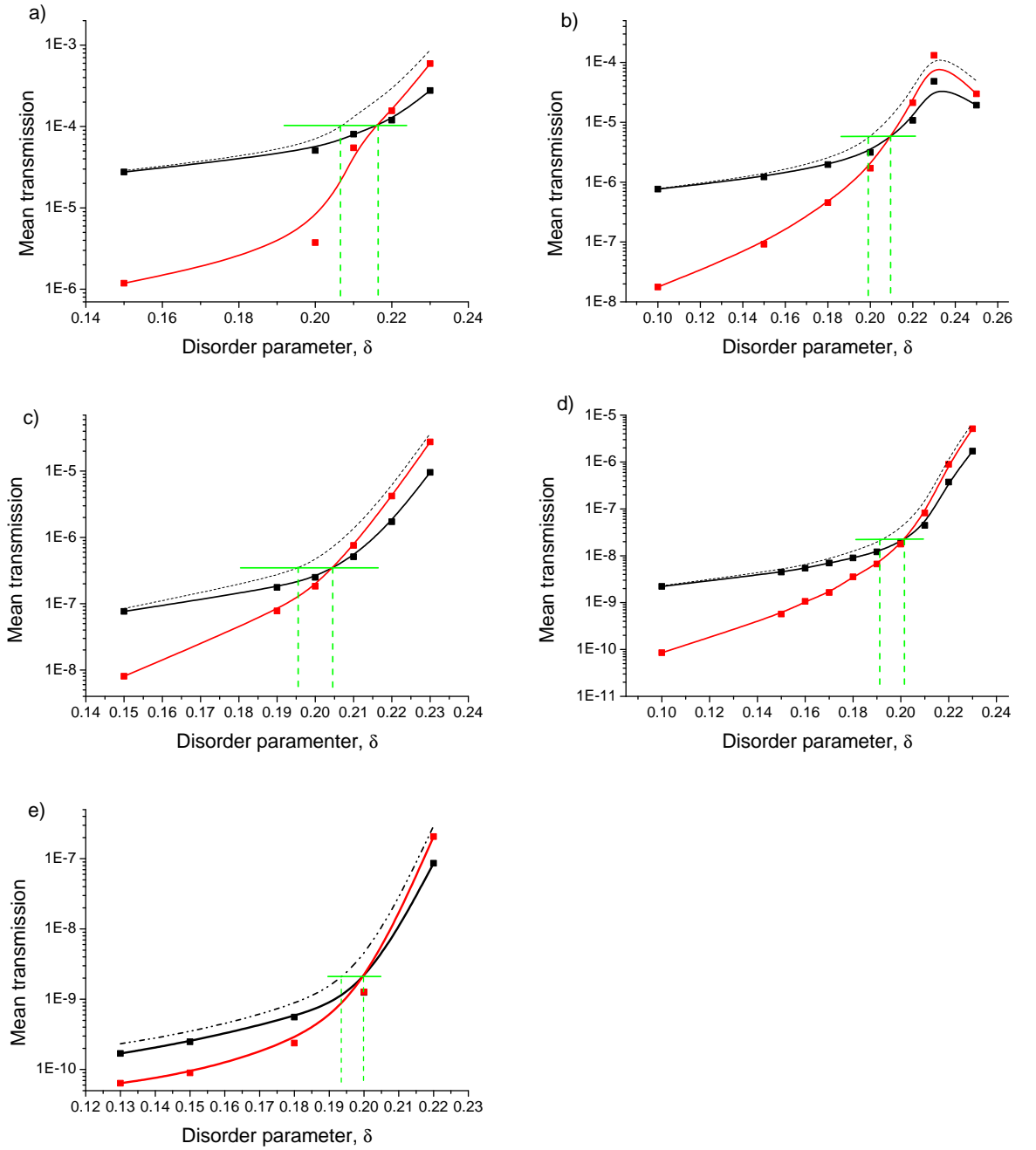


Figure 4.11: The mean (solid black) and standard deviation (red) of transmitted flux in the mid  $1/20^{th}$  of the photonic band gap for structures with background refractive index a)  $n = 1.8$ , b)  $n = 2.0$ , c)  $n = 2.2$ , d)  $n = 2.43$ , e)  $n = 2.7$ . The dotted black line shows the one standard deviation error bound on the mean. The green construction lines show the threshold disorder,  $\delta_{th}^F$  (right) and the lower error bound (left).

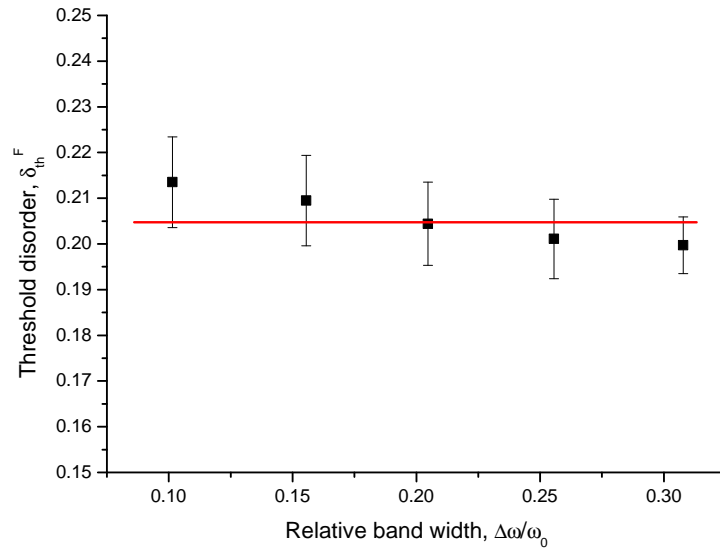


Figure 4.12: Threshold disorder parameter  $\delta_{th}^F$ , defined as the point at which the standard deviation of the relative transmitted flux becomes greater than the mean, as a function of the relative band width  $\Delta\omega/\omega_0$ .

## 4.5.2 Directional energy analysis

We now consider the energy flow through sensor 2 as a function of the scattering angle  $\theta$ . The wavevector of the input pulse,  $k_{\text{in}}$ , is in the  $x$ -direction, perpendicular to the sensor. Its magnitude is given by

$$k_{\text{in}} = \frac{2\pi n}{\lambda} = nk_0 \quad (4.17)$$

where  $n$  is the background refractive index of the photonic crystal slab and  $\lambda$  is the free space wavelength chosen to be that corresponding to the frequency at the centre of the photonic band gap. The background refractive index is used because the excitor and both of the sensors are placed in the background material and not in contact with any of the air holes. Any scattered wave with a component,  $k_z$  parallel to the sensor has scattering angle given by

$$\theta = \sin^{-1} \left( \frac{k_z}{nk_0} \right). \quad (4.18)$$

We can also calculate the wavevector component in the  $x$ -direction:

$$k_x = \sqrt{k_{\text{in}}^2 - k_z^2}. \quad (4.19)$$

To calculate the energy flow, Parseval's theorem may be used for both space and time:

$$\int_{-\infty}^{\infty} \int_{-\infty}^{\infty} f(z, t) g^*(z, t) dz dt = \frac{1}{(2\pi)^2} \int_{-\infty}^{\infty} \int_{-\infty}^{\infty} F(k_z, \omega) G^*(k_z, \omega) dk_z d\omega \quad (4.20)$$

where  $F(k_z, \omega)$  and  $G(k_z, \omega)$  are the Fourier transforms of  $f(z, t)$  and  $g(z, t)$  respectively. We have that:

$$\begin{aligned} \int_{-\infty}^{\infty} \int_{-\infty}^{\infty} H_y(z, t) E(z, t) dz dt &= \frac{1}{(2\pi)^2} \int_{-\infty}^{\infty} \int_{-\infty}^{\infty} H_y(k_z, \omega) E(-k_z, -\omega) dk_z d\omega \\ &= \frac{1}{(2\pi)^2} \int_{-\infty}^{\infty} \int_{-\infty}^{\infty} H_y(k_z, \omega) E^*(k_z, \omega) dk_z d\omega \end{aligned} \quad (4.21)$$

where, for the TM-polarisation used in this investigation, the non-zero field components are  $E_x$ ,  $E_z$  and  $H_y$  and it is assumed that there is only an  $H_y$  component to the magnetic field even in the presence of scattering. Poynting's vector may be

calculated as:

$$\mathbf{E} \times \mathbf{H} = \begin{vmatrix} \hat{x} & \hat{y} & \hat{z} \\ E_x & 0 & E_z \\ 0 & H_y & 0 \end{vmatrix} \quad (4.22)$$

$$= (-E_z H_y) \hat{x} + (E_x H_y) \hat{z} \quad (4.23)$$

We know that  $E_{x,z}(k_z, \omega)$  is perpendicular to  $H_y(k_z, \omega)$  and that it must be orientated such that the energy flow is along the direction of the scattered wavevector,  $k_s$  which is defined by the scattering angle  $\theta$  given in Equation 4.18. The magnitude of  $E_{x,z}(k_z, \omega)$  can be calculated using

$$\begin{aligned} E_{x,z}(k_z, \omega) &= Z H_y(k_z, \omega) \\ &= \frac{c\mu_0}{n} H_y(k_z, \omega) \end{aligned} \quad (4.24)$$

where  $c$  is the velocity of light,  $n$  is the refractive index,  $\mu_0$  is the permeability of free space and  $Z$  is the wave impedance. The electric field components obtained in this way are consistent with the output from *OmniSim*.

The integral, Equation 4.20 tells us that the fields at  $\pm\omega$  and  $\pm k_z$  contribute to the energy flow per unit frequency per unit wavevector:

$$\begin{aligned} S = \frac{1}{2\pi} [ &H_y(k_z, \nu) E_{x,z}^*(k_z, \nu) + H_y(-k_z, -\nu) E_{x,z}^*(-k_z, -\nu) \\ &+ H_y(k_z, -\nu) E_{x,z}^*(k_z, -\nu) + H_y(-k_z, \nu) E_{x,z}^*(-k_z, \nu)] \end{aligned} \quad (4.25)$$

where we have converted from  $\omega$  to the frequency in terms  $\nu = \omega/2\pi$ . The first two terms give the energy flow in the direction  $+\theta$  and the second two terms give the energy flow in the direction  $-\theta$ . Using

$$H_y(-k_z, -\nu) E_{x,z}^*(-k_z, -\nu) = H_y^*(k_z, \nu) E_{x,z}(k_z, \nu) \quad (4.26)$$

we have that the energy flow per unit frequency ( $\nu$ ) per unit wavevector ( $k_z$ ) is equal to twice the real part of Equation 4.25:

$$S = \frac{1}{\pi} \text{Re} [H_y(k_z, \nu) E_{x,z}^*(k_z, \nu)] \quad (4.27)$$

$n$	$\lambda / \mu\text{m}$	$k_{\text{in}} / \mu\text{m}^{-1}$
1.8	2.2161	5.1034
2.0	2.3202	5.4161
2.2	2.4213	5.7089
2.43	2.5349	6.0232
2.7	2.6667	6.3616
3.0	2.8121	6.7030

Table 4.1: Values for the incident wavevector,  $k_{\text{in}}$  for structures with different background refractive indices,  $n$  and wavelength  $\lambda$  at the centre of their photonic band gap.

Sometimes a more useful quantity is energy flow per unit frequency per unit scattering angle. Writing:

$$\begin{aligned}
k_z &= nk_0 \sin \theta \\
dk_z &= nk_0 \cos \theta d\theta \\
dk_z &= k_x d\theta = \sqrt{k_{\text{in}}^2 - k_z^2} d\theta
\end{aligned} \tag{4.28}$$

the energy flow per unit frequency per unit scattering angle is given by:

$$\begin{aligned}
S &= \frac{k_x}{\pi} \text{Re} [H_y(k_z, \nu) E_{x,z}^*(k_z, \nu)] \\
S &= \frac{\sqrt{k_{\text{in}}^2 - k_z^2}}{\pi} \text{Re} [H_y(k_z, \nu) E_{x,z}^*(k_z, \nu)].
\end{aligned} \tag{4.29}$$

In cases where  $k_z > k_{\text{in}}$  the wavevector  $k_x$  is imaginary indicating an evanescent wave, and there is no real energy flow across the sensor. The values for  $k_{\text{in}}$  for the structures under consideration are given in Table 4.1.

In the calculations carried out the *OmniSim* simulations give the real and imaginary parts of the field component  $H_y$  at discrete points along the second sensor for a specific frequency. The grid spacing used was  $0.07143 \mu\text{m}$  and the simulations were set up so that in each case the frequency corresponded to the centre of the band gap. The real and imaginary parts of  $H_y(z)$  were Fourier transformed to give  $H_y(k_z)$  using a Fast Fourier Transform algorithm in the analysis software OriginPro 8.1.

With  $H_y(k_z) = a + ib$  it follows that:

$$\text{Re} [H_y(k_z, \nu) E_{x,z}^*(k_z, \nu)] = Z(a^2 + b^2) \quad (4.30)$$

where  $Z$  is the wave impedance. As an example, the Fourier transform of the  $H_y$  component of the field at sensor 2, for an ideal photonic crystal with background refractive index 2.7, is shown in Figure 4.13. The field contribution with  $k_z$  close to

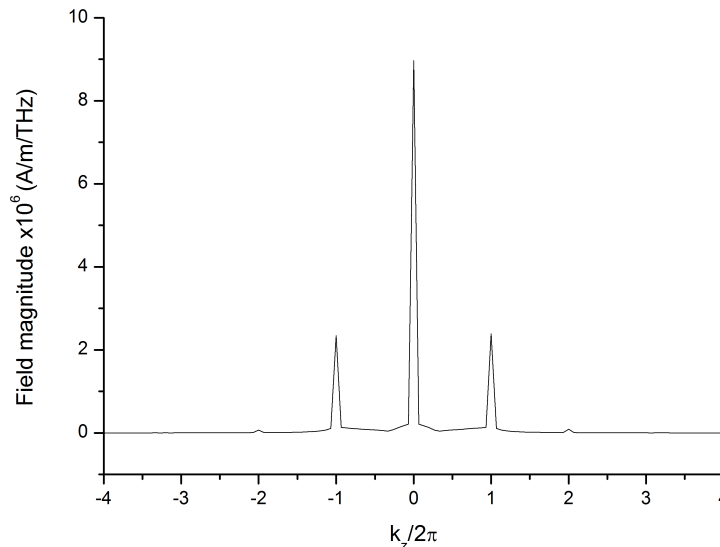


Figure 4.13: The Fourier transformed  $H_y$  field component at sensor 2 for a 2D hexagonal photonic crystal.

zero, the central peak, corresponds to light emerging from the structure in the  $x$ -direction and essentially parallel to the incident pulse. The other main contributions to the field at  $k_z$  values in multiples of  $\pm 2\pi$  occur due to light scattering from the lattice of air holes.

Following [128] and [129], we consider separately the ‘ballistic’ and ‘scattered’ light. In these papers, ballistic light is defined to be that which emerges from the photonic structure with a wavevector parallel to that of the input wave and scattered light is that with all other wavevectors. For this thesis, in order to work with the output from the simulations, we consider the scattering angle: the smallest difference in scattering angle that can be considered is defined by the finite size of

the structure shown in Figure 4.5, in the  $z$ -direction which we denote by  $L$ . We note that the simulation applies periodic boundary conditions on the structure in the  $z$ -direction. This ensures that there are no reflections from edges in the structure but does not allow for  $L$  to be considered infinite for the purposes of calculating the finite increments in scattering angle. The smallest interval that can be resolved in reciprocal space is given by

$$\Delta k = \frac{2\pi}{L} \quad (4.31)$$

which, in these simulations with  $L = 15 \mu\text{m}$ , gives  $\Delta k = 0.4189 \mu\text{m}^{-1}$ . It follows that the smallest increment in scattering angle is given by

$$\Delta\theta = \sin^{-1} \left( \frac{\Delta k}{nk_0} \right) \quad (4.32)$$

and hence the angular resolution depends on the material under consideration. We define ballistic light to be that emerging from the photonic structure at an angle less or equal to than  $\pm\Delta\theta$ . Any waves with a greater scattering angle are considered as scattered light.

In the analysis of Equation 4.29 we may consider any contribution to the energy flow per unit frequency per unit scattering angle for the ideal crystal outside of the ballistic range, to be subtractable from the corresponding results for disordered systems as a background correction. Figure 4.14 is obtained from Equation 4.29 for the ideal structure (black) with background refractive index  $n = 2.7$  and for one configuration of each of four levels of disorder (shown in colour). The black line, excluding the central peak at  $\theta = 0$  can be subtracted from the coloured lines leaving the energy flow per unit frequency per unit scattering angle that results from the disorder. In a few cases making this background correction returns a negative value for the energy, which is unphysical but arises due to the imperfect nature of simulations. The negative values are very small (less than 0.05% of the positive peak values) and so are simply set to zero.

It can be seen in Figure 4.14 that as the disorder parameter increases the amount of energy per unit frequency across all scattering angles increases significantly. At large scattering angles there is roughly a 2 order of magnitude increase in the transmitted energy between  $\delta = 0.05$  and  $\delta = 0.2$ . Disorder creates localized states in the

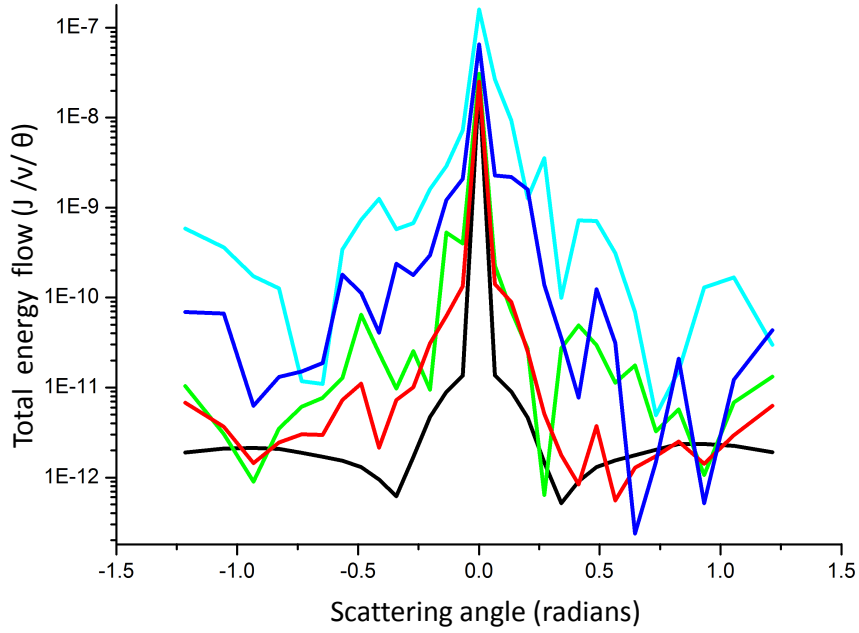


Figure 4.14: Energy flow per unit frequency into scattering angle  $\theta$  for the ideal structure (black) and one configuration each of four levels of disorder:  $\delta = 0.05$  (red),  $\delta = 0.10$  (green),  $\delta = 0.15$  (blue) and  $\delta = 0.20$  (cyan).

photonic band gap and as the amount of disorder increases, the number of localized states increases. The transmission coefficient at frequencies across the band gap is increased due to the additional states and therefore the transmission coefficient and the energy flow through the structure also increases.

The background-corrected energy flows as a function of scattering angle are integrated over all angles and also between  $\pm\Delta\theta$ . The ballistic light contribution is given by the second integral and the scattered light contribution is the difference between the two integrals. Figure 4.15 shows the results of considering ten disorder configurations to obtain the mean (solid symbols) and standard deviation (open symbols) for each value of disorder parameter. The data points are fitted with a b-spline curve. There is roughly a two order of magnitude difference in the energy flows, both ballistic and scattered, between each of the background refractive indices considered. The greater the refractive index difference between the background and the holes, the greater the width of the photonic band gap. A wider photonic band

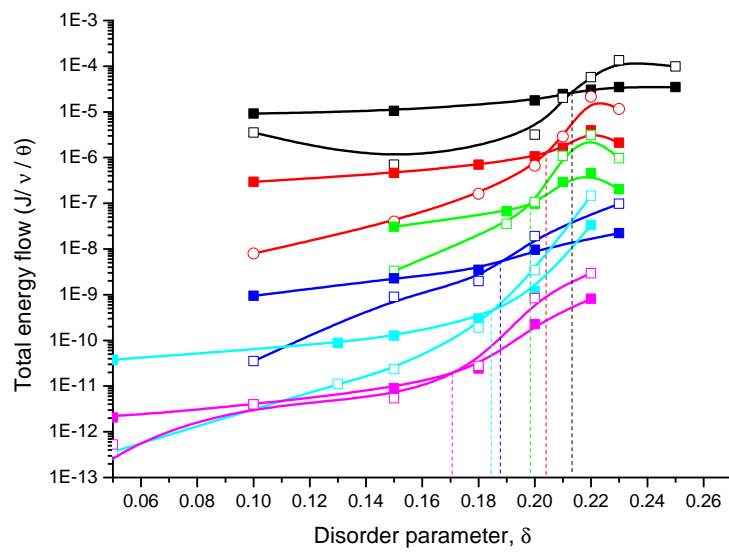


Figure 4.15: Total energy in the ballistic (solid symbols) and scattered (open symbols) light passing through sensor 2 for structures with background refractive index:  $n = 1.8$  (black),  $n = 2.0$  (red),  $n = 2.2$  (green),  $n = 2.43$  (blue),  $n = 2.7$  (cyan) and  $n = 3.0$  (magenta). The vertical dashed lines indicate the disorder parameter at which the energy in the scattered light exceeds that in the ballistic light.

gap means that the energy transmitted through the crystal per unit frequency will be lower. For each value of background refractive index there is a point where the energy flow in the scattered light becomes greater than the energy flow in the ballistic light. This crossover point is defined as the threshold disorder,  $\delta_{\text{th}}^E$ , for this analysis and is indicated in the figure by the vertical dashed lines. As we are interested in the energy in the ballistic light compared to that in the scattered light, the actual energy value is not important. An estimate of the error was calculated in a similar manner to that in Section 4.5.1 by considering the value of the mean plus one standard deviation at the same value of total energy flow for which the crossover occurs (this is not represented in the figure). It should be noted that Figure 4.15 displays a logarithmic scale indicating a vast change in behaviour of the system with the increase in disorder.

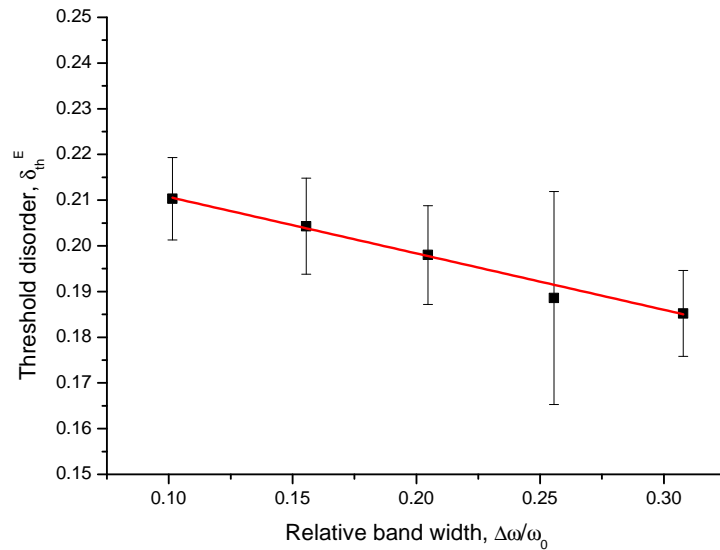


Figure 4.16: Threshold disorder,  $\delta_{\text{th}}^E$  defined as the point at which the energy in the scattered light becomes greater than the energy in the ballistic light, as a function of relative band width with a trend line fit.

Figure 4.16 shows the threshold disorder, as described by the energy flow in the scattered light becoming greater than the energy in the ballistic light, as a function of relative band width. Threshold disorder decreases with increasing relative band

width and the trendline fit (red) is given by

$$\delta_{\text{th}}^E = (0.223 \pm 0.001) - (0.123 \pm 0.005)\Delta\omega/\omega_0 \quad (4.33)$$

with an  $R^2$  value of 0.9941. This shows a very weak dependence of the threshold disorder on relative band width.

### 4.5.3 Mean refractive index

Instead of the relative band width, the mean refractive index may also be used as a parameter to describe variation in the threshold disorder parameter. The mean refractive index of the photonic crystal may be calculated by weighting the substrate and the air holes refractive index by area. The total area of one unit cell is given by

$$A_{\text{total}} = \frac{\sqrt{3}}{2}a^2 \quad (4.34)$$

where  $a$  is the lattice parameter. The area covered by air holes in one unit cell is equal to the area of one circle with radius  $r=0.4a$ :

$$A_{\text{circle}} = \pi(0.4)^2. \quad (4.35)$$

The remaining area has the refractive index of the substrate and is given by

$$A_{\text{bg}} = a^2 \left( \frac{\sqrt{3}}{2} - 0.16\pi \right). \quad (4.36)$$

The weighted mean gives the mean refractive index:

$$n_0 = \frac{(A_{\text{circle}}n_{\text{air}}) + (A_{\text{bg}}n_{\text{bg}})}{A_{\text{total}}}. \quad (4.37)$$

For the flux analysis, Figure 4.17 shows that changing the dependent variable has no effect on the constant trendline:  $\delta_{\text{th}}^F = 0.2048 \pm 0.0012$ . The threshold disorder parameter for the directional energy analysis,  $\delta_{\text{th}}^E$  may be fitted to the mean refractive index as:

$$\delta_{\text{th}}^E = (0.294 \pm 0.005) - (0.0670 \pm 0.003)n_0 \quad (4.38)$$

with an  $R^2$  value of 0.9894. Figure 4.18 shows the threshold disorder parameter as a function of mean refractive index as calculated by the directional analysis (black

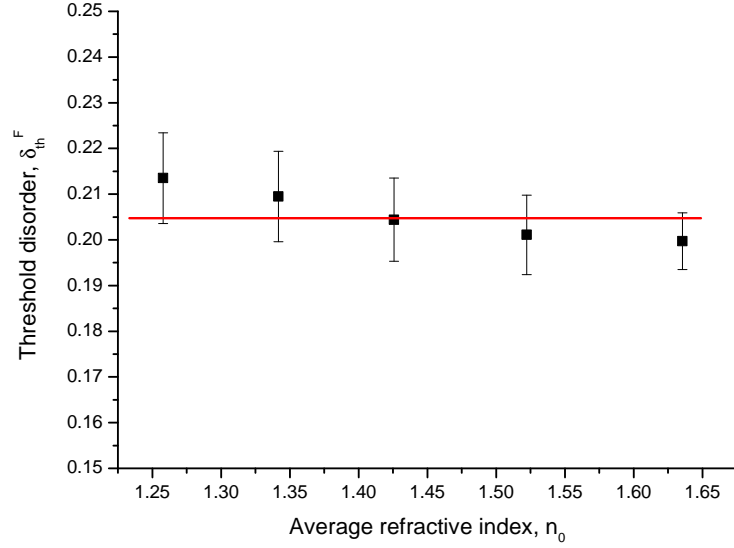


Figure 4.17: Threshold disorder,  $\delta_{th}^F$  as a function of mean refractive index with a trend line fit.

points). The red trendline shows the fit given by Equation 4.38 and the green line shows a numerical fit given by the equation

$$\delta_{th}^E = 0.12 + \frac{(\omega_0 - \Delta\omega)n_0}{6}. \quad (4.39)$$

Equation 4.39 fits the data within the given error bars, however this is not a physically meaningful interpretation and so it would not be applied to other systems without great caution.

#### 4.5.4 Frequency limits

Figure 4.19 shows how the band edges of the photonic band gap of an ideal crystal vary as the radius  $r$  of the air holes is altered for different background refractive indices  $n$ . The dashed lines indicate the centre of band gap frequency for the case  $r = 0.4 \mu\text{m}$ . The range of values of  $r$  for which the centre of band gap for  $r = 0.4 \mu\text{m}$  remains in the new band gap is very similar for all three background refractive indices considered, roughly  $0.33 \mu\text{m} - 0.45 \mu\text{m}$ . This suggests that if the radii of the cylindrical air holes in the photonic crystal were uniformly increased or decreased

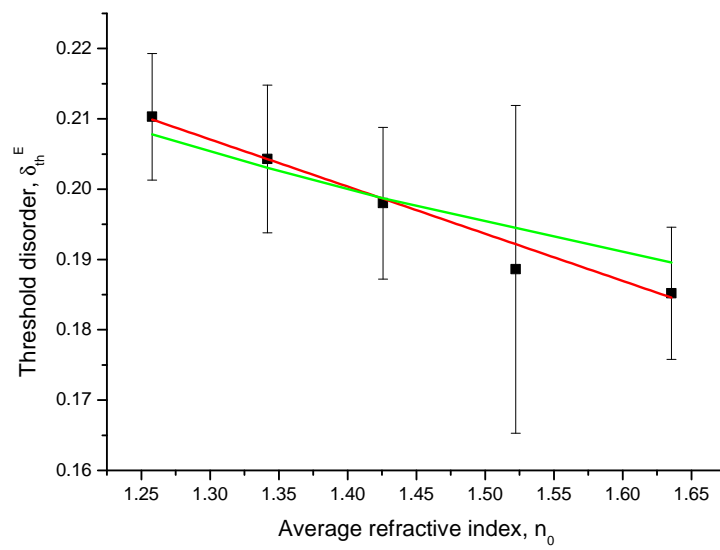


Figure 4.18: Threshold disorder parameter, defined as the point at which the energy in the scattered light becomes greater than the energy in the ballistic light, as a function of mean refractive index. The red trendline shows the fit given by Equation 4.38 and the green line shows the fit given by Equation 4.39.

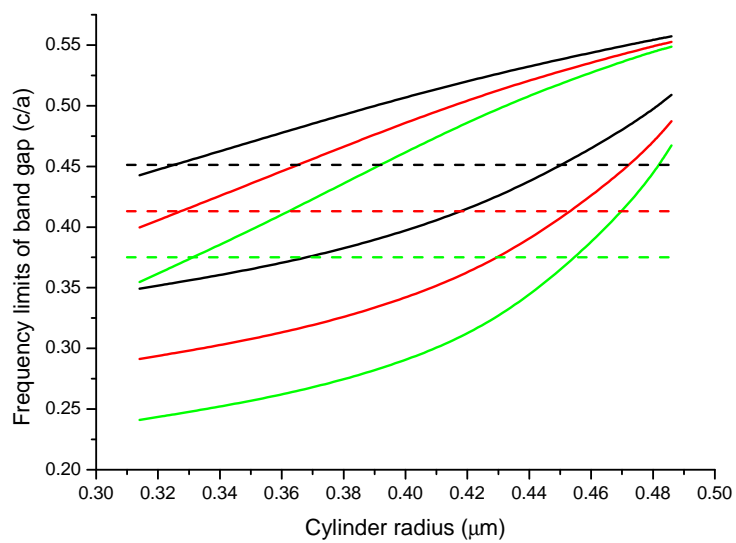


Figure 4.19: Upper and lower band edges for the complete band gap of an ideal photonic crystal structure with all the air holes having radius  $r$ . Black represents a structure with background refractive index  $n = 1.8$ , red represents  $n = 2.2$  and green represents  $n = 2.7$ . The horizontal dashed lines indicate the frequency at the centre of the band gap for the case of air holes with radius  $r = 0.4 \mu\text{m}$ .

by 7% or more the band gap of the new structure would not contain the frequency corresponding to the centre of the photonic band gap for a structure with air holes of radius  $r = 0.4 \mu\text{m}$ . Although this analysis of the frequency limits of the photonic band gap corresponds to ideal photonic crystals with the radii of all the cylinders being the same, we may still gain some insight into the behaviour of disordered photonic crystals using the same ideas. When disorder is imposed on the radii of the air cylinders it is reasonable to assume that the band gap of the disordered photonic crystal varies locally in a manner similar to that for an ideal structure with the same cylinder radius. For example, a randomly disordered configuration may have a small area in which the cylinder radii are consistently smaller than the ideal  $r = 0.4 \mu\text{m}$  and in this locality the band gap will be shifted to a slightly lower frequency range. Similarly, for a small area in which the cylinder radii were all greater than the ideal  $r = 0.4 \mu\text{m}$  the local band gap would be shifted to a higher frequency range. It should be noted that a photonic band gap is not a local phenomena and occurs due to periodicity in a photonic crystal structure and so this brief look at the frequency limits of the band gap of structures with consistently lower or higher background refractive index can not be used as a reliable model for a disordered system. However, it does provide a physical picture of the effects of disorder on the band gap.

## 4.6 Discussion

The effect of disorder, in a two-dimensional photonic crystal, on the transmission of light through the structure, including the transmission of ballistic and scattered light separately, has been studied. The photonic crystal under consideration was a dielectric slab with a hexagonal array of cylindrical air holes. Disorder was imposed on the radii of the air holes using random configurations of a uniform distribution over a range  $r_0(1 - \delta)$  to  $r_0(1 + \delta)$  where the ideal hole radius,  $r_0$  was  $0.4 \mu\text{m}$  and  $\delta$  was the disorder parameter. Dielectric substrates with refractive indices in the range 1.8 to 2.7 were considered. The investigation was carried out with TM-polarised light in order that the ideal photonic crystal structure should have a complete band

gap. For substrates with refractive indices below  $n = 1.8$  the photonic band gap was considered too small due to the low contrast in refractive index between the substrate and the holes. For substrates with refractive index above  $n = 2.7$  the contrast was too great for the simulation, leading to instabilities in the results.

The effect of disorder on the total transmission of light at frequencies close to that of the centre of the photonic band gap for an ideal crystal was found to have a threshold value close to  $\delta = 0.2$  for all substrates considered. This means that for values of disorder below  $\delta = 0.2$  we expect the standard deviation of the transmitted flux in an ensemble of structures to remain below the mean value. This indicates that, for most configurations of disorder, any peaks in the transmission minimum associated with the band gap do not occur at the centre of the band gap and so do not have a significant effect on the transmission at that frequency. Above  $\delta = 0.2$  the standard deviation becomes greater than the mean, indicating that for a significant number of configurations of disorder there are peaks in the transmission spectrum dip towards the centre of the band gap. We would then expect transmission through the photonic crystal to increase significantly.

The effect of disorder on the energy flow of ballistic and scattered light was found to be characterised by a threshold disorder parameter that decreased linearly with relative band width or with mean refractive index. The threshold disorder in this case marked a change of behaviour in the system such that the energy in the scattered light exceeded that in the ballistic light. Two equations were proposed that provide a fit to the simulated data to describe the relationship. The intent was to numerically match up the coefficients in the trendline using known parameters of the system. However, this has not been wholly successful and the narrow range of available data makes it difficult to draw any substantial conclusions.

Recalling that the definitions of threshold disorder parameter in the two analyses are different it does not make sense to compare the two directly. The two analyses of results from the simulation were undertaken on physical grounds rather than strictly quantitative reasoning. This is because the study of disorder in two-dimensional photonic crystals is more complex than that for their one-dimensional counterparts.

A study by Ryu *et al.* [126] that gave quantitative results of the effect of disorder

in the radii of holes in a photonic crystal structure, suggested that manufacturing techniques in 1999 were capable of producing holes of a given radius with accuracy better than  $0.01a$  where  $a$  is the lattice parameter of the photonic crystal. This corresponds to a disorder parameter of  $\delta = 0.05$  which is well below the empirical threshold disorder parameters that have been calculated here. This suggests that disorder in the radius of holes in photonic crystals due to manufacturing processes (with this accuracy) would, in reality, have very little effect on the transmission of light at the frequency corresponding to the centre of the photonic band gap.

Beggs *et al.* [129] studied the same photonic crystal structure as that considered in this chapter, but with GaAs as the substrate material, with refractive index  $n = 3.7$  (greater than the refractive indices considered here). The transmission of ballistic and scattered light through the structure were modelled separately. As the disorder parameter increased from  $\delta = 0.1$  to  $\delta = 0.2$  they found there was a significant increase in the amount of light transmitted through the structure. The same trend was found in the photonic crystal structures with lower substrate refractive indices considered in the work carried out for this thesis.

A study carried out by Zhu *et al.* [133] considered the effect of radius and positional disorder on the properties of a photonic crystal microcavity formed by a missing dielectric rod in a square array of rods in air. They found that disorder in the radius of the rods had little effect on either the Q-factor or the resonant frequency of the microcavity, whereas the positional disorder had a significant effect on the latter. They suggested that altering the position of the centre of the rods has greater disruptive effect on the periodicity of the lattice than altering the radii. This implies that positional disorder has a greater effect on the properties of photonic crystals and it would be interesting to extend this study to include positional disorder.

In conclusion, insufficient data has been obtained in this study to provide a convincing, quantitative relationship between the threshold disorder parameter and the relative band width of photonic crystals formed from a hexagonal array of holes in a substrate material with disorder imposed on the radius of the holes. However, as far as the author is aware, this is a unique attempt to analyse the effect of disorder on materials with different relative band widths and the method used could be extended

to consider other forms of disorder or other geometries of photonic crystal. In accordance with other published results, we have demonstrated qualitatively that low levels of disorder in the radius of the air holes have little effect on the transmission of light with frequency close to the centre of the photonic band gap.

# Chapter 5

## Summary and future work

Techniques for controlling light and its interactions with matter are currently of great interest to research communities worldwide. Light-matter interactions exhibit many interesting fundamental effects as well as the promise of new technology. This thesis has presented work on different light-matter interactions. Firstly, two types of polariton have been considered. We have also considered the affect of disorder on the band gap of photonic crystals.

Exciton-polaritons have a wealth of fundamental physics associated with them and are promising candidates for many varied applications. The formation of exciton-polaritons from optical whispering-gallery modes in submicron spheres, also containing an exciton, have been studied in the materials GaAs, GaN and ZnO. It has been found that optical modes with a decay constant greater than the polariton splitting form weakly coupled exciton-polaritons and those with decay constant less than the polariton splitting form exciton-polaritons in the strong coupling regime. The minimum radii of spheres required to support optical modes with various  $l$  values have also been found.

There is currently much interest in exciton-polaritons in ZnO due to their high binding energy, making possible stable strong coupling at room temperature. We have shown that, in submicron spheres, the requirement for strong coupling and a high binding energy must be balanced against the need for strong confinement and long lifetime of the optical mode. Previous studies of exciton-polaritons in spherical cavities focused on spheres with larger radius than those with the submicron di-

mensions considered here, or have been restricted to the case with quantum number  $l$  equal to unity. The studies of exciton-polaritons in spherical cavities have hitherto been theoretical while experimental work has focused on planar and cylindrical microcavities. This is possibly due to the difficulties involved in fabricating suitable spherical microcavities. A discussion has been given in Chapter 2 as to how spherical microcavities have been fabricated for other applications. Further work on exciton-polaritons in submicron spheres might consider the specific conditions required for Bose-Einstein condensation.

Tamm plasmon-polaritons have been shown to be supported by cylindrical Bragg reflector structures containing a metal core, metal cladding around the outside of the structure or metal in both of these locations. Cylindrical TPPs can exist in both the TE and TM polarisations and can also be formed from hybrid cylindrical modes which do not occur in the planar case. In the case of metal both in the core and around the outside of the fibre it has been shown that two split modes can be supported with a frequency difference in the terahertz regime. Cylindrical TPPs have been shown to have low effective masses and those with values of  $\beta$  close to zero have been shown to have low group velocities. The calculations presented in this thesis are for a lossless metal. Also, for the cases with metal on the outside of the structure, the metal was ‘infinite’ so there was no transmission loss. While these simplifications are not expected to have significant implications for the prediction of the modes of the system, further work to include loss in the model will be important for predicting the detailed results of spectroscopy experiments. It would be interesting to extend the analysis of Tamm plasmon-polaritons to the spherical geometry. However, it is likely to be even more difficult to fabricate a spherical Bragg reflector than a cylindrical one. Further work on Tamm plasmon-polaritons in cylindrical structures might also include changing the distribution of metal, for example, it may be possible to generate light with high orbital angular momentum by including metal in stripes on the outside of the structure parallel to the fibre axis. In the planar case, it has been shown that Tamm plasmon-polaritons may be coupled to exciton-polaritons - this could also be investigated in the cylindrical case.

Both aspects of the work on polaritons presented here would now benefit from

experimental work being carried out to verify the theoretical calculations presented and to explore related physical effects.

Finally in this thesis another type of light-matter interaction has been considered. The effect of disorder in a two-dimensional photonic crystal on the total transmission of light and on the energy flow in ballistic and scattered light has been studied. The photonic crystal under consideration was a dielectric slab with a hexagonal array of cylindrical air holes, with disorder taking the form of a random distribution of hole radii over a range defined by a disorder parameter. Dielectric substrates with refractive indices in the range 1.8 to 2.7 were considered. Empirical, numerical relationships between relative band width, the ratio of the width of the photonic band gap to the frequency at the centre of the band gap for the ideal photonic crystal, and the threshold disorder, defined in two different ways, have been proposed. These show that there is little dependence of the threshold disorder parameter on relative band width. Further study may allow this to be presented more analytically. As it seems that disorder in the hole radii does not have a great effect on the photonic crystal properties it would be interesting to run a similar investigation for another type of disorder, for example disorder in the position of each cylinder axis. Other groups have already studied the effects of positional disorder on the photonic band gap but these investigations have been restricted to one type of substrate and do not attempt to provide a general relationship between relative band width and threshold disorder.

# Bibliography

- [1] M. S. Skolnick, T. A. Fisher, and D. M. Whittaker. Strong coupling phenomena in quantum microcavity structures. *Semiconductor Science and Technology*, 13:645, 1998.
- [2] P. N. Prasad. *Nanophotonics*. Wiley, 2004.
- [3] M. A. Kaliteevski and R. A. Abram. Bragg reflectors for cylindrical waves. *Journal of Modern Optics*, 46:875, 1999.
- [4] M. A. Kaliteevski, S. Brand, and R. A. Abram. Optical eigenmodes of a multilayered spherical microcavity. *Journal of Modern Optics*, 48:1503, 2001.
- [5] E. Yablonovitch. Inhibited spontaneous emission in solid-state physics and electronics. *Physical Review Letters*, 58:2059, 1987.
- [6] S. John. Strong localization of photons in certain disordered dielectric superlattices. *Physical Review Letters*, 58:2486, 1987.
- [7] J. D. Joannopoulos, S. G. Johnson, J. N. Winn, and R. D. Meade. *Photonic Crystals: Moulding the flow of light*. Princeton University Press, 2nd edition, 2008.
- [8] J. M. Lourtioz, H. Benisty, A. Tchelnokov, V. Berger, J. M. Gerard, D. Maystre, and D. Pagnoux. *Photonic Crystals: towards nanoscale photonic devices*. Springer, 2nd edition, 2008.
- [9] J. D. Joannopoulos, P. R. Villeneuve, and S. Fan. Photonic crystals: putting a new twist on light. *Nature*, 386:143, 1997.

- [10] O. Painter, R. K. Lee, A. Scherer, A. Yariv, J. D. O'Brien, P. D. Dapkus, and I. Kim. Two-dimensional photonic band-gap defect mode laser. *Science*, 284:1819, 1999.
- [11] S. Noda, M. Yokoyama, M. Imada, A. Chutinan, and M. Mochizuki. Polarization mode control of two-dimensional photonic crystal laser by unit cell structure design. *Science*, 293:1123, 2001.
- [12] P. Russell. Photonic crystal fibres. *Science*, 299:358, 2003.
- [13] J. C. Knight. Photonic crystal fibres. *Nature*, 424:847, 2003.
- [14] M. Notomi. Manipulating light with strongly modulated photonic crystals. *Reports on Progress in Physics*, 73:096501, 2010.
- [15] M. Notomi. Theory of light propagation in strongly modulated photonic crystals: Refractionlike behavior in the vicinity of the photonic band gap. *Physical Review B*, 62:10696, 2000.
- [16] M. M. Sigalas, C. T. Chan, K. M. Ho, and C. M. Soukoulis. Metallic photonic band-gap materials. *Physical Review B*, 52:11744, 1995.
- [17] M. Kaliteevski, D. Beggs, S. Brand, and R. Abram. Statistics of the eigenmodes and optical properties of one-dimensional disordered photonic crystals. *Physical Review E*, 73:056616, 2006.
- [18] C. Weisbuch, M. Nishioka, A. Ishikawa, and Y. Arakawa. Observation of the coupled exciton-photon mode splitting in a semiconductor microcavity. *Physical Review Letters*, 69:3314, 1992.
- [19] J. Kasprzak *et al.* Bose-Einstein condensation of exciton polaritons. *Nature*, 443:409, 2006.
- [20] J. Keeling and N. G. Berloff. Exciton-polariton condensation. *Contemporary Physics*, 52:131, 2011.

- [21] Le Si Dang, D. Heger, R. André, F. Boeuf, , and R. Romestain. Stimulation of polariton photoluminescence in semiconductor microcavity. *Physical Review Letters*, 81:3920, 1998.
- [22] S. Christopoulos *etal.* Room-temperature polariton lasing in semiconductor microcavities. *Physical Review Letters*, 98:126405, 2007.
- [23] A. Baas, J.-Ph. Karr, M. Romanelli, A. Bramati, and E. Giacobino. Optical bistability in semiconductor microcavities in the nondegenerate parametric oscillation regime: Analogy with the optical parametric oscillator. *Physical Review B*, 70:161307, 2004.
- [24] A. Amo, T. C. H. Liew, C. Adrados, R. Houdré, E. Giacobino, A. V. Kavokin, and A. Bramati. Exciton polariton spin switches. *Nature Photonics*, 4:361, 2010.
- [25] C. Leyder, T. C. H. Liew, A. V. Kavokin, I. A. Shelykh, M. Romanelli nad J.-Ph. Karr, E. Giacobino, and A. Bramati. Interference of coherent polariton beams in microcavities: Polarization-controlled optical gates. *Physical Review Letters*, 99:196402, 2007.
- [26] T. Ostatnický, I. A. Shelykh, and A. V. Kavokin. Theory of polarization controlled polariton logic gates. *Physical Review B*, 81:125319, 2010.
- [27] T. C. H. Liew, A. V. Kavokin, and I. A. Shelykh. Optical circuits based on polariton neurons in semiconductor microcavities. *Physical Review Letters*, 101:016402, 2008.
- [28] D. Bajoni, P. Senellart, E. Wertz, I. Sagnes, A. Miard, A. Lemaître, and J. Bloch. Polariton laser using single micropillar GaAs-GaAlAs semiconductor cavities. *Physical Review Letters*, 100:47401, 2008.
- [29] G. Panzarini and L. Andreani. Quantum theory of exciton polaritons in cylindrical semiconductor microcavities. *Physical Review B*, 60:16799, 1999.
- [30] R. H. Ritchie. Plasma losses by fast electrons in thin films. *Physical Review*, 106:874, 1957.

- [31] K. Kneipp, Y. Wang, H. Kneipp, L. T. Perelman, I. Itzkan, R. R. Dasari, and M. S. Feld. Single molecule detection using surface-enhanced Raman scattering (SERS). *Physical Review Letters*, 78:1667, 1997.
- [32] J. M. Pitarke, V. M. Silkin, E. V. Chulkov, and P. M. Echenique. Theory of surface plasmons and surface-plasmon polaritons. *Reports on Progress in Physics*, 70:1, 2007.
- [33] W. L. Barnes, A. Dereux, and T. W. Ebbesen. Surface plasmon subwavelength optics. *Nature*, 424:824, 2003.
- [34] T. W. Ebbesen, H. J. Lezec, H. F. Ghaemi, T. Thio, and P. A. Wolff. Extraordinary optical transmission through sub-wavelength hole arrays. *Nature*, 391:667, 1998.
- [35] F. J. Garcia-Vidal, L. Martin-Moreno, T. W. Ebbesen, and L. Kuipers. Light passing through subwavelength apertures. *Reviews of Modern Physics*, 82:729, 2010.
- [36] D. A. Schultz. Plasmon resonant particles for biological detection. *Current Opinion in Biotechnology*, 14:13, 2003.
- [37] N. Fang, H. Lee, C. Sun, and X. Zhang. Subdiffraction-limited optical imaging with a silver superlens. *Science*, 308:534, 2005.
- [38] A. V. Krasavin, A. V. Zayats, and N. I. Zheludev. Active control of surface plasmonpolariton waves. *Journal of Optics A*, 7:85, 2005.
- [39] R. Charbonneau, N. Lahoud, G. Mattiussi, and P. Berini. Demonstration of integrated optics elements based on long ranging surface plasmon polaritons. *Optics Express*, 13:977, 2005.
- [40] Y. Bian, Z. Zheng, X. Zhao, J. Zhu, and T. Zhou. Symmetric hybrid surface plasmon polariton waveguides for 3d photonic integration. *Optics Express*, 17:21320, 2009.

- [41] M. Kaliteevski, I. Iorsh, S. Brand, R. A. Abram, J. M. Chamberlin, A. V. Kavokin, and I. A. Shelykh. Tamm plasmon-polaritons: possible electromagnetic states at the interface of a metal and a dielectric Bragg mirror. *Physical Review B*, 76:165415, 2007.
- [42] M. E. Sasin, R. P. Seisyan, M. A. Kaliteevski, S. Brand, R. A. Abram, J. M. Chamberlin, A. Yu. Egorov, A. P. Vasil'ev, V. S. Mikhlin, and A. V. Kavokin. Tamm plasmon polaritons: Slow and spatially compact light. *Applied Physics Letters*, 92:251112, 2008.
- [43] C. Symonds, A. Lemaître, E. Homeyer, J. C. Plenet, and J. Bellessa. Emission of Tamm plasmon/exciton polaritons. *Applied Physics Letters*, 95:151114, 2009.
- [44] T. C. H. Liew, A. V. Kavokin, T. Ostatnický, M. Kaliteevski, I. A. Shelykh, and R. A. Abram. Exciton-polariton integrated circuits. *Physical Review B*, 82:033302, 2010.
- [45] C. Xue, H. Jiang, and H. Chen. Highly efficient all-optical diode action based on light-tunneling heterostructures. *Optics Express*, 18:7479, 2010.
- [46] G. Du, H. Jiang, Z. Wang, Y. Yang, Z. Wang, H. Lin, and H. Chen. Heterostructure-based optical absorbers. *Journal of the Optical Society of America B*, 27:1757, 2010.
- [47] W. L. Zhang and S. F. Yu. Bistable switching using an optical Tamm cavity with a Kerr medium. *Optics Communications*, 283:2622, 2010.
- [48] C. Grossmann, C. Coulson, G. Christmann, I. Farrer, H. Beere, D. Ritchie, and J. Baumberg. Tuneable polaritonics at room temperature with strongly coupled Tamm plasmon polaritons in metal/air-gap microcavities. *Applied Physics Letters*, 98:231105, 2011.
- [49] M. Kaliteevski, S. Brand, R. A. Abram, I. Iorsh, A. V. Kavokin, and I. A. Shelykh. Hybrid states of Tamm plasmons and exciton polaritons. *Applied Physics Letters*, 95:251108, 2009.

- [50] S. Al-Bader and M. Imtaar. Optical fibre hybrid-surface plasmon polaritons. *Journal of the optical society of America B*, 10:83, 1993.
- [51] B. Prade and J. Vinet. Guided optical waves in fibres with negative dielectric constant. *Journal of lightwave technology*, 12:6, 1994.
- [52] C. E. Platts, M. A. Kaliteevski, S. Brand, R. A. Abram, I. V. Iorsh, and A. V. Kavokin. Whispering-gallery exciton polaritons in submicron spheres. *Physical Review B*, 79:245322, 2009.
- [53] C. Kittel. *Introduction to Solid State Physics*. Wiley, 6th edition, 1986.
- [54] A. Kavokin, J. Baumberg, G. Malpuech, and F. Laussy. *Microcavities*. Oxford Science Publications, 2007.
- [55] S. I. Pekar. Theory of electromagnetic waves in a crystal in which excitons arise. *Journal of Experimental and Theoretical Physics, USSR*, 33:1022, 1957.
- [56] V. M. Agranovich. On the influence of reabsorption on the decay of fluorescence in molecular crystals. *Optika i Spektroskopiya*, 3:84, 1957.
- [57] J. J. Hopfield. Theory of the contribution of excitons to the complex dielectric constant of crystals. *Physical Review*, 112:1555, 1958.
- [58] H. Haug and S. W. Koch. *Quantum Theory of the Optical and Electronic Properties of Semiconductors*. World Scientific, 3rd edition, 2001.
- [59] D. I. Babic and S. W. Corzine. Analytic expressions for the reflection delay, penetration depth and absorptance of quarter-wave dielectric mirrors. *IEEE Journal of Quantum Optics*, 28:514, 1992.
- [60] A. Kavokin and G. Malpuech. *Cavity Polaritons*. Elsevier, 1st edition, 2003.
- [61] T. A. Fisher, A. M. Afshar, D. M. Whittaker, J. S. Roberts, G. Hill, and M. A. Pate. Electric-field and temperature tuning of exciton-photon coupling in quantum microcavity structures. *Physical Review B*, 51:2600, 1995.

- [62] J. Tignon, P. Voisin, C. Delalande, M. Voos, R. Houdré, U. Oesterle, and R. P. Stanley. From Fermi's golden rule to the vacuum Rabi splitting: Magneto-polaritons in a semiconductor optical microcavity. *Physical Review Letters*, 74:3967, 1995.
- [63] A. Kavokin. Exciton-polaritons in microcavities: Recent discoveries and perspectives. *Physica Status Solidi B*, 247:1898, 2010.
- [64] A. Imamoglu and R. Ram. Quantum dynamics of exciton lasers. *Physics Letters A*, 214:193, 1996.
- [65] S. Tsintzos, N. Pelekanos, G. Konstantinidis, Z. Hatzopoulos, and P. Savvidis. A GaAs polariton light-emitting diode operating near room temperature. *Nature*, 453:372, 2008.
- [66] A. Khalifa, A. Love, D. Krizhanovskii, M. Skolnick, and J. Roberts. Electroluminescence emission from polariton states in GaAs-based semiconductor microcavities. *Applied Physics Letters*, 92:061107, 2008.
- [67] R. Balili, V. Hartwell, D. Snoke, L. Pfeiffer, and K. West. Bose-Einstein condensation of microcavity polaritons in a trap. *Nature*, 443:409, 2006.
- [68] F. Tassone, C. Piermarocchi, V. Savona, A. Quattropani, and P. Schwendimann. Bottleneck effects in the relaxation and photoluminescence of microcavity polaritons. *Physical Review B*, 56:7554, 1997.
- [69] I. Shelykh, K. V. Kavokin, A. V. Kavokin, G. Malpuech, P. Bigenwald, H. Deng, G. Weihs, and Y. Yamamoto. Semiconductor microcavity as a spin-dependent optoelectronic device. *Physical Review B*, 70:035320, 2004.
- [70] M. A. Kaliteevski, S. Brand, R. A. Abram, A. Kavokin, and Le Si Dang. Whispering gallery polaritons in cylindrical cavities. *Physical Review B*, 75:233309, 2007.
- [71] M. Kaliteevski, S. Brand, R. Abram, V. Nikolaev, M. Maximov, C. Sotomayor Torres, and A. Kavokin. Electromagnetic theory of the coupling of zero-

- dimensional exciton and photon states: A quantum dot in a spherical microcavity. *Physical Review B*, 64:115305, 2001.
- [72] P. Bigenwald, V. Nikolaev, D. Solnyshkov, A. Kavokin, G. Malpuech, and B. Gil. Polariton lasers based on semiconductor quantum microspheres. *Physical Review B*, 70:205343, 2004.
- [73] H. Ajiki and K. Cho. Longitudinal and transverse components of excitons in a spherical quantum dot. *Physical Review B*, 62:7402, 2000.
- [74] H. Ajiki, T. Tsuji, K. Kawano, and K. Cho. Optical spectra and exciton-light coupled modes of a spherical semiconductor nanocrystal. *Physical Review B*, 66:245322, 2002.
- [75] N. I. Nikolaev, A. Smith, and A. L. Ivanov. Polariton optics of semiconductor photonic dots: weak and strong coupling limit. *Journal of Physics: Condensed Matter*, 16:3703, 2004.
- [76] I. Iorsh. Private Communication, 2009.
- [77] B. G. Kornev. *Introduction to Bessel Function Theory*. Moscow, 1971.
- [78] M. Julier, J. Campo, B. Gil, J. Lascaray, and S. Nakamura. Determination of the spin-exchange interaction constant in wurtzite GaN. *Physical Review B*, 57:6791, 1998.
- [79] T. Makino, C. Chia, N. Tuan, Y. Segawa, M. Kawasaki, A. Ohtomo, K. Tamura, and H. Koinuma. Exciton spectra of ZnO epitaxial layers on lattice-matched substrates grown with laser-molecular-beam epitaxy. *Applied Physics Letters*, 76:3549, 2000.
- [80] M. Zamfirescu, A. Kavokin, B. Gill, G. Malpuech, and M. Kaliteevski. ZnO as a material mostly adapted for the realization of room-temperature polariton lasers. *Physical Review B*, 65:161205, 2002.
- [81] Y. Xia, Y. Yin B. Gates, and Y. Lu. Monodispersed colloidal spheres: Old materials with new applications. *Advanced Materials*, 12:693, 2000.

- [82] K. Vahala. Optical microcavities. *Nature*, 424:839, 2003.
- [83] J. Knight, N. Dubreuil, V. Sandoghdar, J. Hare, V. Lefèvre-Seguin, J. Raimond, and S. Haroche. Mapping whispering-gallery modes in microspheres with a near-field probe. *Optics Letters*, 20:1515, 1995.
- [84] X. W. Wu, C. Zou, J. Cui, Y. Yang, Z. F. Han, and G. C. Gu. Modal coupling strength in a fibre taper coupled silica microsphere. *Journal of Physics B*, 42:085401, 2009.
- [85] V. N. Astratov, S. Yang, S. Lam, B. D. Jones, D. Sanvitto, D. M. Whittaker, A. M. Fox, M. S. Skolnick, A. Tahraoui, P. W. Fry, and M. Hopkinson. Whispering gallery resonances in semiconductor micropillars. *Applied Physics Letters*, 91:071115, 2007.
- [86] Born and Wolf. *Principles of Optics*. Cambridge University Press, 6th edition, 1998.
- [87] R. H. Ritchie, E. T. Arakawa, J. J. Cowan, and R. N. Hamm. Surface-plasmon resonance effect in grating diffraction. *Physical Review Letters*, 21:1530, 1968.
- [88] A. Otto. Excitation of nonradiative surface plasma waves in silver by the method of frustrated total reflection. *Zeitschrift für Physik*, 216:398, 1968.
- [89] D. K. Gramotnev and S. I. Bozhevolnyi. Plasmonics beyond the diffraction limit. *Nature Photonics*, 4:83, 2010.
- [90] A. Kavokin, I. Shelykh, and G. Malpuech. Lossless interface modes at the boundary between two periodic dielectric structures. *Physical Review B*, 72:233102, 2005.
- [91] I. Tamm. Über eine mögliche art der elektronenbindung an kristalloberflächen. *Zeitschrift für Physik A*, 76:849, 1932.
- [92] H. Ohno, E. E. Mendez, J. A. Brum, J. M. Hong, F. Agulló-Rueda, L. L. Chang, and L. Esaki. Observation of Tamm states in superlattices. *Physical Review Letters*, 64:2555, 1990.

- [93] P. Yeh. *Optical Waves in Layered Media*. Wiley, 1988.
- [94] S. Brand, R. A. Abram, and M. A. Kaliteevski. Tailor-made surface plasmon polaritons above the bulk plasma frequency: a design strategy for indium tin oxide. *Journal of Physics D*, 43:145104, 2010.
- [95] M. A. Kaliteevski, V. V. Nikolaev, and R. A. Abram. Calculation of the mode structure of multilayer optical fibres based on transfer matrices for cylindrical waves. *Optics and Spectroscopy*, 88:792, 2000.
- [96] G. B. Arfken and H. J. Weber. *Mathematical Methods for Physicists*. Harcourt Academic Press, 5th edition, 2001.
- [97] C. A. Pfeiffer, E. N. Economou, and K. L. Ngai. Surface polaritons in a circularly cylindrical interface: Surface plasmons. *Physical Review B*, 10:3038, 1974.
- [98] U. Schröter and A. Dereux. Surface plasmon polaritons on metal cylinders with dielectric core. *Physical Review B*, 64:125420, 2001.
- [99] E. Devaux, A. Dereux, E. Bourillot, J.-C. Weeber, Y. Lacroute, Jean-Pierre Goudonnet, and C. Girar. Local detection of the optical magnetic field in the near zone of dielectric samples. *Physical Review B*, 62:10504, 2000.
- [100] J. Hecht. *City of Light*. Oxford University Press, 1999.
- [101] A. W. Snyder and J. D. Love. *Optical Waveguide Theory*. Chapman and Hall, 1983.
- [102] A. Yariv. *Optical Electronics*. CBS college publishing, 3rd edition, 1985.
- [103] J. Buck. *Fundamentals of Optical Fibres*. Wiley, 1st edition, 1995.
- [104] B. Sun, Y. Gu, X. Hu, and Q. Gong. A trade off between propagation length and light confinement in cylindrical metal-dielectric waveguides. *Chinese Physics Letters*, 28:057303, 2011.

- [105] D. Chen. Cylindrical hybrid plasmonic waveguide for subwavelength confinement of light. *Applied Optics*, 49:6868, 2010.
- [106] M. Kaliteevski, R. Abram, V. Nikolaev, and G. Sokolovski. Bragg reflectors for cylindrical waves. *Journal of Modern Optics*, 46:875, 1999.
- [107] M. Kaliteevski, R. Abram, and V. Nikolaev. Optical eigenmodes of a cylindrical microcavity. *Journal of Modern Optics*, 47:677, 2000.
- [108] J. D. Jackson. *Classical Electrodynamics*. Wiley, 3rd edition, 1999.
- [109] H. Y. Lee and T. Yao.  $\text{TiO}_2(\text{ZnS})/\text{SiO}_2$  one-dimensional photonic crystals and a proposal for vertical micro-cavity resonators. *Journal of the Korean Physical Society*, 44:387, 2004.
- [110] N. Daude, C. Gout, and C. Jouanin. Electronic band structure of titanium dioxide. *Physical Review B*, 15:3229, 1977.
- [111] R. B. Laughlin. Optical absorption edge of  $\text{SiO}_2$ . *Physical Review B*, 22:3021, 1980.
- [112] R. L. Nelson and J. W. Haus. One-dimensional photonic crystals in reflection geometry for optical applications. *Applied Physics Letters*, 83:1089, 2003.
- [113] P. W. Milonni. *Fast Light, Slow Light, and Left-Handed Light*. Taylor & Francis Group, 2005.
- [114] S. Brand, R. A. Abram, and M. A. Kaliteevski. Bragg reflector enhanced attenuated total reflectance. *Journal of Applied Physics*, 106:113109, 2009.
- [115] S. Brand, M. A. Kaliteevski, and R. A. Abram. Optical Tamm states above the bulk plasma frequency at a Bragg stack/metal interface. *Physical Review B*, 79:085416, 2009.
- [116] T. Goto, A. V. Baryshev, M. Inoue, A. V. Dorofeenko, A. M. Merzlikin, A. P. Vinogradov, A. A. Lisyansky, and A. B. Granovsky. Tailoring surfaces of one-dimensional magnetophotonic crystals: Optical Tamm state and Faraday rotation. *Physical Review B*, 79:125103, 2009.

- [117] L. J. Dong, H. T. Jiang, H. Chen, and Y. L. Shi. Enhancement of Faraday rotation effect in heterostructures with magneto-optical metals. *Journal of Applied Physics*, 107:093101, 2010.
- [118] J. W. S. Rayleigh. *Philosophical Magazine*, 26:256, 1888.
- [119] D. G. Angelakis, P. L. Knight, and E. Paspalakis. Photonic crystals and inhibition of spontaneous emission: an introduction. *Contemporary Physics*, 45:303, 2004.
- [120] S. Noda, N. Yamamoto, H. Kobayashi, M. Okano, and K. Tomoda. Optical properties of three-dimensional photonic crystals based on III - V semiconductors at infrared to near-infrared wavelengths. *Applied Physics Letters*, 75:905, 1999.
- [121] S. Noda, K. Tomoda, N. Yamamoto, and A. Chutinan. Full three-dimensional photonic bandgap crystals at near-infrared wavelengths. *Science*, 289:604, 2000.
- [122] D. Smith, R. Dalichaouch, N. Kroll, S. Schultz, S. McCall, and P.M. Platzman. Photonic band structure and defects in one and two dimensions. *Journal of the Optical Society of America B*, 10:314, 1993.
- [123] A. McGurn, K. Christensen, F. Mueller, and A. Maradudin. Anderson localization in one-dimensional randomly disordered optical systems that are periodic on average. *Physical Review B*, 47:13120, 1993.
- [124] M. Sigalas, C. Soukoulis, E. Economou, C.-T. Chan, and K. Ho. Photonic band gaps and defects in two dimensions: Studies of the transmission coefficient. *Physical Review B*, 48:14121, 1993.
- [125] M. M. Sigalas, C. M. Soukoulis, C. T. Chan, and D. Turner. Localization of electromagnetic waves in two-dimensional disordered systems. *Physical Review B*, 53:8340, 1996.

- [126] H. Y. Ryu, J. K. Hwang, and Y. H. Lee. Effect of size nonuniformities on the band gap of two-dimensional photonic crystals. *Physical Review B*, 59:5463, 1999.
- [127] M. Kaliteevski, J. Manzanares Martinez, D. Cassagne, and J. Albert. Disorder-induced modification of the transmission of light in a two-dimensional photonic crystal. *Physical Review B*, 66:113101, 2002.
- [128] M. Kaliteevski, J. M. Martinez, D. Cassagne, and J. Albert. Disorder-induced modification of the attenuation of light in a two-dimensional photonic crystal with complete band gap. *Physica Status Solidi (a)*, 195:612, 2003.
- [129] D. M. Beggs, M. A. Kaliteevski, R. A. Abram, D. Cassagne, and J. P. Albert. Disorder-induced modification of the transmission of light through two-dimensional photonic crystals. *Journal of Physics: Condensed Matter*, 17:1781, 2005.
- [130] K. Yee. Numerical solutions of initial boundary value problems involving Maxwell's equations in isotropic media. *IEEE Transaction on Antennas and Propagation*, 14:302, 1966.
- [131] K. S. Kunz and R. J. Luebbers. *The Finite Difference Time Domain Method for Electromagnetics*. CRC Press, 1993.
- [132] Photon Design, 14 Leopold Street, Oxford, OX4 1TW. 2005.
- [133] Z. H. Zhu, W. M. Ye, J. R. Ji, X. D. Yan, and C. Zen. Influence of random errors on the characteristics of typical 2D photonic crystal microcavity. *Applied Physics B*, 88:231, 2007.

# Appendix: Reflection from a Bragg reflector

Consider an  $N$  layer Bragg reflector with alternating layers of refractive index  $n_A$  and  $n_B$  with thicknesses  $a$  and  $b$  respectively such that the optical thickness of each layer is:

$$n_A a = n_B b = \frac{\pi c}{2\omega_0} \quad (1)$$

where  $\omega_0$  is the Bragg frequency. The transfer matrix,  $\hat{T}_N$  relating the fields on either side of the  $N$  layers is given in [93] as

$$\hat{T}_N = \begin{pmatrix} AU_{N-1} - U_{N-2} & BU_{N-1} \\ CU_{N-1} & DU_{N-1} - U_{N-2} \end{pmatrix}^N \quad (2)$$

where  $A$ ,  $B$ ,  $C$  and  $D$  are constants,  $U_N = \sin[(N+1)qd]/\sin[qd]$ ,  $d = a + b$  the thickness of one period and  $q$  is found from the dispersion relation:

$$\cos(qd) = \cos(k_A a) \cos(k_B b) - \frac{1}{2} \left( \frac{k_B}{k_A} + \frac{k_A}{k_B} \right) \sin(k_A a) \sin(k_B b). \quad (3)$$

The reflection coefficient is given by

$$r_{BR} = \frac{CU_{N-1}}{AU_{N-1} - U_{N-2}} = \frac{C}{A - \sin[(N-1)qd]/\sin[Nqd]}. \quad (4)$$

Considering a frequency close to the Bragg frequency,  $\omega = \omega_0 + \delta\omega$  and using Equation 1 we have

$$\begin{aligned} k_A a &= \frac{n_1 a}{c} (\omega_0 + \delta\omega) = \frac{\pi}{2} + n_A a \kappa \\ k_B b &= \frac{n_2 b}{c} (\omega_0 + \delta\omega) = \frac{\pi}{2} + n_B b \kappa \end{aligned} \quad (5)$$

where  $\kappa = \delta\omega/c$ . For the case  $\delta\omega$  is small such that we can use the small angle approximations for sin and cos and neglect second order and higher terms in  $\kappa$ , the dispersion relation in Equation 3 simplifies to

$$\cos(qd) = -\frac{1}{2} \left( \frac{n_B}{n_A} + \frac{n_A}{n_B} \right). \quad (6)$$

Looking for solutions of the form  $qd = \pi + ix$  and using the relation  $\cos(ix) = \cosh(x) = (e^x + e^{-x})/2$  we have

$$e^x + e^{-x} = \frac{n_B}{n_A} + \frac{n_A}{n_B} \quad (7)$$

and  $e^x$  may be given by either  $n_A/n_B$  or  $n_B/n_A$ . Substituting  $qd = \pi + ix$  into the sin term in the denominator of Equation 4 we have

$$\begin{aligned} \frac{\sin[(N-1)qd]}{\sin[Nqd]} &= -\frac{\sinh[(N-1)x]}{\sinh[Nx]} \\ &= -\frac{e^{Nx}e^{-x} - e^{-Nx}e^x}{e^{Nx} - e^{-Nx}} \\ &\approx -e^{-x} \end{aligned} \quad (8)$$

for a large number of layers,  $N$  in the Bragg reflector. For a wave that decays into the Bragg reflector we require that

$$e^{iqd} = e^{i\pi}e^{-x} = -e^{-x} \quad (9)$$

and we should choose  $e^{-x} = n_B/n_A$ .

Using values for the constants  $A$  and  $C$  as given in [93] in Equation 4 we obtain for the TE polarisation:

$$r_{BR} = \frac{e^{-ik_Aa} \left[ \frac{i}{2} \left( \frac{k_B}{k_A} - \frac{k_A}{k_B} \right) \sin(k_Bb) \right]}{e^{-ik_Aa} \left[ \cos(k_Bb) - \frac{i}{2} \left( \frac{k_B}{k_A} + \frac{k_A}{k_B} \right) \sin(k_Bb) \right] + \frac{n_B}{n_A}}. \quad (10)$$

Using equation set 5 and the small angle approximations, neglecting second order or higher terms in  $\kappa$ :

$$\begin{aligned} \sin\left(\frac{\pi}{2} + n_Bb\kappa\right) &= \cos(n_Bb\kappa) \approx 1 \\ \cos\left(\frac{\pi}{2} + n_Bb\kappa\right) &= -\sin(n_Bb\kappa) \approx -n_Bb\kappa. \end{aligned} \quad (11)$$

Hence we have

$$r_{BR} = \frac{\left(\frac{n_B}{n_A} - \frac{n_A}{n_B}\right)}{2in_B b \kappa - \left(\frac{n_B}{n_A} + \frac{n_A}{n_B}\right) - 2i\frac{n_B}{n_A} e^{ik_A a}}. \quad (12)$$

After some rearranging and writing Equation 12 as a Taylor series we can write

$$r_{BR} = \exp\left[i\pi \frac{n_B}{n_A - n_B} \frac{\delta\omega}{\omega_0}\right] \quad (13)$$

for the case  $n_A > n_B$ . It should be noted that this expression was derived using the constants  $A$  and  $C$  in Equation 4 for the TE-polarisation however using the analogous TM-polarisation constants eventually gives the same solution. Similarly for the case  $n_B > n_A$  the reflection coefficient is found to be:

$$r_{BR} = -\exp\left[i\pi \frac{n_A}{n_B - n_A} \frac{\delta\omega}{\omega_0}\right]. \quad (14)$$

The expressions for the reflection coefficient given in Kaliteevski *et al.*'s paper [41] are different as they are measured a distance  $a$  from the first interface which results in an additional phase difference:

$$\begin{aligned} 2ak_A &= 2\left(\frac{\pi}{2} + n_A a \kappa\right) \\ &= \pi\left(1 + \frac{\delta\omega}{\omega_0}\right) \end{aligned} \quad (15)$$

and then we have

$$\begin{aligned} \tilde{r}_{BR}|_{n_A > n_B} &= -\exp\left[i\pi \frac{n_A}{n_A - n_B} \frac{\delta\omega}{\omega_0}\right] \\ \tilde{r}_{BR}|_{n_B > n_A} &= \exp\left[i\pi \frac{n_B}{n_B - n_A} \frac{\delta\omega}{\omega_0}\right] \end{aligned} \quad (16)$$

where the tilde denotes the reflection coefficients as they appear in [41].